Measurement of the Cross Section for Diphoton Production in 1.8 TeV Proton-Antiproton Collisions

Draft Version 2.5

Takeshi TAKANO

A dissertation submitted to the Doctoral Program
in Physics, the University of Tsukuba,
in partial fulfillment of the requirements
for the degree of Doctor of Philosophy (Science)
September 1997

Abstract

We have studied the prompt diphoton production in proton-antiproton collisions at a center-of-mass energy of 1.8 TeV by the Collider Detector at Fermilab (CDF) .

The diphoton production in hadron-hadron collisions is one of the clear probe for the test of the Next-to-Leading Order (NLO) calculation of the Quantum Chromodynamics (QCD) because of the advantage of the detection of the photons with good energy resolution. The measurement of the diphoton production cross section can be used to check the QCD theory, as well as the background study for Higgs bosons decaying to diphotons with large transverse energy which will be produced in future hadron collider (LHC) . The diphoton production is also a good probe for measuring the effects of the multiple initial soft gluon radiations and the intrinsic transverse momentum of the initial state partons, which are beyond the QCD theory, by looking at the transverse momentum of the diphoton system .

The data were stored by the CDF detector placed at BØ area of the Fermilab Tevatron collider during 1992 - 1995 collider run. The total integrated luminosity was 110 pb^{-1}. The trigger system, including both the hardware and the software modules, required the collision events to have two large and isolated electromagnetic energy depositions in the Central Electromagnetic Calorimeter (CEM) . The clusters were also required to have EM-dominant energy depositions; the hadronic energy deposition to be small.

At offline level, we selected events which had no tracks associated with them. The EM shower profile should be close to that from testbeam electrons and no large second clusters at the shower maximum region. Geometrical cuts were also applied to the data. The efficiencies of the photons for each selection criterion were calculated with various CDF physics datasets.

The backgrounds against prompt photons come from neutral mesons (π^0s, ηs, and

K_s^0s) decaying into multi-photons. We cannot separate them event-by-event at their transverse momentum larger than 10 GeV/c. The backgrounds were subtracted statistically by using the information such as the shower profile at the shower maximum position in the CEM and the conversion rate in front of the CEM. The background subtraction method was presented with its systematic uncertainties.

A photon fraction in the diphoton candidates was evaluated as a function of the transverse momentum (p_T) of the photons. It showed the large photon purity at high p_T region (0.6 at $p_T = 25$ GeV).

The differential cross section for the diphoton production was measured as a function of p_T of the photons, the invariant mass (M) of the diphotons, the azimuthal angle between diphotons ($\Delta\phi$), the ratio of the transverse momentum of the photons (Z) and p_T of the diphoton system. The results were compared with the NLO QCD predictions with CTEQ2M parton distribution functions. The results, as a function of p_T, M and $\Delta\phi$, showed qualitative agreements with the NLO predictions, while the results of Z and diphoton system p_T showed slight differences between the data and the theory.

The difference of the shape of the diphoton system p_T between the data and the theory was quantified with Kolmogorov-Smirnov test. The probability of the consistency between two distributions was estimated to be 0.13. We also checked the consistency between the data and Parton Shower Monte Carlo(PYTHIA), which includes the effects of the multiple initial soft gluon radiations and the intrinsic transverse momentum of the initial partons. It was estimated to be 0.91. PYTHIA explained the shape of the diphoton system p_T distribution better than the NLO.

Acknowledgements

This is an acknowledgement to all people who supported me during the doctor program.

This work was supported by the U.S. Department of Energy and National Science Foundation; the Italian Istituto Nazionale di Fisica Nucleare; the Ministry of Education, Science and Culture of Japan; the Natural Sciences and Engineering Research Council of Canada; the National Science Council of the Republic of China; and the A. P. Sloan Foundation.

Contents

The CDF Collaboration viii

1 Introduction 1

1.1 Large-Momentum-Transfer Production of Prompt Photons 1

1.2 Formalism 2

1.3 Next-to-Leading Order QCD Predictions 3

1.4 Study of the Background for Higgs Boson Hunting 4

1.5 Initial Soft Gluon Radiation and intrinsic k_T smearing 5

1.6 Previous Results for Diphoton Cross Section 5

1.7 Other Topics on Diphoton Production 6

1.8 Outline of the Thesis 7

2 The CDF Detector 17

2.1 Tracking chambers 18

2.1.1 Silicon Vertex Detector: SVX 18

2.1.2 Vertex time projection chamber: VTX 19

2.1.3 Central tracking chamber: CTC 19

2.2 Calorimetry 19

2.2.1 Central electromagnetic calorimeter: CEM 20

2.2.2 Central strip chambers: CES 21

2.2.3 Central Preradiator Detector: CPR 22

2.2.4 Central and Wall Hadron Calorimeter: CHA/WHA 22
2.2.5 Plug and Forward Calorimeters 22
2.3 Trigger and Data Acquisition System 23
2.3.1 Trigger System 23
2.3.2 Neural Network Hardware Trigger for Isolation Cut at Level 2 . . 23
2.4 Luminosity Measurement 24

3 Event Selection **30**
3.1 Cluster Finding Algorithm 30
3.2 Trigger Requirement 32
3.2.1 Level 1 Trigger Requirement 32
3.2.2 Level 2 Trigger Requirement 32
3.2.3 Level 3 Trigger Requirement 33
3.3 Offline Event Selection 34
3.3.1 Energy Correction and Transverse Energy Requirement 34
3.3.2 Calorimeter Isolation Cut 35
3.3.3 Lateral Shower Profile: χ^2 and Extra Cluster Cut in the CES . . 36
3.3.4 No-Track Requirement 39
3.3.5 Z vertex and Rapidity Cut 39
3.3.6 Final Diphoton Candidates 40
3.4 Efficiencies for the Trigger and Selection Cuts 41
3.4.1 Level 2 Trigger Efficiency 41
3.4.2 Calorimeter Isolation Cut Efficiency 42
3.4.3 CES Extra Cluster Cut Efficiency 42
3.4.4 Track Cut Efficiency 43
3.4.5 Summary of Efficiencies 43

4 Photon Identification **53**
4.1 Background Sources 53

4.2 Photon Identification Method 53
4.2.1 Profile and Conversion Method 54
4.2.2 Photon Identification on Event by Event Basis 57
4.3 CES Profile Method Efficiencies and Systematic Uncertainties 58
4.3.1 CES signal efficiency 58
4.3.2 CES background efficiency 59
4.3.3 Sources of the Systematic Uncertainties for CES Efficiencies . . . 61
4.3.4 Constraint on the CES Systematic Uncertainties with CPR 62
4.4 CPR Conversion Method Efficiencies and Systematic Uncertainties 63
4.4.1 CPR signal and background efficiencies 63
4.4.2 Calibration for the CPR Efficiencies with the Reconstructed Neutral Mesons 64
4.5 Sources of the Systematic Uncertainties for CPR Efficiencies 65
4.6 Photon Identification Method Combined with CES and CPR Efficiencies 65

5 Measuring the Diphoton Cross Section 79
5.1 Result of the Background Subtraction and Final Diphoton Events 79
5.2 Photon Fraction in Diphoton Candidates 80
5.3 The Diphoton Cross Section 81
5.3.1 Summary of the Systematic Uncertainties 81
5.3.2 Evaluation of the Diphoton Cross Section 82
5.4 Discussion 85
5.4.1 Effect of the Initial Soft Gluon Radiation and Intrinsic k_T 85
5.4.2 Kolmogorov-Smirnov Test for Diphoton System p_T Distribution . 85

6 Conclusion 95

A The Standard Selection Criteria for Electrons 96
A.1 The Selection Criteria for Electrons 96
A.1.1 3D Track Cut 96

A.1.2 E/P 97
A.1.3 Had/EM 97
A.1.4 Lateral Shower Sharing: L_{shr} 98

B Standard CES Profile **99**
B.1 Standard CES Profile 99
B.2 Strip/Wire Profile Differences 100
B.3 Parameterization of the CES Standard Profile 101
B.3.1 Parameterization of the Symmetric Profile 101
B.3.2 Parameterization of the Antisymmetric Profile 102
B.3.3 Energy Scaling of the Variance 102

Bibliography **105**

Chapter 1

Introduction

1.1 Large-Momentum-Transfer Production of Prompt Photons

The Quantum Chromodynamics (QCD) [1] has been explaining the dynamics of the collisions between hadrons. One of the key feature of the theory is the property of asymptotic freedom [2][3], which describes the weakening of the effective quark-gluon coupling at short distances or, equivalently, large momentum transfers. The characteristic of asymptotic freedom allows application of perturbative techniques to the problem of short-distance interactions. The large-momentum-transfer processes in hadron-hadron collisions have played an important role of testing the QCD.

In the Collider Detector at Fermilab (CDF), various physics processes in hadron-hadron collisions were used to test the QCD; for example, lepton pair production [4], Z boson plus jet production [5], and inclusive jet cross section [6]. All of the results showed the qualitative agreement with the QCD predictions.

The prompt photon production with large transverse momentum in hadron - hadron collisions is also good probe for testing the QCD [7]. Although the cross section of

the prompt photon production is small compared with that of the jet production, the momentum of the photons in the final state can be strictly measured with the electromagnetic (EM) calorimeter which has a fine energy resolution, rather than measuring the momentum of the jets, which must be measured with both the EM and the hadron calorimeters and the resolution of the hadron calorimeter is worse than the EM calorimeter.

Measurement of the diphoton production in hadron - hadron collisions is thus important for testing the QCD. The number of Feynman diagrams used in the QCD predictions are restricted by requiring the existence of the two photons in the final state. The Feynman diagrams for the leading-order diphoton processes are shown in Fig. 1.1.

1.2 Formalism

In the parton model, developed by Feynman [8] and Bjorken & Paschos [9], the hard scattering is described by the leading-order subprocesses which, for jet or photon productions with large transverse momentum (p_T), correspond to two body scattering. Figure 1.2 shows the schematic drawing of such a high p_T process in hadron-hadron collisions, where A and B are the initial hadrons, C and D are the final state objects after the fragmentation processes. The corresponding expression for the invariant cross section of the particle C is

$$E_C \frac{d\sigma}{d^3p_C}(AB \to C + X) = \sum_{abcd} \int dx_a dx_b dz_c G_{a/A}(x_a, Q^2) G_{b/B}(x_b, Q^2) D_{C/c}(z_c, Q^2) \times \frac{\hat{s}}{z_c^2 \pi} \frac{d\sigma}{d\hat{t}}(ab \to cd) \delta(\hat{s} + \hat{t} + \hat{u}) \,, \quad (1.1)$$

where p_C is the momentum of outgoing particle C, x_a and x_b are the momentum fractions of the parton a and b with respect to the initial hadrons A and B, $G_{a/A}(x_a, Q^2)$ and $G_{b/B}(x_b, Q^2)$ are the distribution functions of the parton a and b, respectively, $D_{C/c}(z_c, Q^2)$ is the fragmentation function of the particle C from parton c, $\hat{s}$, $\hat{t}$ and $\hat{u}$ show the Mandelstam variables for the hard collision of the partons $ab \to cd$, $\frac{d\sigma}{d\hat{t}}$ is the

invariant differential cross section for the two-body parton scattering subprocess.

The parton model describes that the structure functions should be represented as a function of only x; the functions scale with x, they are not as a function of momentum transfer Q^2. While in view of the QCD, where we consider the contribution of the gluons in the physics processes, the scaling properties of the structure functions and the fragmentation functions are no more true, both functions are as a function of x, as well as the momentum transfer Q^2.

Theoretical efforts on the parametrizations of a set of Q^2-dependent nucleon-parton distribution functions have been made for the physics processes in high energy hadron-hadron collisions with the data from deep inelastic scattering, J/Ψ and high-mass dilepton production [10], where the Q^2 evolution of these distribution functions are calculated with the Altarelli-Parisi equations [11]. The global fits to the recent results from various standard experiments (deep inelastic experiments, lepton-pair production experiments and direct photon production experiments), have been also done to determine more sophisticated parton distribution functions [12].

The invariant cross sections for the leading-order subprocesses shown in Fig. 1.1 are calculated in [7].

1.3 Next-to-Leading Order QCD Predictions

The next-to-leading order(NLO) QCD predictions for the diphoton production were evaluated by Bailey *et al.* [13]. Following diphoton processes were included in this calculation,

1. leading order Born process (Fig. 1.1 (a)),

2. leading order Box process (Fig. 1.1 (b)),

3. contributions of single- and double-photon bremsstrahlung[1] (Fig. 1.3),

[1]This item includes both 3-body or 4-body final states and also the collinear pieces that use photon fragmentation functions. The photon fragmentation functions are evolved with Q^2 just as the usual

4. Born processes with one virtual gluon exchange (Fig. 1.4),

5. Born processes with one real gluon emission (Fig. 1.5).

Single-photon bremsstrahlung contribution to the diphoton production was calculated with the 2→2 direct photon subprocess cross sections. In this analysis we used CTEQ2M parton distribution functions [12]. Double-photon bremsstrahlung process was also calculated with the 2→2 QCD subprocess cross sections. In the 2→3 QCD subprocesses, 3-body phase space was evaluated with the Monte Carlo techniques.

The largest difference between NLO and Parton-shower Monte Carlo is that the NLO only includes one gluon emitting at the initial state, while the Parton-shower Monte Carlo is allowed many initial gluon radiations at the initial state, shown in Fig. 1.6.

We use this NLO prediction for comparing with the diphoton data. Figure 1.7 shows the theoretical prediction for the NLO QCD calculations as a function of the transverse momentum (p_T) of the photons. Here we put two entries in one event. The momentum transfer Q^2 was chosen to be p_T^2 of the leading photons. It indicates that we will have the diphoton events up to around 70 GeV with the integrated luminosity of 110 pb^{-1}, assuming the acceptance of the photon detection to be 1.

1.4 Study of the Background for Higgs Boson Hunting

The QCD diphoton production is the only dominant physics background for search for the Higgs bosons decaying to two-photons with large transverse momentum [14] for future hadron collider (LHC). The consistency between the experimental result of the diphoton cross section and the theory should be checked for the background study for this decay mode. The CDF and DØ experiments are the only experiments for this purpose.

hadronic fragmentation functions are done [7].

1.5 Initial Soft Gluon Radiation and intrinsic k_T smearing

Recent result of the inclusive photon cross section measurement done at CDF [15] shows that the result is in agreement with the NLO QCD predictions but has the steeper slope above the theory at low p_T region. Figure 1.8 shows the result of the inclusive photon cross section as a function of p_T of the photons, and variations of different parton distribution functions, where (data-theory)/theory is shown in linear scale. CTEQ group reported that such a shape was seen in other inclusive photon measurements done at various fixed target experiments, and one of the idea to understand the shape was that the shape could be occurred by the transverse momentum of the initial partons, which is caused by the multiple initial soft gluon radiations, as well as the intrinsic transverse momentum of the partons[2] in the hadrons. Both effects are beyond the NLO predictions. The p_T distribution of the photons is smeared by these effects. Theoretical efforts of explaining the slope of the inclusive photon cross section is in progress with the help of the Monte Carlo techniques which take these effects into account [17].

The diphoton production in hadron - hadron collisions is one of the clear probe for measuring the effects by measuring the p_T of the diphoton system, which corresponds to the p_T of the system of the initial partons.

1.6 Previous Results for Diphoton Cross Section

There are many experimental results of measuring the cross section for prompt photon production. The results of the early experiments with fixed targets are reported in [18], as well as the report of the comparison of the data with the early theoretical works described in [7].

[2]In the parton model approach it is assumed that the average value of the intrinsic transverse momentum reflects the size of the hadron via the uncertainty principle. This leads to the expectation that $< k_T >$ may be in the range of several hundred MeV [7].

p_T bin (GeV/c)	Mean p_T (GeV/c)	$d\sigma_{\gamma\gamma}/dp_T$(pb/GeV/c)	Stat. (%)	Sys. (%)
10-12	11.1	17.5	57	+31 -21
12-15	13.5	11.6	46	+45 -35
15-19	17.4	4.2	65	+41 -29
10-19	13.3	9.6	31	+37 -27

Table 1.1: The diphoton cross section as a function of photon p_T from the total integrated luminosity of $4.3\,\mathrm{pb}^{-1}$. Statistical and systematic errors are also listed.

The first measurement of the diphoton cross section in $\bar{\mathrm{p}}\mathrm{p}$ collision was done at UA2 and UA1 collaboration with CERN Sp$\bar{\mathrm{p}}$S collider at $\sqrt{\mathrm{s}} = 630\,\mathrm{GeV}$ [19][20]. UA2 showed the result with large statistics. It showed the agreement with the NLO QCD prediction.

CDF already published the result of the diphoton cross section with the total accumulated luminosity of $4.3\,\mathrm{pb}^{-1}$ [21]. Figure 1.9 shows the results of the cross section as a function of the transverse momentum of the photons. Numerical values of the cross section are shown in table 1.1 with the statistical and the systematic errors. The result was about 3 times higher than the NLO QCD prediction.

1.7 Other Topics on Diphoton Production

In 1996, CDF detected a diphoton candidate, both of which had a large transverse momentum. This event also contained one electron and one "electron like" particle, and large missing E_T. CDF has investigated the event, as well as more general property of "diphoton plus missing E_T" events [22]. It was reported that the shape of missing E_T distribution for diphoton events was consistent with that of Drell-Yan events.

1.8 Outline of the Thesis

In this thesis we present the result of the measurement of the cross section for diphoton production at a center-of-mass energy $\sqrt{s} = 1.8$ TeV. The data were accumulated using CDF detector. The total integrated luminosity was about $110\,\mathrm{pb}^{-1}$ during 1992-1995 Fermilab Tevatron collider run. Each component of the CDF detector will be described in Chapter 2, including trigger system. In chapter 3 we shows the criteria for selecting diphoton candidates, and evaluation of their efficiencies for real diphoton events. Chapter 4 describes the extraction of the prompt diphotons from neutral mesons decaying to multiple photons. Since the backgrounds are not discriminated from real diphoton signals event by event, we evaluated the statistical method with the information from the electromagnetic shower profile at the shower maximum region and the conversion rates in front of the calorimeter. A photon fraction in the final diphoton candidates is shown in chapter 5, where we present the differential cross section as a function of transverse momentum of the photons, invariant mass of the diphotons, azimuthal angle between two photons, the ratio of p_T for diphotons; $Z = p_T^{(2)}/p_T^{(1)}$, and transverse momentum of the diphoton system. The results are compared with the NLO QCD prediction. Systematic uncertainties of this cross section measurement are also summarized.

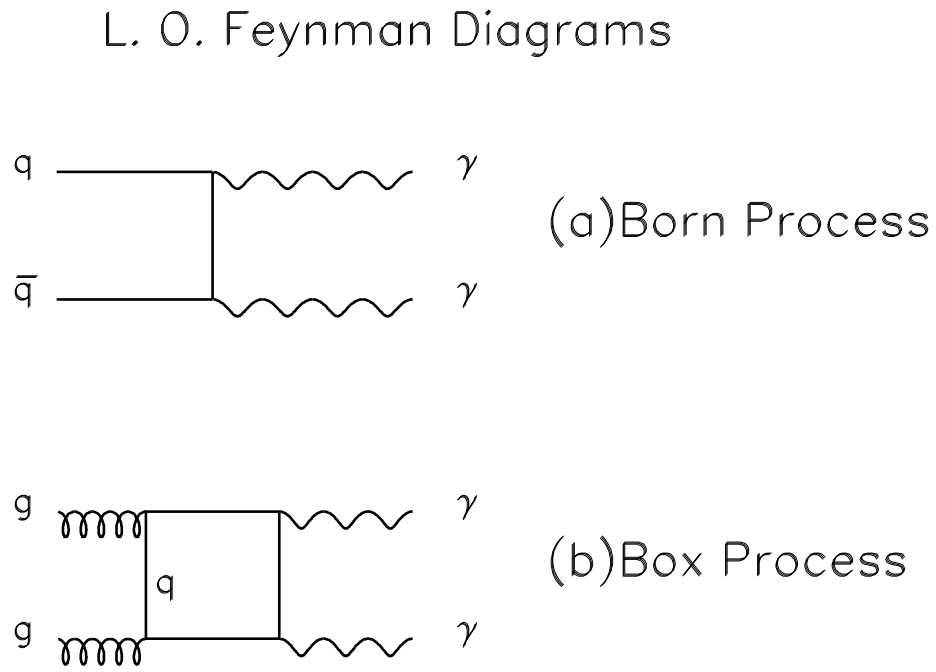

Figure 1.1: Leading-order Feynman diagrams for the diphoton production, (a) Born process, (b) Box process.

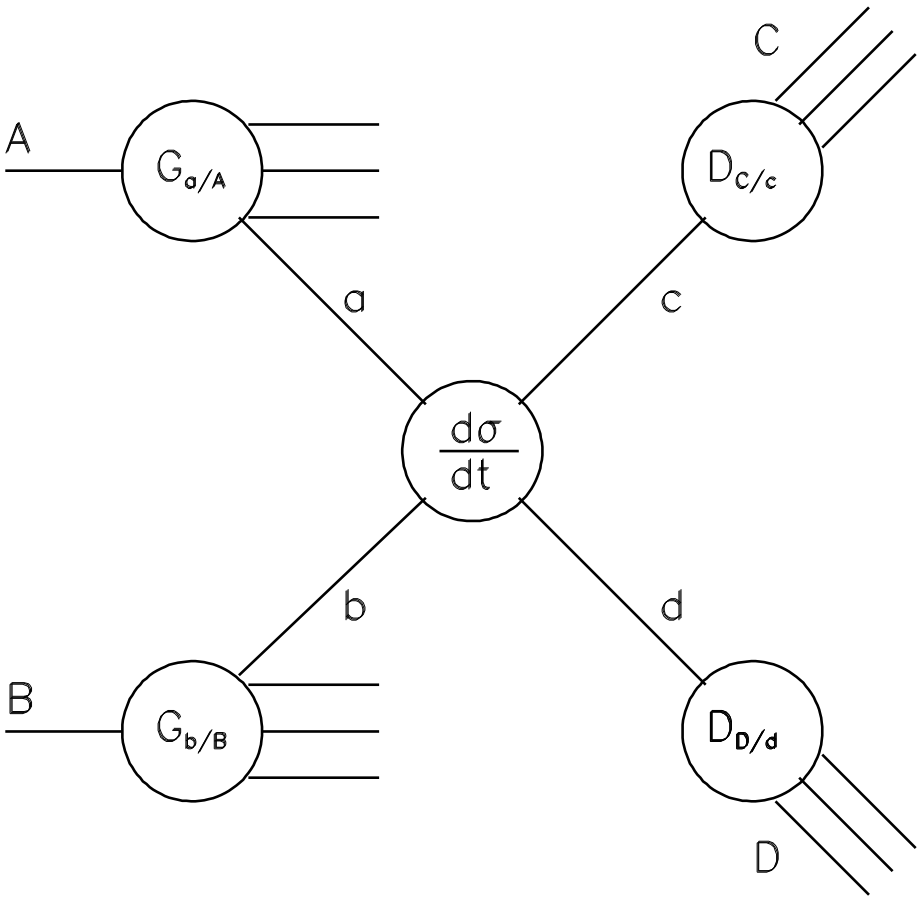

Figure 1.2: Schematic drawing of a high p_T reaction factorized into parton distribution functions (G), parton fragmentation functions (D), and a hard scattering subprocess.

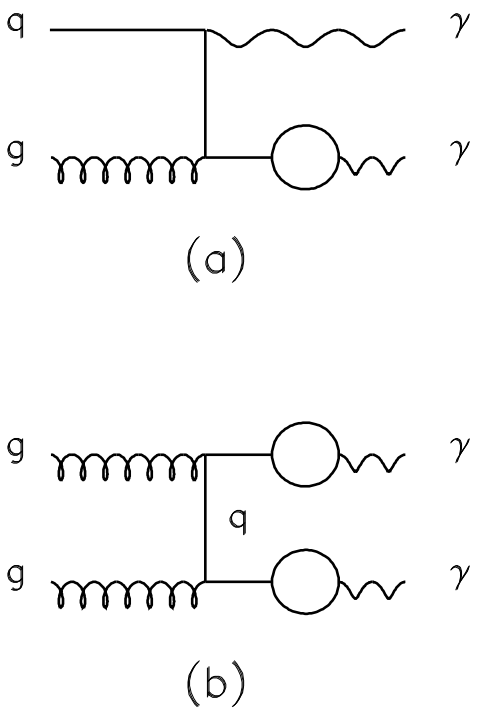

Figure 1.3: Feynman diagrams used in the NLO predictions for diphoton production from the contributions of (a) one photon fragmentation process and (b) diphoton fragmentation process. Circle shows the fragmentation process for the final state quark.

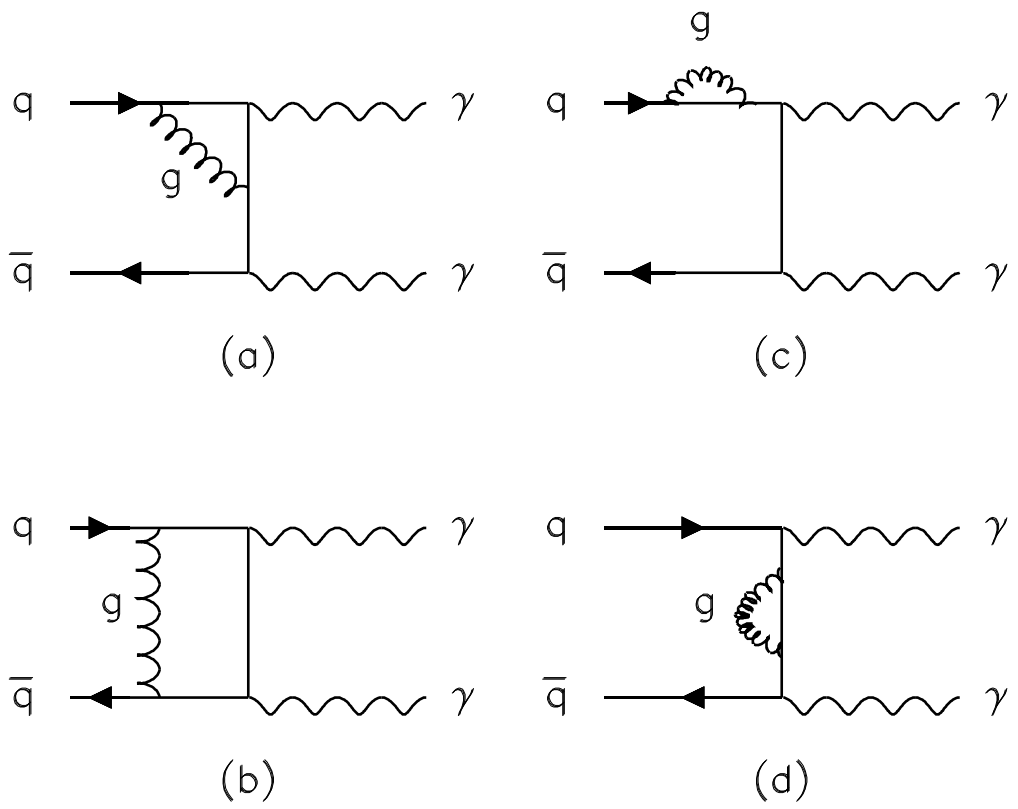

Figure 1.4: Feynman diagrams used in the NLO predictions for diphoton production with one virtual gluon exchange.

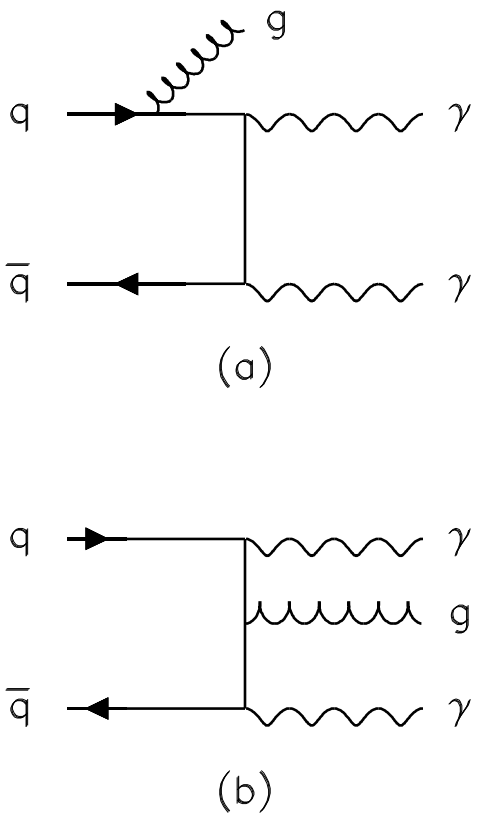

Figure 1.5: Feynman diagrams used in the NLO predictions for diphoton production with one real gluon emission.

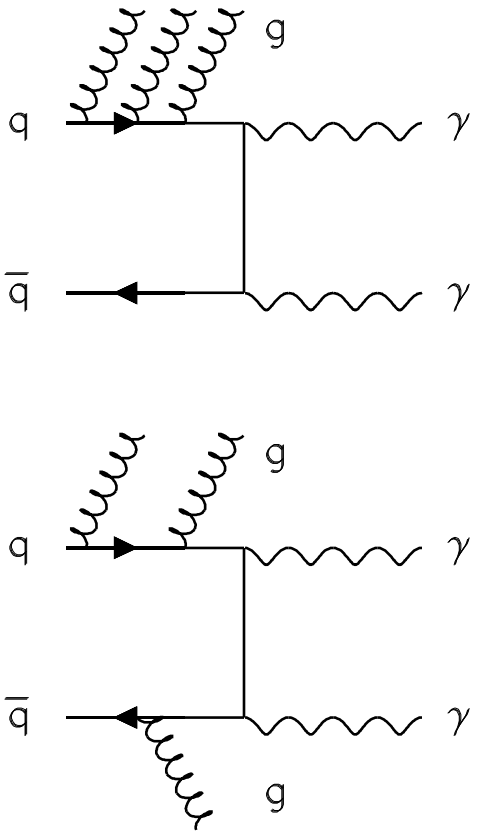

Figure 1.6: Examples of the Feynman diagrams of the initial state soft gluon radiations for diphoton production in the Parton-shower Monte Carlo.

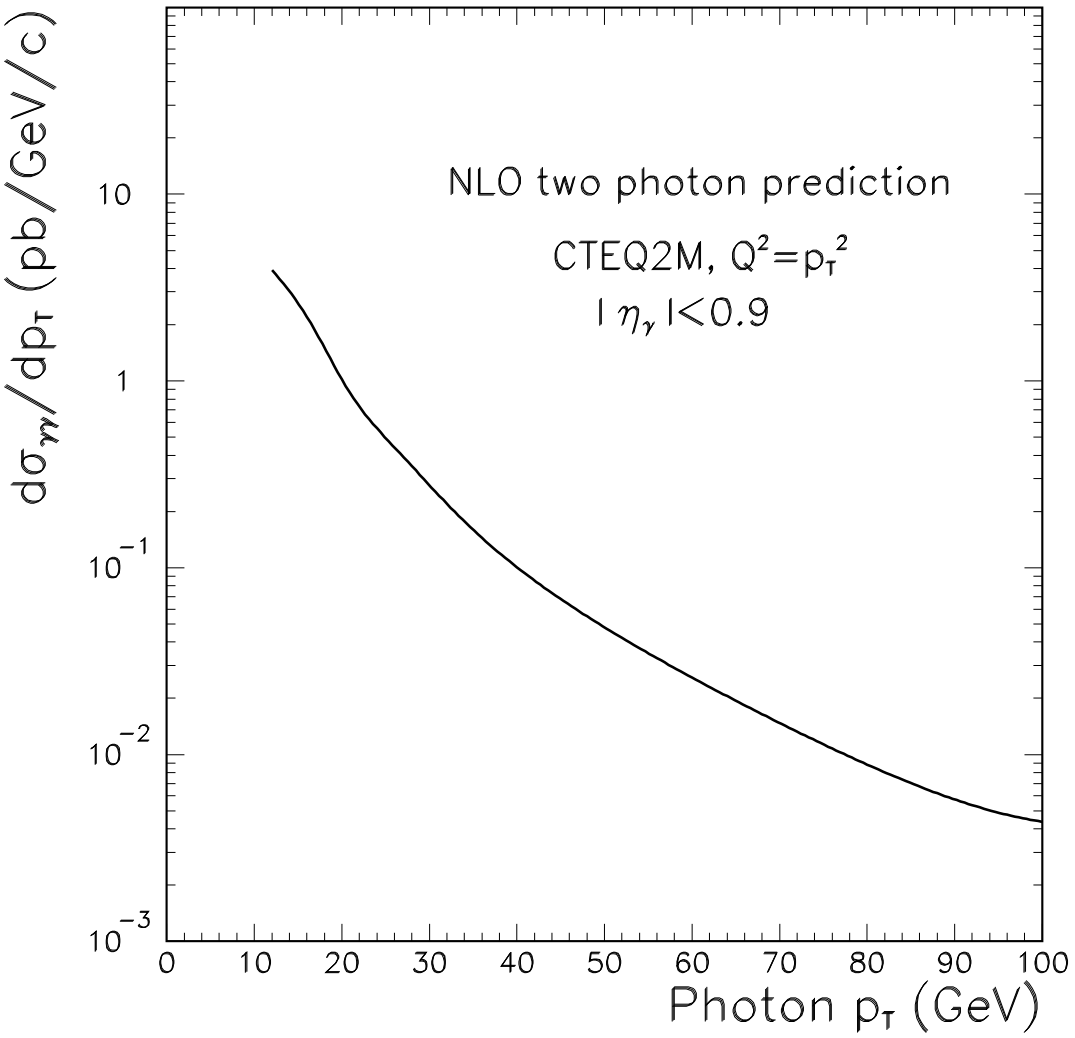

Figure 1.7: The prediction of the diphoton cross section of the NLO calculation, as a function of the transverse momentum of the photons.

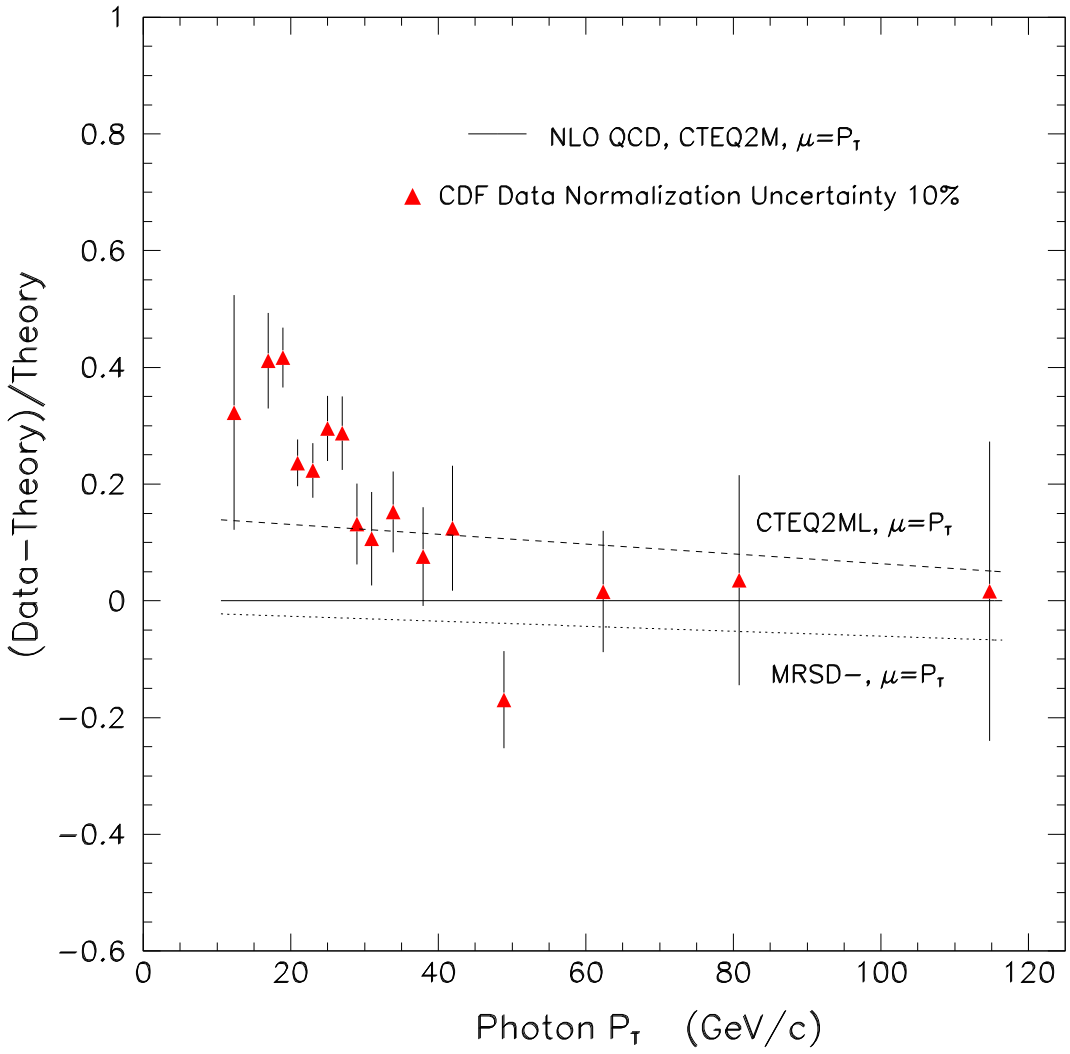

Figure 1.8: The result of the inclusive photon cross section measurement done at CDF as a function of p_T of the photons, where (data-theory)/theory is plotted. Variations from different parton distribution functions are also shown. Solid line shows the NLO prediction with CTEQ2M parton distribution functions, dashed line shows that with CTEQ2ML, dotted line shows that with MRSD- parton distribution functions.

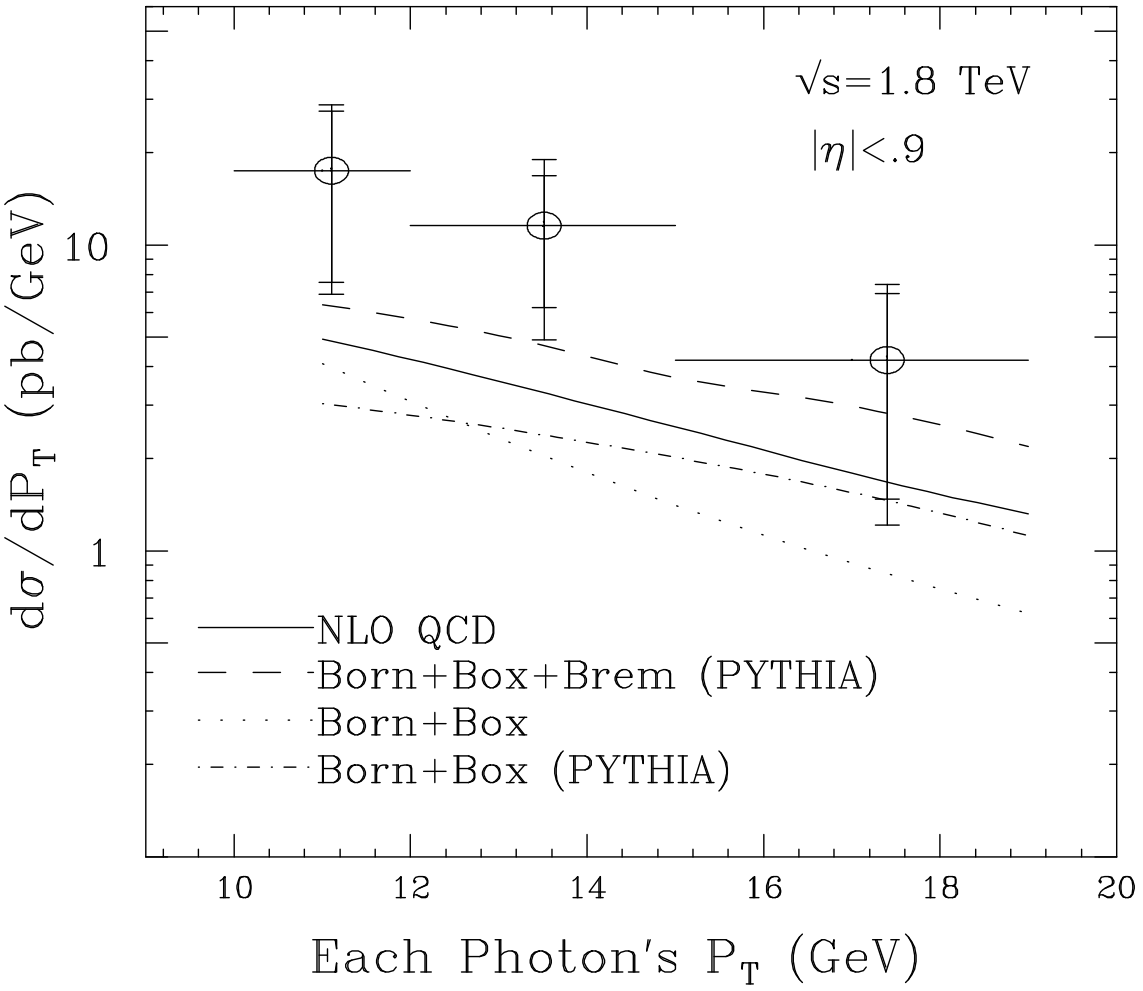

Figure 1.9: The published result of the diphoton cross section as a function of the photon p_T measured at CDF. The total accumulated luminosity was 4.3pb^{-1}. The data were compared with the NLO(solid), LO(dotted) QCD predictions, PYTHIA LO with(dashed) and without(dot-dashed) bremsstrahlung contributions.

Chapter 2

The CDF Detector

In this chapter we describe the experimental apparatus, the Collider Detector at Fermilab (CDF). We will emphasize the descriptions on the central part of the CDF detector, especially for the central electromagnetic calorimeter, where our sample of the two photon candidates is selected and used for the study of the two photon cross section.

The CDF detector [23] is a general purpose superconducting-solenoid-magnetic detector which was designed for studying the proton-antiproton collisions at the center of mass of 1.8 TeV. The detector covers almost of the solid angle, down to 2° with respect to the beam direction and 2π in azimuth. It consists of three parts, central, forward and backward, as shown in Figure 2.1.

The apparatus is divided in roughly three categories; tracking device, calorimetries and the muon detection system. The tracking systems measure the tracks of individual charged particles. The calorimetries are used to measure the energy deposition of particles from the collision. Muon system is designed to detect the particles penetrating outside the calorimeters.

2.1 Tracking chambers

In the central region of the detector (Figure 2.2), tracking chambers reside within a 1.4 T solenoid coil [24]. They allow precise momentum analysis of charged particles. We describe three tracking chamber systems below.

2.1.1 Silicon Vertex Detector: SVX

The silicon vertex detector (SVX) was installed at the beginning of the 1992 collider run, which was designed to detect the secondary vertices which was caused by the Lorentz boost of the heavy mesons with the long life times, especially the mesons from the b quark fragmentations.

SVX covers the z range from 0 cm to ± 51 cm with two barrel modules contacting at $z = 0$ cm. Each barrel consists of four concentric cylindrical layers of DC-coupled silicon microstrips. Each layers located surrounding the beam pipe: 3.005 cm from the beam line for the innermost layer, 4.256 and 5.687 cm for the middle two layers, and 7.866 cm for the outermost layer. The silicon microstrips are 8.5 cm long and 300 μm thick with a strip pitch of 60 μm for the inner three layers and 55 μm for the fourth layer. The tracks of the charged particles in $R - \phi$ plane are reconstructed with the charge distribution of each layers. The position resolution of the SVX in the $R - \phi$ plane is about 13 μm at a track transverse momentum of 3.5 GeV/c.

The informations from the SVX are used to determine the track parameters of the charged particles with the CTC as follows: first all tracks are reconstructed only with CTC, then the tracks are extrapolated to each SVX layers. At least 2 hits in the four layers is the criterion to reconstruct the track parameters with both CTC and SVX informations. The self reconstruction of the track parameters with SVX is not done.

2.1.2 Vertex time projection chamber: VTX

The vertex time projection chamber (VTX) is located just outside the beam pipe. After 1988-1989 CDF collider run, the VTX was installed by replacing the similar chamber called VTPC [25]. Most of the characteristics of the module in the VTX is the same as that in the VTPC.

It consists of 28 time projection chamber modules along the beam direction z, and has a good track reconstruction capability in R-z plane. The main role of the VTX is to determine the primary event vertex along the beam axis. The VTX determines the event vertex with an accuracy of about 3 mm.

2.1.3 Central tracking chamber: CTC

The central tracking chamber (CTC) [26] is a large cylindrical drift chamber, 1.3 m in diameter and 3.2 m long (figure 2.3). It is located outside the VTX and covers the angular region $40° < \theta < 140°$ ($-1 < \eta < 1$). The chamber consists of 84 layers of sense wires grouped into 9 "superlayers". Five of them consist of 12 axial wires, and four of them consist of 6 stereo wires which have angles of $\pm 3°$ relative to the beam direction. The resolution of a single hit point is about 200 μm, and gives a momentum resolution of

$$\Delta p_T / p_T \simeq 0.002\, p_T, \tag{2.1}$$

where p_T is the transverse momentum of a charged particle in GeV/c.

2.2 Calorimetry

A calorimetric device plays an important role in high energy experiments, especially in hadron collider experiments. This is because it can measure the energy of neutral particles as well as charged particles. Identification of a particular class of particles, an electron or photon for example, is also possible. Especially for the electromagnetic

calorimeters, the resolution of the energy of the particle become more precise at high E_T, which enables us to make the resolution of the various physics variables (momentum of the electrons, the invariant mass of the two electron pair, etc.) more precise than that from CTC.

Calorimeters are segmented into towers with projective geometry; each tower points back to the nominal interaction point. The size of the tower is typically 15 degrees in azimuth and 0.1 in pseudorapidity η, defined by $\eta = -\ln\tan\theta/2$, where θ is the polar angle with respect to the proton beam direction (z). The pseudorapidity rather than θ is used as the tower segmentation variable because the distributions of any particles or hadronic jets in hadron colliders are roughly flat in this variable.

The CDF calorimeters consist of three parts (central, plug and forward) depending on the angular region. Each calorimeter has two longitudinal components, the electromagnetic in front and the hadronic behind. In this way an electromagnetic shower can be separated from a hadronic shower, because an electromagnetic (hadronic) shower has a faster (slower) development as a function of the amount of materials a particle passes through. All CDF calorimeters are of the sampling type, which consists of a passive absorber to create particle showers and an active medium to detect secondary particles in the showers.

2.2.1 Central electromagnetic calorimeter: CEM

The CDF central electromagnetic calorimeter (CEM) [27] consists of alternative layers of a plastic scintillator as a sampling medium and a lead sheet as a showering material. It is segmented into 24 modules in azimuth, and two along the beam direction, total of 48 wedge shaped modules (Figure 2.4). A "wedge" module has 10 towers, each of which covers 15 degrees in azimuth and 0.1 in η.

The CEM has 31 scintillator and 30 lead layers, corresponding to a total amount of materials of 16 radiation lengths (X_0). The layers are placed parallel to the beam line.

A typical size of a tower cell is 46 cm in R-ϕ (x) direction and 24 cm along the beam

direction z. This is larger than the size of the electromagnetic showers, which is only a few cm's wide laterally.

Scintillation lights are converted in two wavelength shifter plates located at ϕ-boundaries of a tower, and are guided through light pipes to photomultiplier tubes (PMTs). Optical properties of the scintillator (SCSN-38) and the wavelength shifter (Y7) are used. A large number of average output photons from each scintillator-lightguide system in one tower makes the degradation of the energy resolution from the statistical fluctuation keep small.

Each of the CEM towers is calibrated using the electron beam of 50 GeV momentum. The calibration is maintained using the ^{137}Cs radioactive sources for the overall calorimeter response and the LED and Xenon flasher system for the phototubes and lightguides.

The energy resolution of the CEM is measured using the test beam electrons to be

$$\frac{\sigma(E)}{E} = \frac{0.135}{\sqrt{E \sin\theta}}, \tag{2.2}$$

where E is the energy measured in GeV and θ is the polar angle. The dependence on the polar angle is due to the increase in the absorber thickness in lower angle towers.

2.2.2 Central strip chambers: CES

A layer of wire proportional chamber (CES) is placed at near shower maximum of the CEM (nominal depth at 5.9 X_0 including the coil). A chamber has two orthogonal views, anode wires measuring the R-ϕ view of the showers and cathode strips measuring the z view. A channel has a typical width of 1.5 cm. The fine segmentation enables us to measure more precise profiles of showers than with CEM towers. The position resolution of a few mm's is achieved for electromagnetic showers.

In the physics analysis, we use the local coordinates in CES module to define the same fiducial volume of each CES module. Figure 2.5 shows the schematic drawing of

the CES local coordinates.

2.2.3 Central Preradiator Detector: CPR

The central preradiator detector (CPR) [28] was installed at the beginning of the 1992 collider run, which detects the particle showers started by the preshower materials (coil and cryostat) placed in front of the CEM. Output charge from the CPR enables us to get informations for estimating conversion probability of the electrons, photons and pions, which become the powerful informations for extracting electrons/photons from background hadrons. Thus the CPR plays a important role on this analysis.

CPR consists of the multi-wire gas proportional gas chamber as the detection device. There are two MWPC modules located in front of each CEM wedge. In each CPR module there are 32 sense wires and 31 field wires which are along with z axis. The total amount of the material of the CPR is about 3% of a radiation length and 1% of an interaction length.

2.2.4 Central and Wall Hadron Calorimeter: CHA/WHA

Behind the CEM there exist the central (CHA) and the wall (WHA) hadron calorimeters [31]. They both consist of layers of plastic scintillator and iron absorber. Towers have the same segmentation as the CEM.

2.2.5 Plug and Forward Calorimeters

Calorimeters covering the plug ($1.1 < |\eta| < 2.4$) and forward ($2.2 < |\eta| < 4.2$) regions of the detector employ gas proportional chambers with cathode pad readout as detection device, and lead and iron plates as showering material for electromagnetic and hadron components, respectively. A tower size of $\Delta\eta \times \Delta\phi = 0.1 \times 5^\circ$ is used.

2.3 Trigger and Data Acquisition System

2.3.1 Trigger System

The CDF trigger is divided in four levels, level 0, 1, 2 and 3. The level 0 trigger requires the signature of an inelastic collision, which is defined by the coincidence of the beam-beam counter (BBC) systems. The BBC consists of the scintillator hodoscopes located in front of the forward and the backward detectors.

The level 1 and 2 triggers use signals from the calorimeters and the tracking chambers to make decisions on the events. Calorimeter signals are summed into trigger towers with a size of $\Delta\eta \times \Delta\phi = 0.2 \times 15^{\circ}$. In this way the whole CDF calorimeter is represented by a 42×24 array for both electromagnetic and hadronic energies.

The level 1 trigger makes a decision based on calorimeter signals in excess of a programmable threshold, a stiff CTC track from a fast hardware track processor [32], and the muon triggers [33]. The level 2 trigger can form clusters of energies using the 42×24 array. The extra module for isolation cut is used in the triggers for electrons and photons, which is described later.

The level 3 trigger system performs a more sophisticated event selection by executing FORTRAN-77 programs in the UNIX-based data acquisition machines.

The trigger system for two photons used in this analysis will be described in details in Chapter 3.

2.3.2 Neural Network Hardware Trigger for Isolation Cut at Level 2

In 1992-1995 collider run, a hardware trigger module for isolation cut was installed for electron and photon selection [34], which consists of the special IC chip used for the Neural Network (NN) system.

The trigger system was used as follows: first the IC chip studies the isolation pattern around the trigger tower with the simulations, then the simple pattern recognition was used to discriminate the non-isolated events at the hardware trigger level. More details can be seen in [34].

2.4 Luminosity Measurement

The luminosity can be obtained by counting the rate of a certain process of which cross section is known. We use inelastic $\bar{p}p$ events, and the BBC's to detect them. That is, we have

$$\mathcal{L} = \frac{R_{\rm BBC}}{\sigma_{\rm BBC}}, \tag{2.3}$$

where $\mathcal{L}$ is the luminosity, $R_{\rm BBC}$ is the BBC event rate, and $\sigma_{\rm BBC}$ is the effective cross section visible to the BBC's. We estimate $\sigma_{\rm BBC}$ at 1800 GeV as follows.

We first calculate the corresponding quantity for the UA4 experiment at 546 GeV, using their absolute measurements of the total and elastic $\bar{p}p$ cross sections, to be 38.9 ± 1.8 mb. A small correction due to the difference in the geometry of the trigger counters at CDF and UA4 is made in order to convert the above quantity into the corresponding CDF quantity at 546 GeV, $\sigma_{\rm BBC}^{546}$. We then relate it to the value at 1800 GeV, $\sigma_{\rm BBC}^{1800}$, by using the measurements of the Tevatron luminosities ($\mathcal{L}_{\rm acc}$) based on accelerator parameters, and the observed BBC rates $R_{\rm BBC}$ at the two energies. They have a relation

$$\frac{\sigma_{\rm BBC}^{1800}}{\sigma_{\rm BBC}^{546}} = \frac{R_{\rm BBC}(1800)}{R_{\rm BBC}(546)} \cdot \frac{\mathcal{L}_{\rm acc}(546)}{\mathcal{L}_{\rm acc}(1800)}. \tag{2.4}$$

We obtain

$$\sigma_{\rm BBC}^{1800} = 46.8 \pm 3.2 \text{ mb}, \tag{2.5}$$

or a 8% uncertainty in the luminosity measurement.

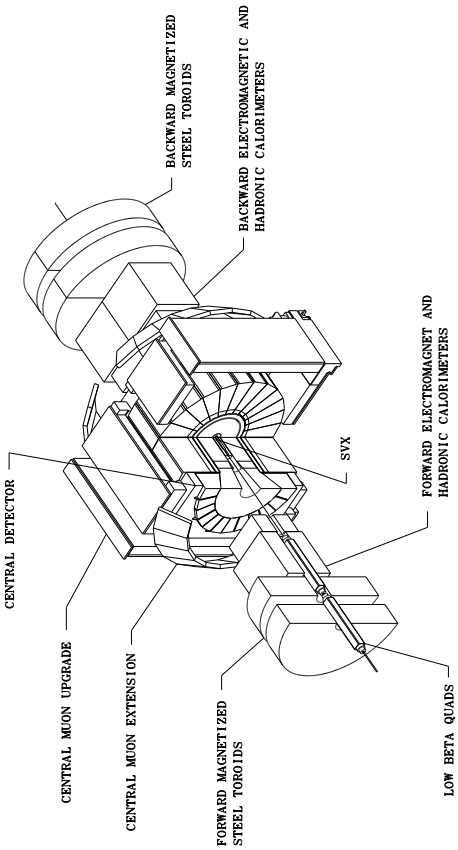

Figure 2.1: Schematic perspective view of the CDF detector.

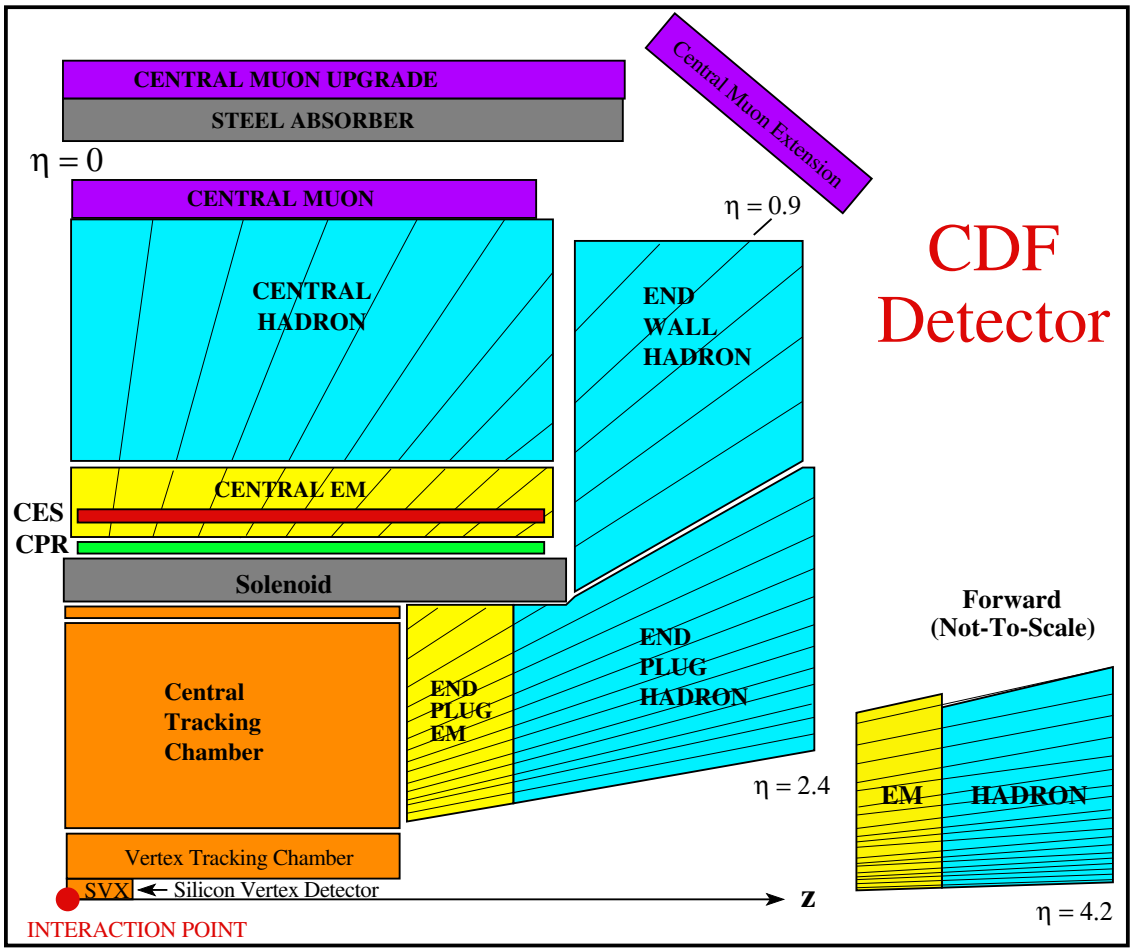

Figure 2.2: Schematic quarter section of the CDF detector.

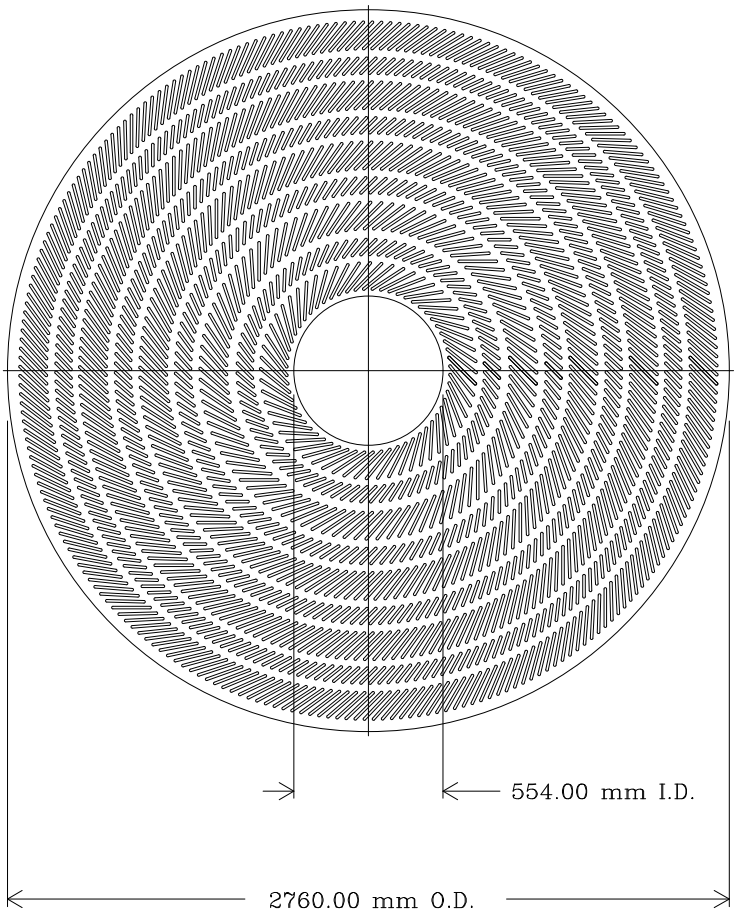

Figure 2.3: Schematic view of an endplate of the CTC showing the arrangement of the blocks which hold the 84 layers of sense wires.

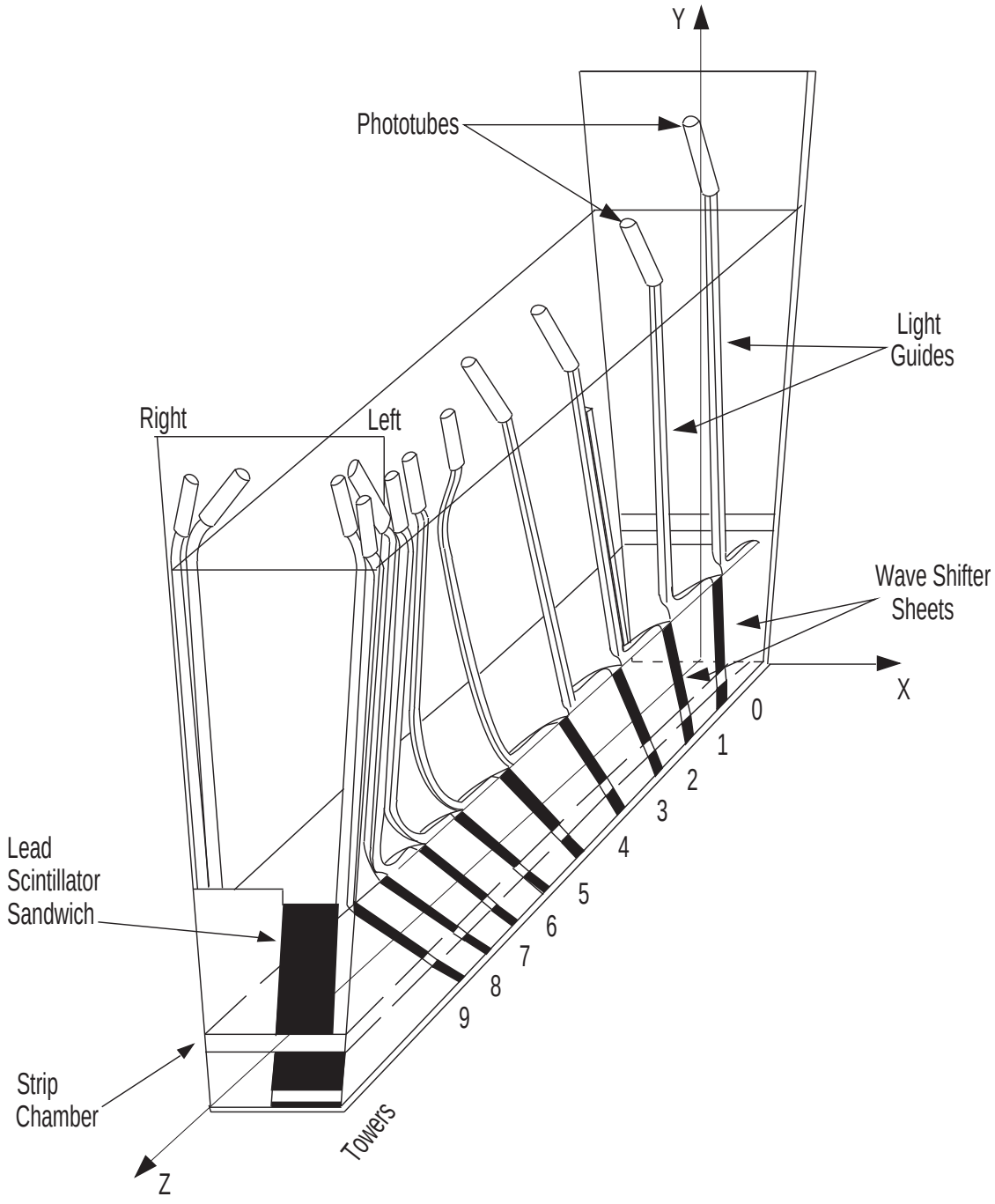

Figure 2.4: A module of the central electromagnetic calorimeter (CEM).

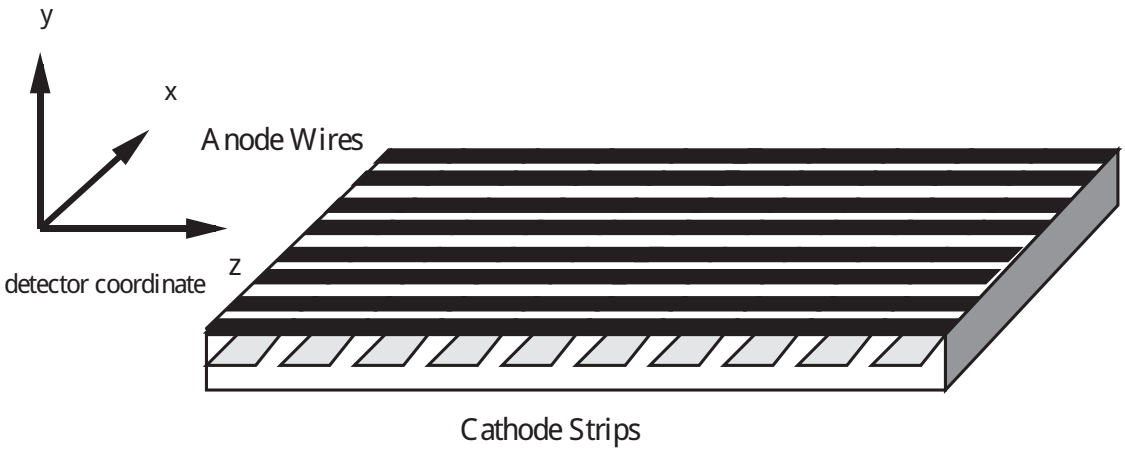

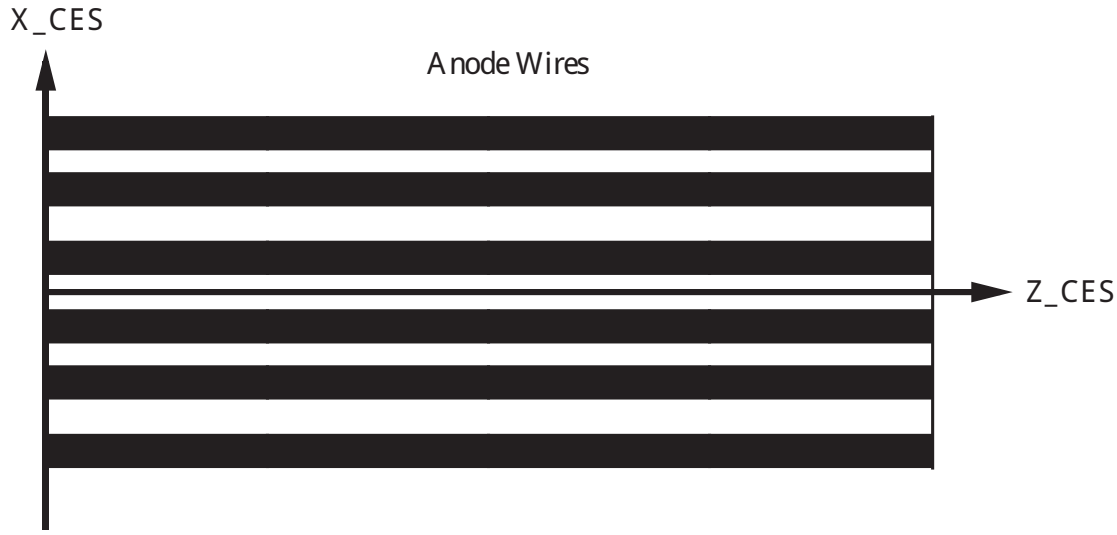

Figure 2.5: Schematic drawings of the CES and its local coordinates.

Chapter 3

Event Selection

In this chapter we present the criteria for selecting two photon candidates from the CDF data, and their efficiencies for real two photon events.

The basic idea of the background subtraction used in this analysis is to use the lateral shower profile at shower maximum region in the CES, and photon conversion rate in a material measured by the CPR. Although the CDF calorimetries cover almost of the polar angle, but for this reason, we use only CEM in both on-line and off-line levels in this analysis.

3.1 Cluster Finding Algorithm

The signature of the prompt two photon production is seen in the calorimetries to have two large and isolated electromagnetic energy depositions. The CDF two photon trigger finds this signature to acquire the refined data.

In order to reconstruct the correct energy for electrons and photons from energy depositions in each CEM tower, clustering of the energy depositions is needed. The clustering algorithm is as follows; first we look for the EM towers above the threshold energy (typically 3 GeV in the transverse energy), which will be the seed towers of the EM clusters. Then we add the energy depositions of the two adjacent towers (energy

threshold is typically 0.1 GeV in the transverse view) along with the z axis. The cluster width is, therefore, $\Delta\phi = 15°$ and $\Delta\eta = 0.3$. Thus the clustered energy $E^{cluster}$ is denoted by

$$E^{cluster} = E^{seed}_{\eta=\eta_s} + E_{\eta=\eta_s-0.1} + E_{\eta=\eta_s+0.1}, \tag{3.1}$$

where η_s is the pseudorapidity of the seed tower. This calculation is done for each EM seed tower.

At the level 2, the transverse energy is calculated using detector rapidity of the seed tower, assuming that the corresponding particle comes from $z = 0$, that is, the collision occurs at the center of the detector,

$$E_T = 2E \arctan(e^{-\eta}) \tag{3.2}$$

where E is the total deposited energy in a cluster, η is the pseudorapidity of the seed tower.

At the level 3 and offline level, we have information of the event vertices along the z-axis from the VTX and of the position of the EM showers from the CES. The polar angle of a EM cluster is calculated from the measured event vertex position in the VTX and the measured EM shower position in the CES. The transverse energy is calculated by

$$\begin{aligned} E_T &= E \times \sin\theta \\ &= E \times \frac{\sqrt{R^2_{CES} + X^2_{CES}}}{\sqrt{R^2_{CES} + X^2_{CES} + Z^2_{vetex}}}, \end{aligned} \tag{3.3}$$

where E is the total deposited energy of the cluster, R_{CES} is the radius of the CES cylinder, X_{CES} is the x position in the CES coordinate measured by the CES wire chamber (see Chapter 2), and Z_{vertex} is the z position of the event vertex reconstructed by the VTX.

3.2 Trigger Requirement

The CDF trigger system consists of various physics triggers. The lowest physics trigger is called "minimum bias trigger", which is used to check the detector system or to evaluate the efficiency for the event selection used in the physics analysis. The physics trigger has the rank from level 1 to level 3. The level 1 and the level 2 trigger consist of the hardware modules. The level 3 trigger consists of the online software systems.

We used the diphoton trigger system to select the diphoton dataset. The events with two EM clusters in the CEM are accumulated by the hardware trigger system at Level 1 and 2, then they are discriminated with the online software system at the level 3. The diphoton triggers at the level 2 and the level 3 does not have the prescale factors, thus all events which pass the trigger requirements are processed.

In level 2 trigger, the basic variables, which come from the result from the EM clustering in CEM are used to select the events which can be calculated by the hardware processor. The ratio of the total transverse energy and the EM energy must be near 1 to exclude the backgrounds from jets. Isolated EM clusters are required to reduce background by the neutral mesons from jets.

3.2.1 Level 1 Trigger Requirement

At the level 1 trigger we used in this analysis the events are required to have a 5 GeV energy deposition in the CEM towers.

3.2.2 Level 2 Trigger Requirement

Level 2 trigger for two photon event consists of 2 criteria; one is E_T and the other is isolation, which rejects the backgrounds and obtain a more signal-rich sample. This trigger first requires that events have 2 central EM clusters both of which have E_T above 10 GeV. The isolation cut in neural net chip is roughly equivalent of the isolation energy of 3×3 towers surrounding the trigger tower less than 5 GeV for both clusters.

At the level 2, the hardware trigger requires the event;

1. to have the 2 clusters in the detector region $|\eta| \leq 1.19$,
2. having the transverse energy $E_T \geq 10\,\mathrm{GeV}$,
3. the ratio of the total transverse energy and the electromagnetic energy should be near 1
   $E_{T,TOT} \,/\, E_{T,EM} \leq 1.125$,
4. the clusters are isolated in the calorimeter.

3.2.3 Level 3 Trigger Requirement

At level 3, the data are processed by the on-line software and calculated various sophisticated variables (3D tracks, z vertices, shower position at the CES, *etc.*) . We require

1. $E_{\mathrm{T}} \geq 10\,\mathrm{GeV}$ for both CEM clusters,
2. fiducial area in CES coordinate; $|x| \leq 17.5\,\mathrm{cm}$ and $14.5\,\mathrm{cm} \leq |z| \leq 217.0\,\mathrm{cm}$.

Figure 3.1 shows the E_T distributions of the leading and next-to-leading EM clusters in the two photon dataset. Since all combinations of the EM clusters in one event are booked, there are some events below the trigger threshold (they are not the triggered clusters) , but the number of events steeply rise at the threshold. Since the trigger has nothing to do with whether the cluster associates the tracks or not, the dataset includes the electrons as well as photons. There are peaks at $40 \leq E_T \leq 50\,\mathrm{GeV}$ which come from the electrons from Drell-Yan process. Figure 3.2 shows the mass distribution of the diphoton dataset, which also shows the peak from the contamination of the Drell-Yan process.

3.3 Offline Event Selection

In the offline event selection, basically we use the same variables given from the algorithm used in the level 3 trigger. In off-line analysis we apply to the events some correction routines for the detectors which has been estimated from the accumulated events during the whole run. All corrections are taken into account in the analysis then we make the criteria to have the two photon candidates.

3.3.1 Energy Correction and Transverse Energy Requirement

The correction is applied to each CEM response. Here we describe the transverse EM energy corrections we used in this analysis.

The transverse energy for electrons/photons in the CEM was corrected by 3 ways:

1. correction for response variations in the individual CEM tower,

2. correction for tower-to-tower gain variation,

3. correction for time dependent gain variation.

The correction factors for the difference of the response in each individual tower of the calorimeter are given from the CEM test beam with the electrons. Reference [29] describes the results from 50 GeV electron data.

The tower-to-tower gain correction is done with the CEM testbeam result. The CEM response is also corrected with the the inclusive electron dataset [35][36].

There are some factors which we need to apply the time-dependent correction. For example, CEM uses the photomultiplier tubes as a readout device, which detect the photons from scintillating tiles via a wave-shifting bar and the light guide, The gain for each phototube sometimes should be monitored as a function of the time during the collider run because of the fluctuations of their long-term-stability. The long-term-stability of the scintillating tiles, wave-shifting bars and the light guides is also taken into

account for degradation of the energy resolution and the energy scale. It is monitored during the runs then used in the correction routines at the off-line level if needed.

At the offline event selection, the events are required to have the corrected E_T to be:

$$E_T^{corrected} \geq 12\,\mathrm{GeV}\,, \tag{3.4}$$

for both EM clusters to reject the trigger bias for the E_T cut at the level 2 (where E_T is required to be larger than 10 GeV and the cluster to be isolated) .

3.3.2 Calorimeter Isolation Cut

A calorimeter isolation cut is one of the most effective criterion in the photon selection cuts. The dominant source of the backgrounds for this analysis is the neutral mesons decaying into multi photons with large transverse momentum which come from the quark/gluon fragmentation. Usually high p_T neutral mesons are the constituents of the "jets", thus larger amount of the underlying particles associate with them, compared with the prompt photon case. The calorimeter isolation cut therefore effectively rejects the background neutral hadrons from prompt photon events.

The calorimeter isolation is calculated as follows; first we make the cone around a EM cluster with a radius ΔR denoted by

$$\Delta R = \sqrt{\Delta\eta^2 + \Delta\phi^2}. \tag{3.5}$$

The cone radius of 0.4 or 0.7 are typically used in CDF physics analyses. Then the energy depositions for all towers within the radius are added, finally the energy of the EM cluster is subtracted,

$$\mathrm{Isolation} = \left(\sum_{i \leq \,\mathrm{cone\ size}} E_i \right) - E_{cluster}\,. \tag{3.6}$$

where E_i is a tower energy and $E_{cluster}$ is an energy of an EM cluster.

Figure 3.4 shows the isolation distributions in the cone of 0.4 , where the two photon events are selected with all selection cut described in this chapter except for the isolation cuts, and are applied the background subtraction method which is described in the next chapter, to extract the real two photon events and background events. In this figure R shows the fraction of the events within the isolation $\leq 1\,\mathrm{GeV}$. The real two photon events are almost within the isolation $\leq 1\,\mathrm{GeV}\,(R \sim 0.90)$, while the backgrounds are much broader than the signals $(R \sim 0.36$ for the total backgrounds$)$. Thus we chose the isolation cut

$$\text{isolation in cone } 0.4 \leq 1\,\mathrm{GeV} \tag{3.7}$$

to select the diphoton candidates.

3.3.3 Lateral Shower Profile: χ^2 and Extra Cluster Cut in the CES

The lateral shower profile in the CES is useful to discriminate the background decaying into multi photons. For example, photons from $\pi^0 \to \gamma\gamma$ deposits their energy into CEM, with the opening distance $d\,(\mathrm{cm})$ at a radius $R\,(\mathrm{cm})$ from the beam line. The opening distance is related to the P_T of π^0, which is:

$$d\,(\mathrm{cm}) = \frac{2RM_{\pi^0}}{P_T}\,, \tag{3.8}$$

where $M_{\pi^0} = 0.135\,\mathrm{GeV}/c^2$ is π^0 mass, P_T is in GeV/c, $R = 184\,\mathrm{cm}$ at the CES radius. It indicates that for the neutral mesons with high P_T (around $\geq 5\,\mathrm{GeV}$), the decaying multiple photons do not separate each other enough to be distinguished with the CEM tower configuration $(d \sim 10\,\mathrm{cm})$, in other words they are included in the same CEM cluster. The lateral shower profile of such an event shows us the different shower shape compared with that from the testbeam electrons. We use this difference to reject the backgrounds effectively.

The CES provides us the informations of the lateral profile of the EM shower and

its lateral position nearly at shower maximum region in the CEM. The CES clusters are found independently in both wire and strip view. First we look for the wire/strip channels which have the output of $\geq$ 0.5 GeV to be regarded as the seed channels. Then includes the 11 channels (with the threshold of 57.2 MeV) centered on the seed channel. We repeat this procedure for all seed channels. The CES cluster should associate with the corresponding EM cluster.

The configuration of the CES is described in the previous chapter. In CES coordinate, we regard the x and z position of the EM shower as the weighted mean of the cluster in each wire/strip view, which are labeled as X_{CES} and Z_{CES}, respectively. In order to use the CES clusters in its fiducial area, the geometrical cuts for the CES cluster are required to be

$$|X_{CES}| \leq 17.5\,\mathrm{cm}\,, \tag{3.9}$$

$$14\,\mathrm{cm} \leq |Z_{CES}| \leq 217\,\mathrm{cm}, \tag{3.10}$$

in the CES local coordinate.

Before reffering to the evaluation of the CES χ^2, we note that the shower shape of the test beam electrons is used as a standard EM shower profile for this analysis instead of that from the real photons. We should have the lateral shower profile for real photon as a standard shower profile. But we don't have the test beam result for real photons, and using the real photon beam is not realistic at the testbeam. We should depend the lateral shower shape on the test beam result for electrons. Essentially the difference between the shape of the photons and that for electrons is small, only the shower-starting point for the electron is slightly earlier than that for photons, according to the simulations. We include this difference into the systematic uncertainty for evaluating the two photon cross section, which will be discussed in the next chapter. The χ^2 is calculated by:

$$\chi^2 = \frac{1}{4}\sum_{i=1}^{11}\frac{(y_i - \bar{y}_i)^2}{\sigma_i^2}\,, \tag{3.11}$$

where i is the channel index, y_i is the profile of either wire or strip channel from the

collision data, which is the sum of the output energy from the wires/strips for the corresponding i-th channel (GeV for typically 2 wires/strips, normalized to unity) , and $\bar{y}_i$ is the standard electron profile, and σ_i^2 is the estimated variance of the standard profile $\bar{y}_i$. $\bar{y}_i$ is from the test beam result, which is defined by:

$$\bar{y}_i \;=\; \int_{x_i^{lower}}^{x_i^{upper}} f(x)\,dx \;=\; I(x_i^{upper}) \;-\; I(x_i^{lower})\,, \tag{3.12}$$

where x_i^{upper} and x_i^{lower} show the distance from the shower center in wire/strip view. As described above, typically $x_i^{upper} - x_i^{lower}$ corresponds to 2 wires/strips. The standard CES profile from testbeam electron, $f(x)$ and $I(x)$ is described in Appendix A in details, as well as the description of σ_i^2.

A variable χ^2_{CES} is defined as the mean value of χ^2_{wire} and χ^2_{strip}:

$$\chi^2_{CES} \;=\; \frac{\chi^2_{wire} \;+\; \chi^2_{strip}}{2}\,. \tag{3.13}$$

χ^2_{CES} of the real photon is almost within 20, while the χ^2 for the neutral mesons is broad. Thus it is effective to require:

$$\chi^2_{CES} \;\leq\; 20\,, \tag{3.14}$$

for the background reduction.

The variable χ^2_{CES} is also used in the background subtraction methods which will be described in the next chapter, where we calculate the efficiencies for the photons/backgrounds to have $\chi^2_{CES} \leq 4$ in the sample $\chi^2_{CES} \leq 20$.

If a CEM cluster has two CES clusters and they are placed close together, the EM cluster has a possibility to come from the background neutral meson: one of the decaying multiple photons would make the first CES cluster and the rest of the photons come together to make the second CES cluster. Thus a CES extra cluster cut is effective to reject the background neutral mesons. The event is required that they do not have the extra cluster above 1 GeV near the seed tower in both X and Z views in the CES

coordinate.

3.3.4 No-Track Requirement

Real photon does not have the electrical charge to make the signals in the CTC. As is seen in Fig. 3.2 and 3.3, it is essential to require that there is no 3-dimensional track associated with the EM clusters.

We use the hit rate in the CPR to extract the real two photon events instead of using CES if the E_T of the CEM cluster is greater than 35 GeV, which is described in details in the next chapter. CPR is only divided in four chambers in z-direction which means we do not know which particle make the CPR hit if two or more particle penetrate the same CPR module in R-Z plane. We require the events that there is no tracks pointing at the CPR hit position if the CEM cluster have the $E_T \geq 35\,\mathrm{GeV}$.

3.3.5 Z vertex and Rapidity Cut

At the event reconstruction level, we have information of $\bar{\mathrm{p}}\mathrm{p}$ collision point measured by the VTX along the beam line. Some criteria are applied to classify the vertices into 6 types. In this analysis we require the reconstructed vertices that at least one vertex should have the "best 2" rank and it should be within the area of,

$$|Zvertex| \leq 60\,\mathrm{cm}\,, \tag{3.15}$$

to confirm the event inside the fiducial region of the CDF detector.

Using the interaction point along the Z axis and the CES cluster position, the physics rapidity of a photon is calculated;

$$\begin{aligned} \eta_\gamma &= \frac{1}{2}\log\left(\frac{E + p_Z}{E - p_Z}\right) \\ &= \frac{1}{2}\log\left(\frac{\sqrt{R^2_{CES} + Z^2_{vertex} + X^2_{CES}} + Z_{vertex}}{\sqrt{R^2_{CES} + Z^2_{vertex} + X^2_{CES}} - Z_{vertex}}\right) \end{aligned} \tag{3.16}$$

item	events alive
diphoton trigger dataset	71206
associated 3d track	22844
$E_T \geq 12\,\mathrm{GeV}$	13228
$E_{cone4} \leq 1\,\mathrm{GeV}$	1452
$\lvert x\rvert$ and $\lvert z\rvert$ fiducial cuts	1299
extra strip / wire cluster	784
associated CPR track	779
$\chi^2_{CES} \leq 20$	776
$\lvert z_{vert}\rvert \leq 60\,\mathrm{cm}$	713
$\lvert\eta_\gamma\rvert \leq 0.9$	570
result from 1993-1995 collider run	570
result from 1992-1993 collider run	82
Total number of diphoton candidate	652

Table 3.1: Event cuts and the number of events for diphotons.

where R_{CES} is a radius of the CES cylinder, X_{CES} is the X position of the CES cluster in the CES coordinate and Z_{vertex} is the interaction point in the detector $R-Z$ view

It is required that the rapidity is,

$$|\eta_\gamma| \leq 0.9 \tag{3.17}$$

to compare the data with the NLO QCD prediction.

3.3.6 Final Diphoton Candidates

Table 3.1 shows the list of selection cuts and the number of events in the 1993 - 1995 collider run. The two photon dataset from 1992 - 1993 collider run is analyzed separately with the same offline selection cuts.

By combining the two collider experiments, total 652 events are alive as the two photon events.

3.4 Efficiencies for the Trigger and Selection Cuts

3.4.1 Level 2 Trigger Efficiency

The dielectron sample split from the inclusive electron sample was used to evaluate the level 2 trigger efficiency. The standard electron selection criteria are described in details in Appendix A. Following criteria were applied,

1. Both EM clusters in the central region,
2. extra energy in cone $0.4 \leq 1$ GeV,
3. standard photon fiducial cuts ,
4. $|Z_{vertex}| \leq 60$ cm ,
5. Number of 3D tracks $= 1$,
6. $\chi^2_{CES} \leq 20$,
7. $E/P \leq 1.5$,
8. $Had/EM \leq 0.05$,
9. $L_{sh} \leq 0.2$,
10. $|\eta_e| \leq 0.9$,
11. position difference between the CTC position extrapolated to the CES and the CES cluster position; $|\Delta x| \leq 1.5$ cm and $|\Delta z| \leq 2.5$ cm.

The data which passed the reconstruction processes should be required the trigger bit which we are interested in, because the events were accumulated with the "OR" of all physics triggers, whose triggering rate(we call it prescale factor) were usually different

from each other. Thus the level 2 dielectron trigger was required to the events to ensure that the events passed the dielectron trigger and to avoid the effect of prescale factors from other triggers.

Figure 3.5 shows the ratio of these two distributions which corresponds to the level 2 trigger efficiency as a function of E_T. It becomes flat in the region of $E_T \geq 12\,\mathrm{GeV}$.

We used the level 2 trigger efficiency

$$\epsilon(\text{cone } 0.4 \leq 1\,\mathrm{GeV}) = 0.84 \pm 0.02\,. \tag{3.18}$$

This was used to correct the diphoton cross section for the inefficiency of the level 2 trigger.

3.4.2 Calorimeter Isolation Cut Efficiency

Calorimeter isolation cut efficiency is evaluated by the minimum bias (MB) dataset. First of all, we generate the two sets of the random numbers for the rapidity and the azimuthal angle $(\eta_1\ \phi_1)\,(\eta_2\ \phi_2)$ in each MB event. We assume as if there are two photons placed at these points. Then we calculate the calorimeter isolation with Eq. 3.6 around these points. Figure 3.6 shows the comparison of the Cone 0.4 isolation distribution of two photon events with that from the MB events, The plots are well consistent with each other, which shows that we can estimate the isolation cut efficiency with the MB events instead of two photon events.

Figure 3.7 shows Cone4 $\leq 1\,\mathrm{GeV}$ isolation cut efficiency as a function of the instantaneous luminosity. All points are laid on the straight line. A typical number of the efficiency $(\text{at } 9.1 \times 10^{30}\,\mathrm{cm^{-2}\,sec^{-1}})$ is 0.895 ± 0.005 per photon.

3.4.3 CES Extra Cluster Cut Efficiency

Most of the CEM cluster of the real photon do not have the CES extra clusters, but the CEM cluster with high E_T would have the possibility to have them because

they have large electromagnetic energy depositions at the shower maximum position, the CES cluster would be large enough to be rejected by the cut. Shower fluctuation should be also taken into account.

The CES extra cluster cut efficiency is estimated using the test beam electron data. Figure 3.8 shows the efficiency as a function of the electron energy. The efficiency shows lower as the energy of the electron goes higher, this symptoms are understood by the description above. The efficiency for the electrons from W decay is also shown which have a lower efficiency than the extrapolation from the test beam electrons due to the radiation of an extra photon.

3.4.4 Track Cut Efficiency

The requirement of the no-tracks pointing at the CEM cluster rejects the real photon event in two cases; one is the conversion photons in front of the tracking chamber, where one of the conversion electrons has the almost of the momentum of the photon then coming into the CEM. In this case, CEM cluster with the high P_T 3D track appears to the event which does not filled with the track cut.

The track cut efficiency for the conversion photon is evaluated with the conversion electron sample. The analysis was done in the inclusive photon cross section measurement at CDF [15][37]. It was 0.94 with a 0.4% uncertainty.

The track cut rejects the events in the case that the CEM cluster comes from the real photon but the tracks from the underlying events accidentally points it.

The efficiency is estimated with the min bias events where the virtual CEM clusters are randomly generated, looking at the tracks which points at the virtual clusters. The result was 0.94 with a 1% uncertainty.

3.4.5 Summary of Efficiencies

Table 3.2 lists the numbers for efficiencies used in this analysis, which includes the rest of the efficiencies which are not described in details in this section.

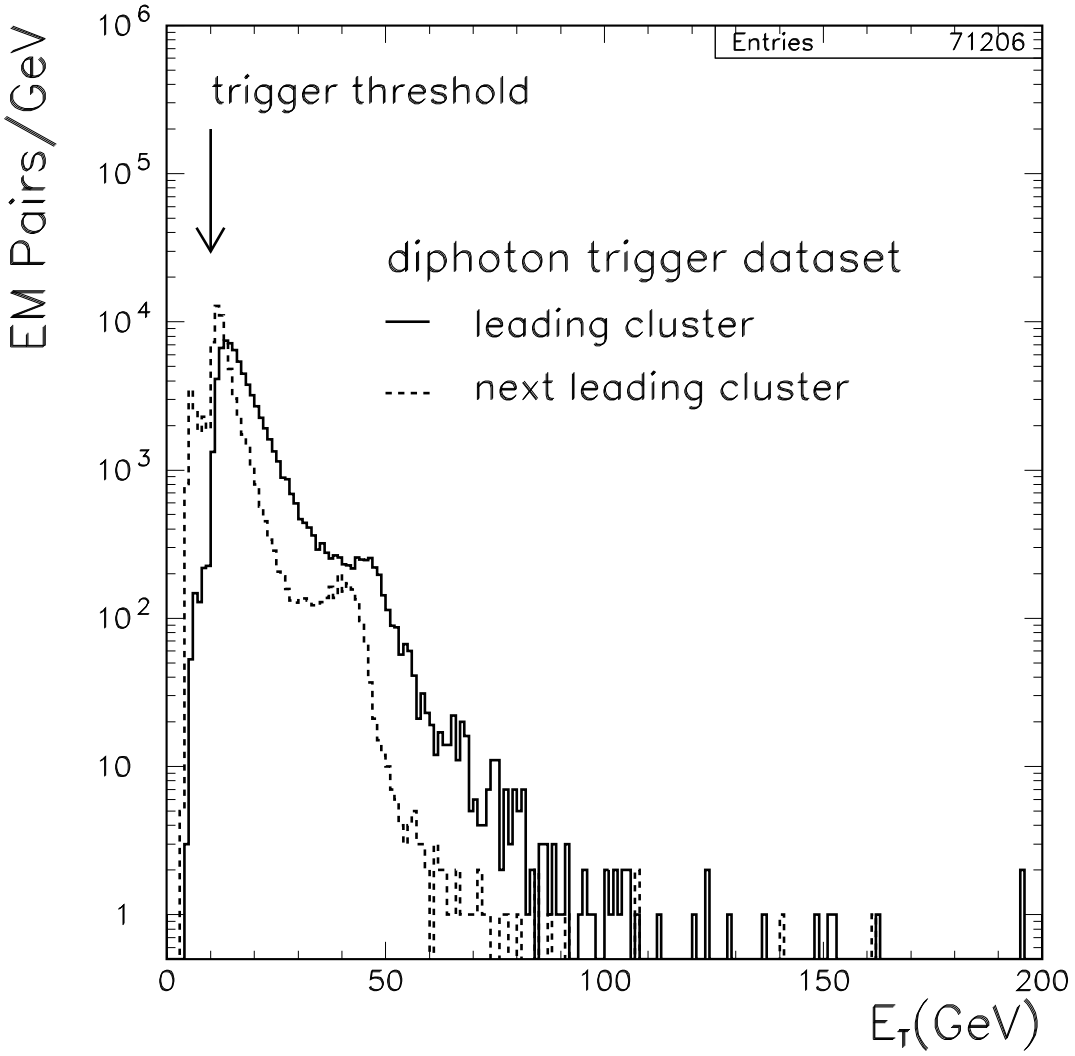

Figure 3.1: E_T distribution of the leading and next-leading EM clusters in the two photon dataset.

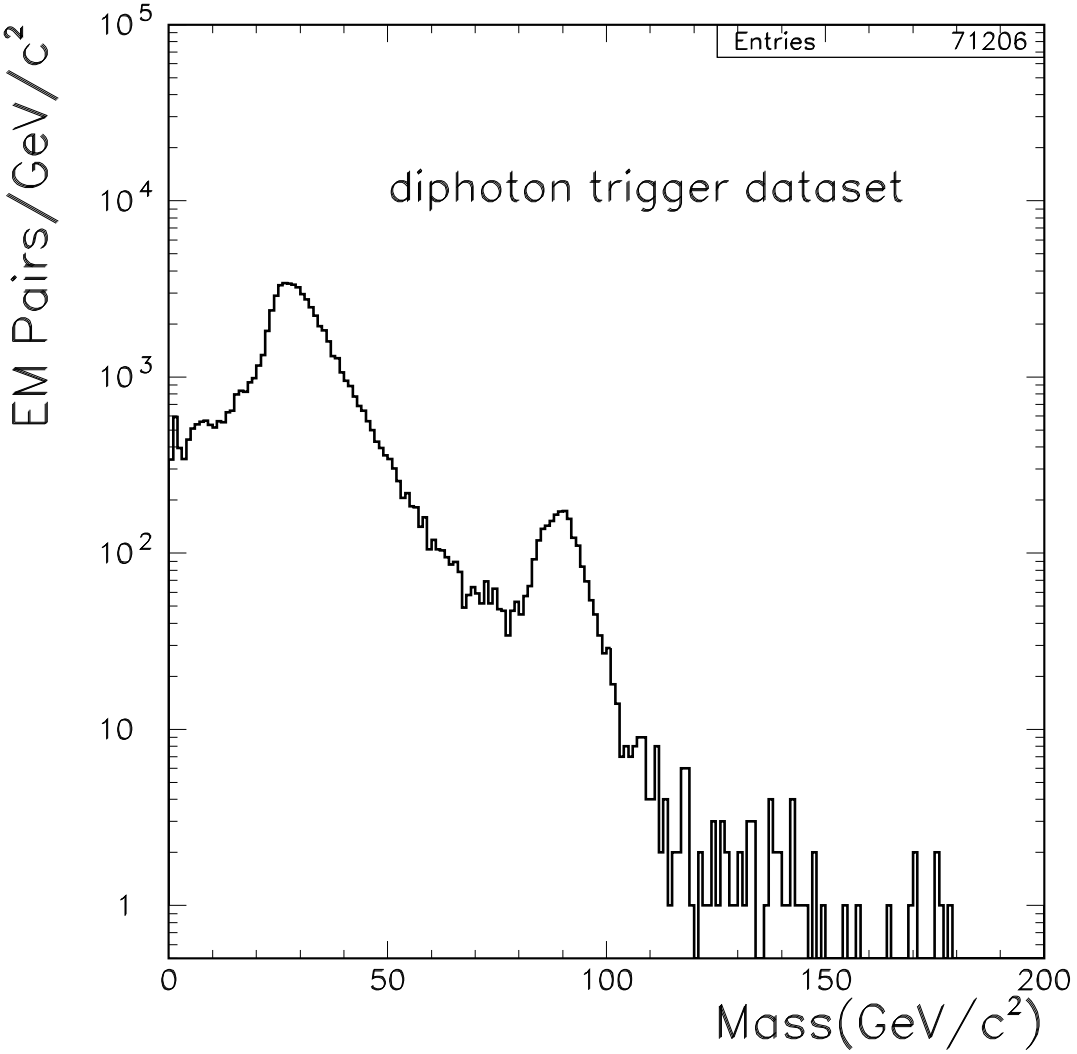

Figure 3.2: Invariant mass distribution of the two EM clusters in the two photon dataset.

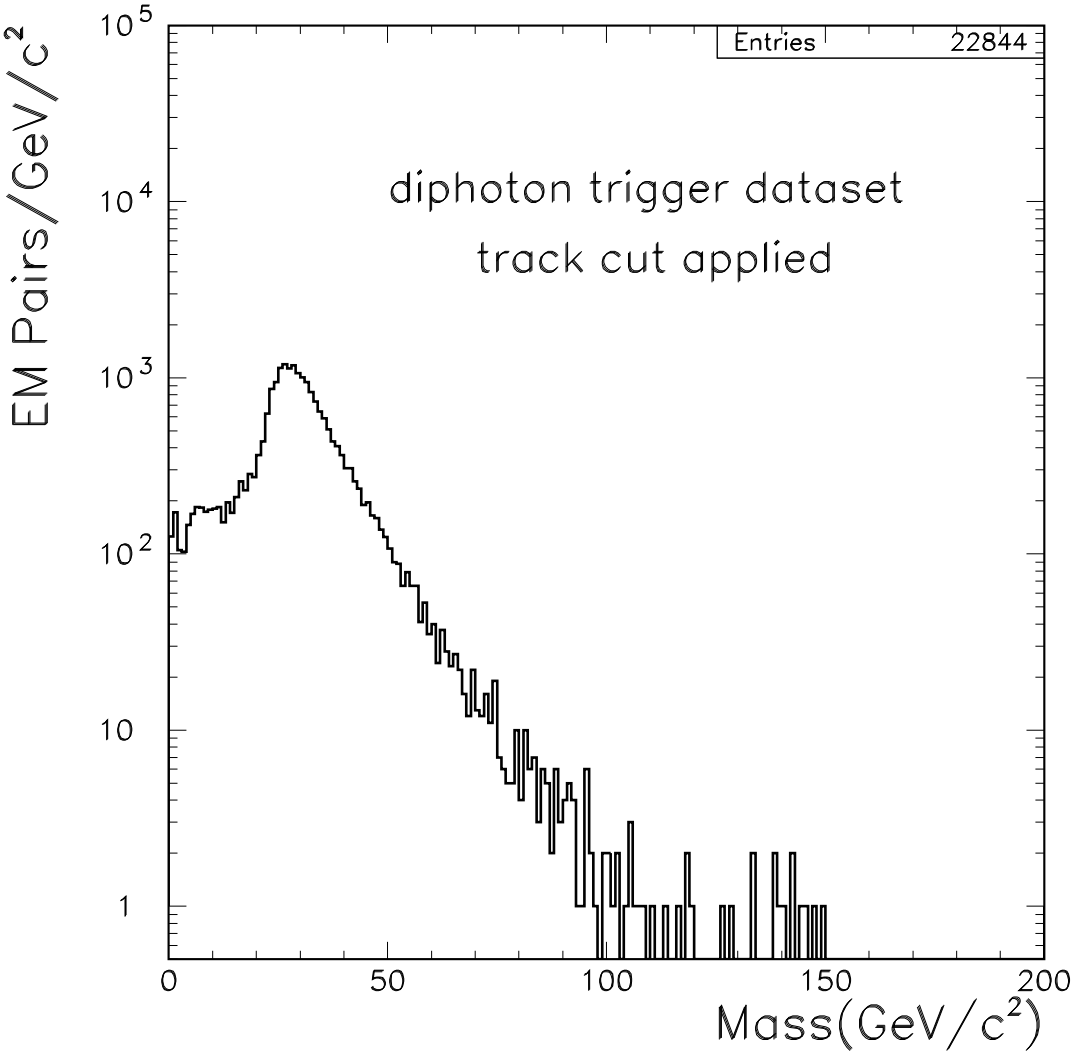

Figure 3.3: Invariant mass distribution of the two EM clusters in the two photon dataset, with the requirement of the number of 3D tracks to be zero.

ITEM	VALUE
CES fiducial cuts $\epsilon_{\rm fid}$ (per photon)	0.663
conversion veto $\epsilon_{\rm conv}$ (per photon)	0.94
underlying track $\epsilon_{\rm trk}$ (per photon)	0.94
isolation cut $\epsilon_{\rm iso}$ (per photon)	0.9 luminosity dependent
Zvertex cut $\epsilon_{\rm zvret}$ (per event)	0.97
extra CES cluster cut $\epsilon_{\rm ext}$ (per photon)	$>$0.9 E_T dependent
trigger efficiency $\epsilon_{\rm L2}$ (per event)	0.8

Table 3.2: Summary of efficiencies.

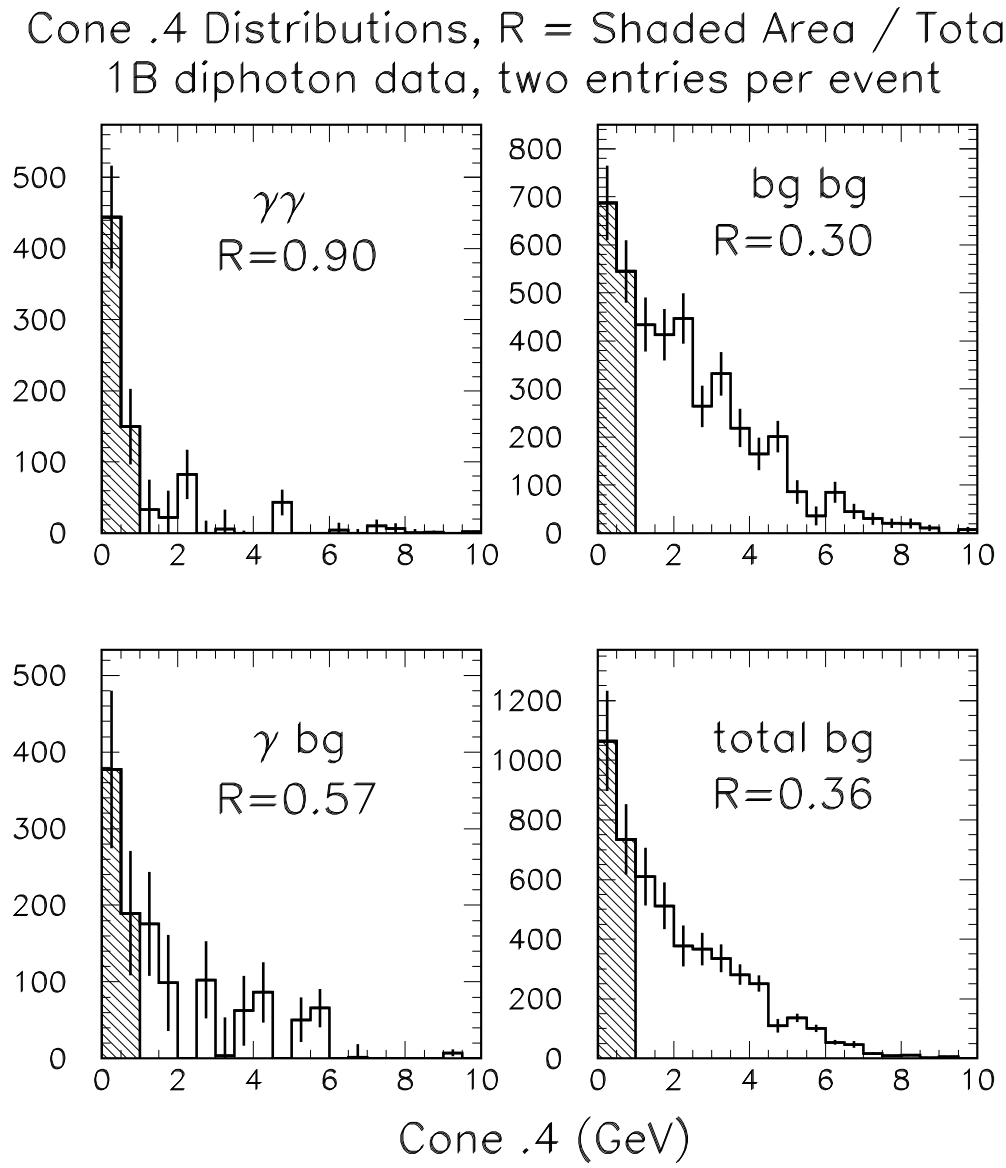

Figure 3.4: Distributions of the transverse energy isolation in the cone of 0.4 for (a) $\gamma\gamma$events, (b) γ background events, (c) background background events and (d) total (b+c) backgrounds. R shows the ratio of the number of events in the shaded area and the number of the total events.

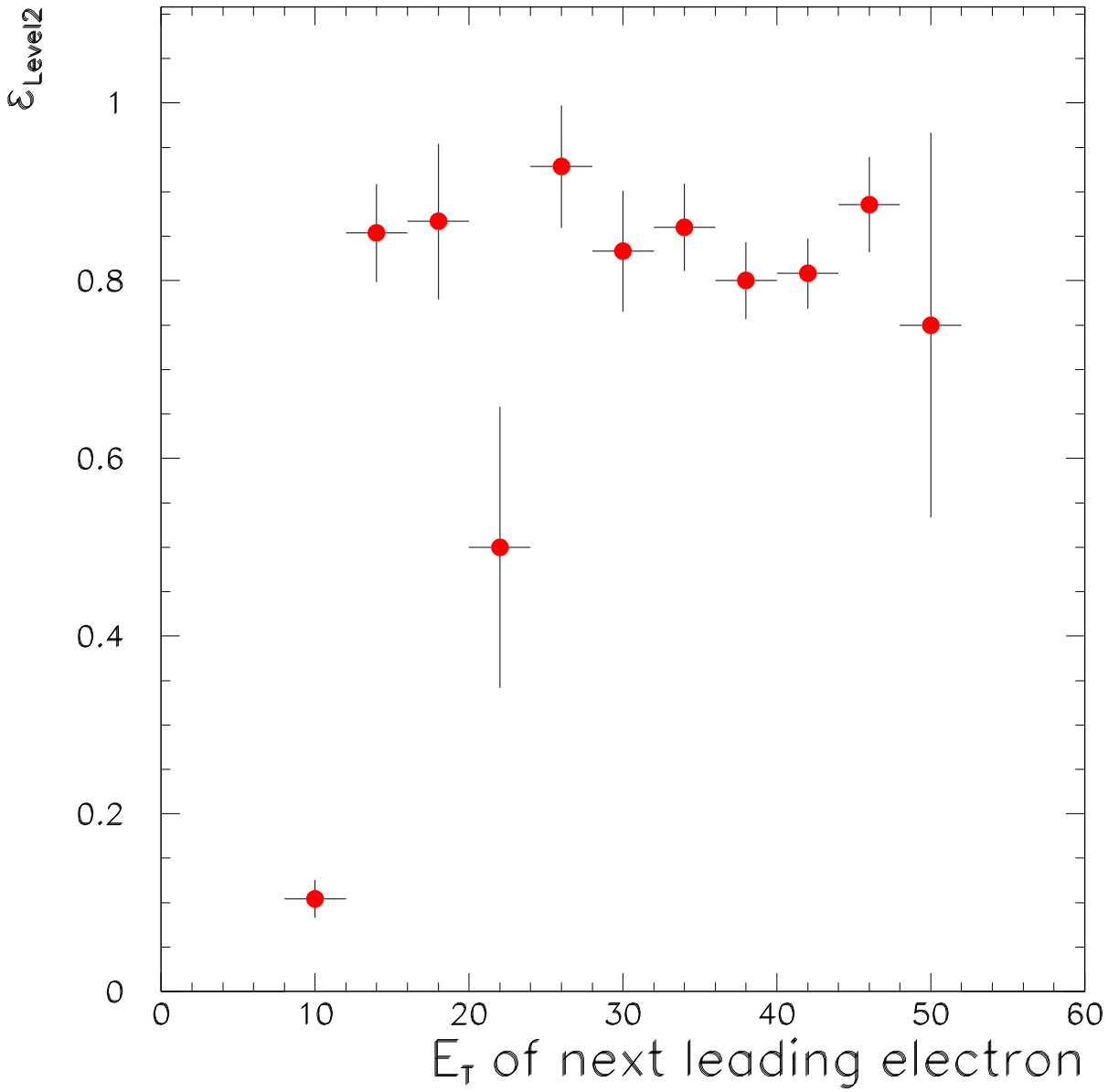

Figure 3.5: Level 2 trigger efficiency as a function of E_T for next-leading electrons.

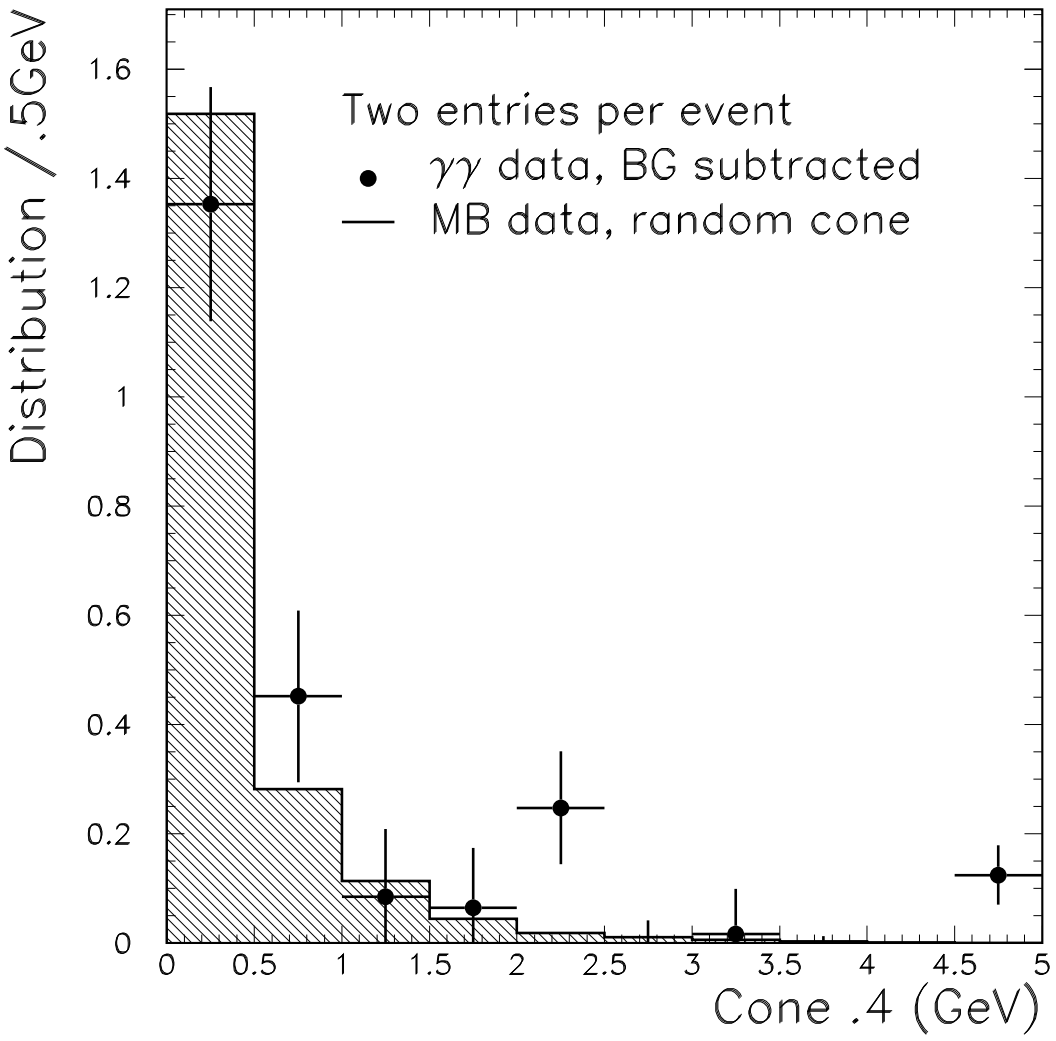

Figure 3.6: Comparison of the cone 0.4 isolation distributions between the two photon events (points) and the that from MB events (histogram). Both points and histogram are two entries per event.

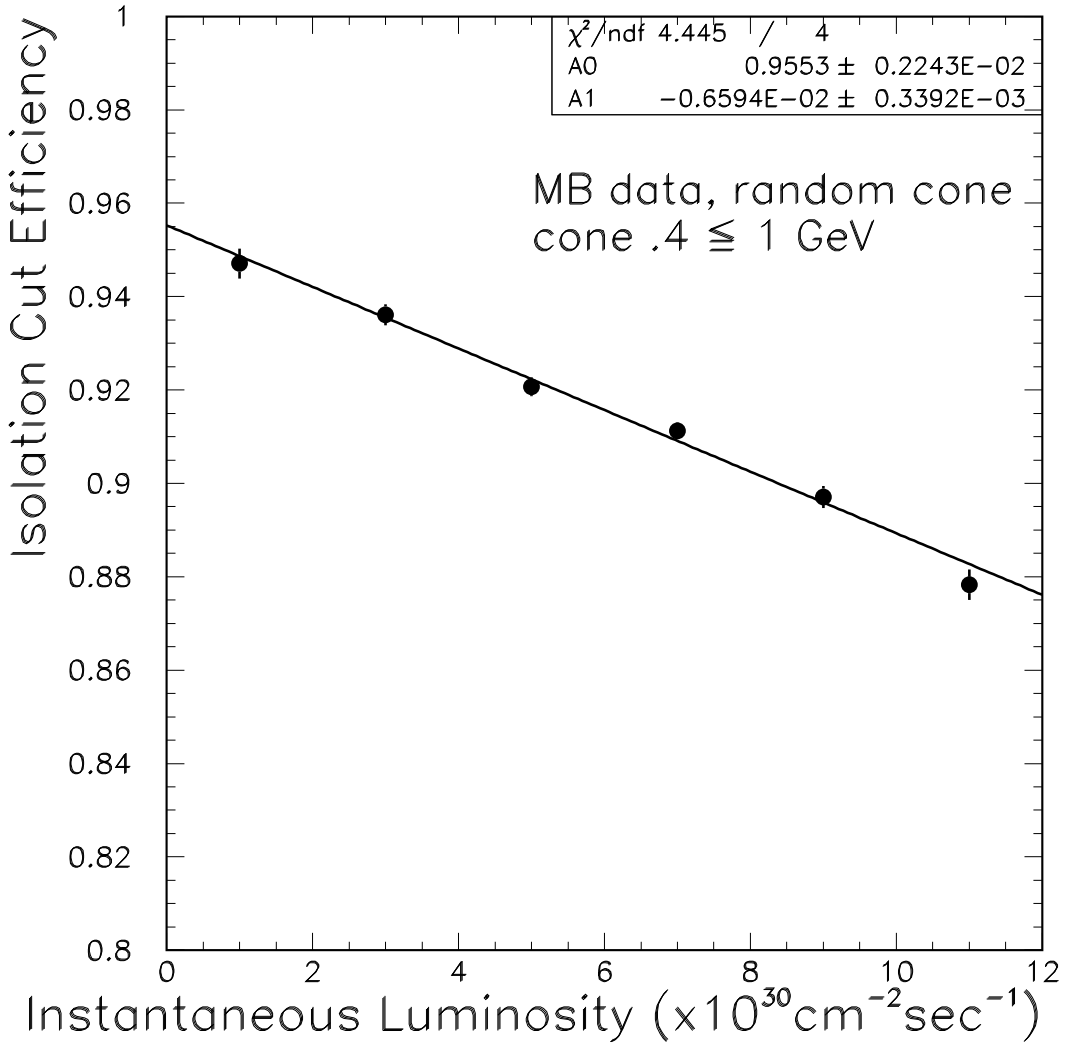

Figure 3.7: Efficiency of the isolation cut (cone4$\leq$1 GeV) as a function of the instantaneous luminosity.

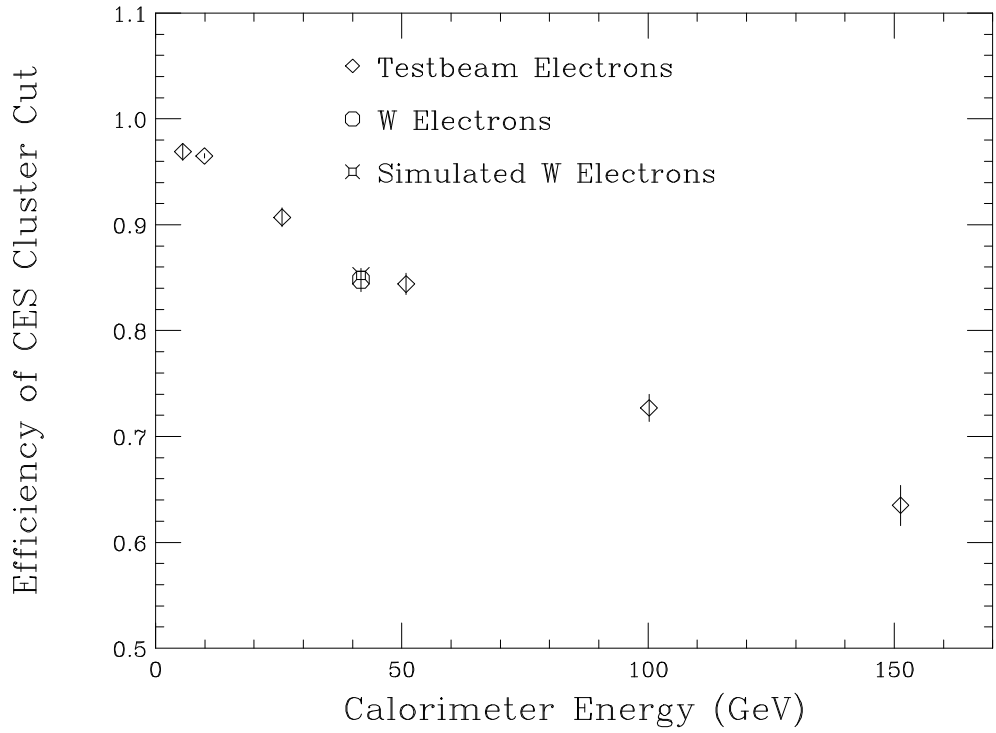

Figure 3.8: Efficiency of the CES extra cluster cut as a function of the calorimeter energy.

Chapter 4

Photon Identification

In this chapter we describe the photon identification procedure and the background subtraction in the diphoton sample selected in the previous chapter.

4.1 Background Sources

In the previous chapter we described the selection criteria of the diphoton candidates. All criteria give us high efficiencies for real two photon events and have rejection powers for the backgrounds. After the selection cuts, we have the candidates for two photon events, but we still have backgrounds in the candidates, which we are unable to reject by the selection cuts event-by-event, because multi photons from the neutral meson cannot identify as more than 2 CES clusters if p_T of the meson is high enough for the photons to have their p_T almost the same direction.

Table 4.1 shows the list of the neutral mesons as a background source in this analysis and their measured branching ratio of their decays to photons or π^0's [39].

4.2 Photon Identification Method

4.2.1 Profile and Conversion Method

The CES shows us a statistical difference between a real photon and multi photons from neutral mesons. The comparison of the lateral shower profile in the shower maximum region measured in the CES with that from the electron test beam result give us a statistical difference between a real photon and multi photons from neutral mesons. We express the difference with a variable χ^2_{CES} defined by Eq.3.13. Figure 4.1 shows the comparison of the χ^2 distributions of the real photons and neutral pions generated by the simulations.

We look at the EM shower profile for the incident particle comparing with that from real electrons from the testbeam. If the background particle has relatively low $P_T\,(\leq 40\,\mathrm{GeV})$, the shower shape is degraded by the multiple photons having the distance calculated by Eq. 3.8, which makes χ^2 higher, while at higher $P_T\,(\geq 40\,\mathrm{GeV})$, the distance between the photons becomes smaller enough to makes χ^2 lower. As the result, at high p_T it makes this method difficult to distinguish this background event from the real photon event. We will see the limitation of the separation power of this method later.

Another statistical information is the difference of the hit rate in the CPR as a result from the difference of the photon conversion probability in front of the calorimeter between the photons and background mesons. In high p_T, multi photons from the neutral meson decays are almost in the same direction, then they come into the same module of the CPR. The hit rate in the CPR is correlated with the number of photons coming

Decay modes	Branching ratio (%)
$\pi^0 \to \gamma\gamma$	98.798 ± 0.032
$\eta \to \gamma\gamma$	39.25 ± 0.31
$\eta \to \pi^0\pi^0\pi^0$	32.1 ± 0.4
$K^0_s \to \pi^0\pi^0$	31.39 ± 0.28

Table 4.1: List of the neutral background sources.

into the same module. Consider a meson $\pi^0 \to \gamma\gamma$ as a background, for example, the conversion probability of the π^0 (P_π) and that of single photon (P_γ) is related to:

$$\begin{aligned} P_\pi &\approx P_\gamma^2 + 2P_\gamma(1 - P_\gamma) \\ &= 1 - (1 - P_\gamma)^2 \end{aligned} \tag{4.1}$$

where we assume that the conversion probability of the photon is approximately independent of p_T. Thus the difference of the conversion probability between single photons and π^0's can be used to extract the real two photon events from the two photon candidates.

As we described above, this method is independent of the incident particle p_T, while the separation power is smaller than that of the profile method. We used this method in higher p_T region, where the profile method becomes having smaller separation power. It will be described later.

Now we define the efficiencies for passing a certain criterion with the simulated photons and the backgrounds. The criterion is that the photon or background events have the $\chi^2 \leq 4$ (CPR charge $\geq$ 500 fC) in the profile (conversion) method. Then we define that N_{pass} (N_{false}) shows the number of EM clusters that pass (fail) the criterion, and the efficiencies of the tests ($\chi^2 \leq 4$ in profile method and CPR charge $\geq$ 500 fC in conversion method) for both photons and backgrounds are calculated by:

$$\epsilon_\gamma = \mathrm{N}_{pass,\gamma} \,/\, \mathrm{N}_{total,\gamma} \tag{4.2}$$

$$\epsilon_b = \mathrm{N}_{pass,b} \,/\, \mathrm{N}_{total,b}. \tag{4.3}$$

We obtained them from the simulation, and these are calibrated with the real photon and neutral meson samples which will be described in the next section.

Once we have the efficiencies, we can calculate the real number of photon events and background events. In the single photon case, the following vector equation can be used

to obtain the number of true photons and the backgrounds:

$$\begin{pmatrix} N_{false} \\ N_{pass} \end{pmatrix} = \begin{pmatrix} 1 - \epsilon_b & 1 - \epsilon_\gamma \\ \epsilon_b & \epsilon_\gamma \end{pmatrix} \begin{pmatrix} N_b \\ N_\gamma \end{pmatrix} \tag{4.4}$$

where $N_\gamma\,(N_b)$ is the number of true photons (backgrounds) in the photon candidates. In the two photon case, there are 4 possible combinations in CES/CPR test, which are false-false, false-pass, pass-false and pass-pass, then the the number of possible cases for the combinations of signal and background become 4, which are $b-b$, $b-\gamma$, $\gamma-b$ and $\gamma-\gamma$. We used the following vector equation with 4×4 matrix instead of 2×2, as was used in the single photon case.

$$\begin{pmatrix} N_{ff} \\ N_{fp} \\ N_{pf} \\ N_{pp} \end{pmatrix} = \begin{pmatrix} (1-\epsilon_{b1})(1-\epsilon_{b2}) & (1-\epsilon_{b1})(1-\epsilon_{\gamma 2}) & (1-\epsilon_{\gamma 1})(1-\epsilon_{b2}) & (1-\epsilon_{\gamma 1})(1-\epsilon_{\gamma 2}) \\ (1-\epsilon_{b1})\,\epsilon_{b2} & (1-\epsilon_{b1})\,\epsilon_{\gamma 2} & (1-\epsilon_{\gamma 1})\,\epsilon_{b2} & (1-\epsilon_{\gamma 1})\,\epsilon_{\gamma 2} \\ \epsilon_{b1}\,(1-\epsilon_{b2}) & \epsilon_{b1}\,(1-\epsilon_{\gamma 2}) & \epsilon_{\gamma 1}\,(1-\epsilon_{b2}) & \epsilon_{\gamma 1}\,(1-\epsilon_{\gamma 2}) \\ \epsilon_{b1}\,\epsilon_{b2} & \epsilon_{b1}\,\epsilon_{\gamma 2} & \epsilon_{\gamma 1}\,\epsilon_{b2} & \epsilon_{\gamma 1}\,\epsilon_{\gamma 2} \end{pmatrix} \times \begin{pmatrix} N_{bb} \\ N_{b\gamma} \\ N_{\gamma b} \\ N_{\gamma\gamma} \end{pmatrix} \tag{4.5}$$

By inverting this 4×4 matrix, the real number of signals $(N_{\gamma\gamma})$ and backgrounds $(N_{b\gamma}$, $N_{\gamma b}$ and $N_{bb})$ are evaluated.

4.2.2 Photon Identification on Event by Event Basis

As is seen in the next section, the CES profile efficiencies have a large dependence on photon p_T. The CPR conversion efficiencies also have a dependence on the amount of the material in front of the CPR, which mainly caused by the detector configuration. In other words, the change of the amount of the material is also interpreted to an angle of the incident particle into the central detector. Thus the profile and conversion efficiencies are changed event by event. Actually it is natural to use the method described above on event by event basis, in which we can take these dependences into account on the photon identification.

For example, consider that we have a two photon candidate in which both of EM clusters pass the $\chi^2 < 4$ test, it means we have a input 4-dimensional vector in the Eq. (4.5): $(n_{ff}, n_{fp}, n_{pf}, n_{pp}) = (0, 0, 0, 1)$. Then by inverting the 4×4 matrix given by the CES / CPR efficiencies, we have the output 4-dimensional vector which contains the each weight in this event $(w_{bb}, w_{b\gamma}, w_{\gamma b}, w_{\gamma\gamma})$.

The procedure is repeated to all two photon candidates. The total number of the signal and background events are calculated by taking the sum of these signal/background weights:

$$N_{\gamma\gamma} = \sum_{i=1}^{n} w_{\gamma\gamma}^{(i)}, \tag{4.6}$$

$$N_{\gamma b} = \sum_{i=1}^{n} w_{\gamma b}^{(i)}, \tag{4.7}$$

$$N_{b\gamma} = \sum_{i=1}^{n} w_{b\gamma}^{(i)}, \tag{4.8}$$

$$N_{bb} = \sum_{i=1}^{n} w_{bb}^{(i)}, \tag{4.9}$$

where n is the number of total two photon candidates. The statistical errors for the

real $\gamma\gamma$, γb, $b\gamma$ and bb events are now defined by

$$\sigma_{\gamma\gamma} = \sqrt{\sum_{i=1}^{n} w_{\gamma\gamma}^{(i)\,2}}. \tag{4.10}$$

$$\sigma_{\gamma b} = \sqrt{\sum_{i=1}^{n} w_{\gamma b}^{(i)\,2}}. \tag{4.11}$$

$$\sigma_{b\gamma} = \sqrt{\sum_{i=1}^{n} w_{b\gamma}^{(i)\,2}}. \tag{4.12}$$

$$\sigma_{bb} = \sqrt{\sum_{i=1}^{n} w_{bb}^{(i)\,2}}. \tag{4.13}$$

4.3 CES Profile Method Efficiencies and Systematic Uncertainties

The CES χ^2 efficiencies are estimated with the simulated photons and backgrounds with GEANT. We need to confirm the consistency between the simulated efficiencies and those from real CDF data.

4.3.1 CES signal efficiency

Electrons for W decays are used to test the shape of the χ^2 distributions for simulated electrons from W decays. Figure 4.2 shows the comparisons of the χ^2 distributions in both the strip and the wire view and the average of those between the real W electrons and the simulated electrons. Simulation result show in agreements with the data.

The simulation was also checked by using the well separated real two photons from reconstructed η mesons decaying to two photons (with the branching ratio of 39%) in the CDF data. Figure 4.3 shows the invariant mass distribution of the two photons. A peak is observed at $0.546 \pm 0.005\,\mathrm{GeV}/c^2$ which corresponds to the expected mass of η meson $0.54745 \pm 0.00019\,\mathrm{GeV}/c^2$ [39]. π^0 mass peak is not obvious because the 11 channel

clustering in the CES is too wide for the π^0 peak. Figure 4.4 shows the comparison of the strip view of the χ^2 distribution of the photons from η decays in the CDF with the simulated η decays, which shows in agreement with each other.

4.3.2 CES background efficiency

In order to evaluate the CES efficiency for total backgrounds, we measured the production ratio between neutral mesons, especially the ratio of η meson and π^0 meson because these mesons are the dominant backgrounds for the photon analysis. In CDF measurement, we expect to have the number of π^0 and η mesons decaying to two photons

$$N_{\pi^0}^{detect} = N_{\pi^0}^{prod}\,\mathrm{BR}(\pi^0 \to \gamma\gamma)\,\epsilon(\pi^0 \to \gamma\gamma)\,, \tag{4.14}$$

$$N_{\eta}^{detect} = N_{\eta}^{prod}\,\mathrm{BR}(\eta \to \gamma\gamma)\,\epsilon(\eta \to \gamma\gamma)\,, \tag{4.15}$$

where $N_{\pi^0}^{detect}\,(N_{\eta}^{detect})$ is the number of $\pi^0(\eta)$ events decaying to two photons detected by the CDF detector, $N_{\pi^0}^{prod}\,(N_{\eta}^{prod})$ is the number of total $\pi^0(\eta)$ events produced in this collider run, $\mathrm{BR}(\pi^0 \to \gamma\gamma)$ $(\mathrm{BR}(\eta \to \gamma\gamma))$ is the branching ratio of the $\pi^0(\eta)$ decaying to two photons [39], and $\epsilon(\pi^0 \to \gamma\gamma)$ $(\epsilon(\eta \to \gamma\gamma))$ is the total acceptance for the detection of the $\pi^0(\eta) \to \gamma\gamma$. The branching ratios are already known, the detection acceptance are calculated by the detector simulation, the only unknown parameters are $N_{\pi^0}^{prod}$ and N_{η}^{prod}. Taking a ratio of these two numbers enables us to cancel out the systematic uncertainties.

Figure 4.5 shows the branching ratio times detection acceptance for each background source as a function of p_T, where the branching ratio for each background source is listed in Table 4.1 and the detection acceptance is estimated using the detector simulation. This plot shows that π^0 is the dominant sources for the CES background efficiency, by taking the η/π^0 ratio (1.02) and K_s^0/π^0 ratio (0.4) into account, which are described below.

• N_η / N_{π^0}

The background components for this method is investigated by the real π^0 and η sample collected in the CDF data. Figure 4.6 shows the mass distribution with the 3 channel CES clustering. Also shown is the background fit (2 Gaussian + polynominal) ,and the estimated distribution of single photons misidentified as π^0's. π^0 and η peaks are clearly seen. The resulting η/π^0 ratio is:

$$\frac{N_\eta^{prod}}{N_{\pi^0}^{prod}} = 1.02 \pm 0.15(\text{stat}) \pm 0.23(\text{syst.}) . \tag{4.16}$$

It is used to form the combined background χ^2 distribution.

• $N_{K_s^0} / N_{\pi^0}$

The process $K_s^0 \to \pi^0\pi^0$ also contributes the background χ^2 distributions, especially at high P_T region. The production of K_s^0 was measured by the CDF during 1987 collider run, using the charged decay modes [42]. The result of the ratio:

$$\frac{N_{K_s^0}^{prod}}{N_{\pi^0}^{prod}} = 0.4 \pm 0.05 , \tag{4.17}$$

is used in this analysis.

• Final Background Efficiency

Using Eq. 4.16, 4.17 and figure 4.5 for background efficiency, the final plot of CES $\chi^2_{CES} \leq 4$ cut efficiencies for both photons and backgrounds is calculated. It is shown in figure 4.9 with the bounds of the total systematic uncertainties described in the next section.

• Check of the Background Efficiency with the decay $\rho^{\pm} \to \pi^{\pm}\pi^{0}$

The background efficiencies from the simulation with the production ratio described above taken into account is cross-checked with the π^0s from $\rho \to \pi^0\pi^{\pm}$. Figure 4.7 is the invariant mass distribution of the photon candidate plus charged track. The peak is observed at $0.772 \pm 0.009\,\mathrm{GeV}/c^2$ which corresponds clearly to the ρ mass region and $0.7681 \pm 0.009\,\mathrm{GeV}/c^2$ from world average [39].

Figure 4.8 shows the χ^2_{CES} distribution of the π^0 from ρ decay. The result from the simulation is in good agreement with that from the CDF data.

4.3.3 Sources of the Systematic Uncertainties for CES Efficiencies

The systematic uncertainties of both signal and background are highly correlated, because these efficiencies are both sensitive to the same instrumental effects. Therefore they are not discussed separately; a one standard deviation change upward in the photon efficiency due to a given source results in a corresponding 1σ upward change in the background efficiency.

The sources of the systematic uncertainties for CES efficiencies are:

1. the difference of the shower fluctuation between electrons and photons,
2. the difference of the shower shape between electrons and photons,
3. the use of test beam showers taken under slightly different conditions than the collider running,
4. the background composition.

The uncertainty of the difference of the shower fluctuation between electrons and photons comes from the variation of the shower parametrization which are used in the detector simulation. This variation was used to estimate the systematic uncertainty of the shower fluctuation.

The shower shape of the photons is slightly different from that of the electrons because photon showers start later than electrons. In order to estimate the effect of the difference, we used electron testbeam result with different material in front of the calorimeter to see the change of CES χ^2 as a function of the shower depth of the strip chamber.

In the collider running, the high voltage to the chambers is slightly different from that in the testbeam. Thus the condition of the chamber, such as the saturation in the chamber was taken into account to estimate the systematic uncertainty of the CES background subtraction.

We changed the background composition N_η/N_{π^0} from 0.75 to 1.3 to estimate the systematic uncertainty.

The effects on the systematic uncertainty from these sources are plotted in figure 4.10. It shows the systematic uncertainties of the cross section due to the background subtraction uncertainties as a function of photon P_T, where the total uncertainty and the uncertainties for each source are plotted. For simplicity, only the positive uncertainties are shown. The negative uncertainties are the same fashions.

4.3.4 Constraint on the CES Systematic Uncertainties with CPR

If one assumes that the CES and CPR background subtraction methods work completely well and the systematic uncertainties of CPR are completely known, the CES systematic uncertainties can be constrained by looking at the relative difference of the number of photons from CES and CPR:

$$\frac{N_\gamma^{CES} - N_\gamma^{CPR}}{N_\gamma^{CPR}} = \frac{N_\gamma^{CES}}{N_\gamma^{CPR}} - 1\,. \tag{4.18}$$

Figure 4.11 shows the ratio of the number of photon events with CES profile method and that with CPR conversion method. Since the systematic uncertainty of the CPR,

as is seen in the next section, is reasonably smaller than that of CES, this difference, at most 10% , can be regarded as a systematic uncertainty of the CES.

4.4 CPR Conversion Method Efficiencies and Systematic Uncertainties

CPR conversion method is the independent scheme from the CES profile method to extract the real photon events from the photon candidates. The conversion efficiencies are calculated by the γ / backgrounds simulations, and need to be calibrated with the real collision data. In this section we describe the calculation and calibration of these efficiencies.

4.4.1 CPR signal and background efficiencies

For the CPR conversion method, ϵ_γ and ϵ_b are estimated with the simulated photons and backgrounds from the following equation:

$$\epsilon_\gamma \;=\; 1 \;-\; \exp\left(\, -7/9 \;\times\; \mathrm{t} \,\right) \tag{4.19}$$

$$\epsilon_b \;=\; 1 \;-\; \exp\left(\, -7/9 \;\times\; \mathrm{t} \;\times\; N_\gamma(P_T) \,\right) \tag{4.20}$$

where t is the amount of the material in front of the CPR as a radiation length, $N_\gamma(P_T)$ is the function of the average number of photons within the CPR "window". This changes with the particle type and its P_T. The effect of the particle type is estimated with the simulated π^0, η and K^0_s with a relative production ratio of 1:1.02:0.4.

These efficiencies should be corrected for the following effects. First the efficiencies are changed as a function of the polar angle θ of the particle, because the the total material for the particle penetrating should be changed. We correct the effect event by event basis. Next the effect of the backscattered photons and electrons inside the

calorimeter is estimated. These particles are produced during the electromagnetic shower after penetrating the CPR, their momentum are soft then they scattered inside the CEM with the large scattered angle, then give the signals in the CPR. This correction is estimated with the electromagnetic shower simulation. The last correction, which is applied only to ϵ_γ, is for the effect of the soft photons in the underlying event. It is estimated with the minimum bias triggers.

4.4.2 Calibration for the CPR Efficiencies with the Reconstructed Neutral Mesons

The CPR hit rate measured by the fully reconstructed neutral mesons (π^0, η and ρ) can be used to check the CPR hit rate estimated from the simulation. Since the CPR was installed to the CDF in 1992, the dataset which was used to calibrate the CPR is different from that used for CES calibration. The data used in this calibration was taken during the 1992-1993 collider run. Figure 4.12 shows the two γ invariant mass distribution of the π^0 and η mesons, and two γ plus charged track mass distribution of the ρ meson, with the transverse energy of the leading photons larger than 8 GeV. We calculated CPR hit rate with these reconstructed neutral mesons by looking at the hit rate of the event in the peak region (signal plus backgrounds) and that from the sidebands(backgrounds) . The expected CPR hit rate is also calculated with the simulation. These are described in details in [40][41]. The measured (expected) conversion rate is .842 $\pm$ .008 (.847) for the π^0 , .831 $\pm$ .01 (.842) for the η, and .836 $\pm$ .010 (.834) for the π^0 from ρ meson decay. All measured results and predicted results taking the corresponding detector materials into account show in good agreement with each other.

4.5 Sources of the Systematic Uncertainties for CPR Efficiencies

The uncertainty in the expected CPR conversion rate, due to the material count for the solenoid magnet, is 0.006. There is excellent agreement between the measured and predicted rates in all cases, thus we will use 0.006 for the uncertainty in ϵ_b. This translates into a 0.0078 uncertainty in ϵ_γ, and is completely correlated with the ϵ_b uncertainty.

The the final result of the both CES and CPR efficiencies are shown in figure 4.13.

4.6 Photon Identification Method Combined with CES and CPR Efficiencies

As is seen in the previous sections, the CES profile method has a large power for separating the signal events from background-contained candidates, but it also has a dependence on p_T which degrades the separation power at high p_T, while the CPR conversion method has a relatively small separation power in low p_T compared with profile method, but it is almost independent from p_T at high p_T region. It is efficient for this measurement to use both methods. We chose the p_T threshold to be 35 GeV/c, and we use the CES profile efficiencies if EM cluster has $p_T \leq 35$ GeV, and otherwise the CPR conversion efficiencies, then put them into the Eq. (4.5).

The systematic uncertainty of the cross section caused by this combined method comes from both uncertainties of the CES and the CPR efficiencies. We estimate the uncertainty as the quadratic sum of these two uncertainties.

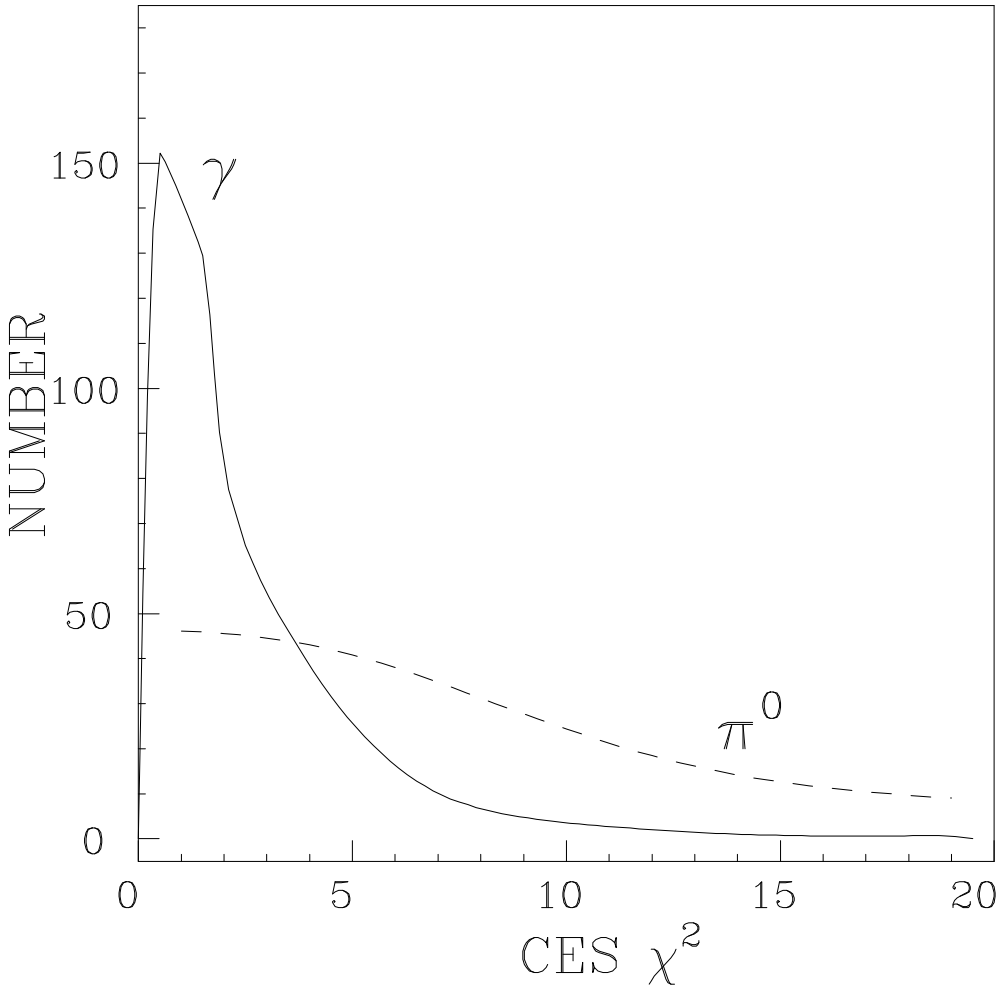

Figure 4.1: Comparison of the CES χ^2 distributions between the simulated single photons and simulated π^0s.

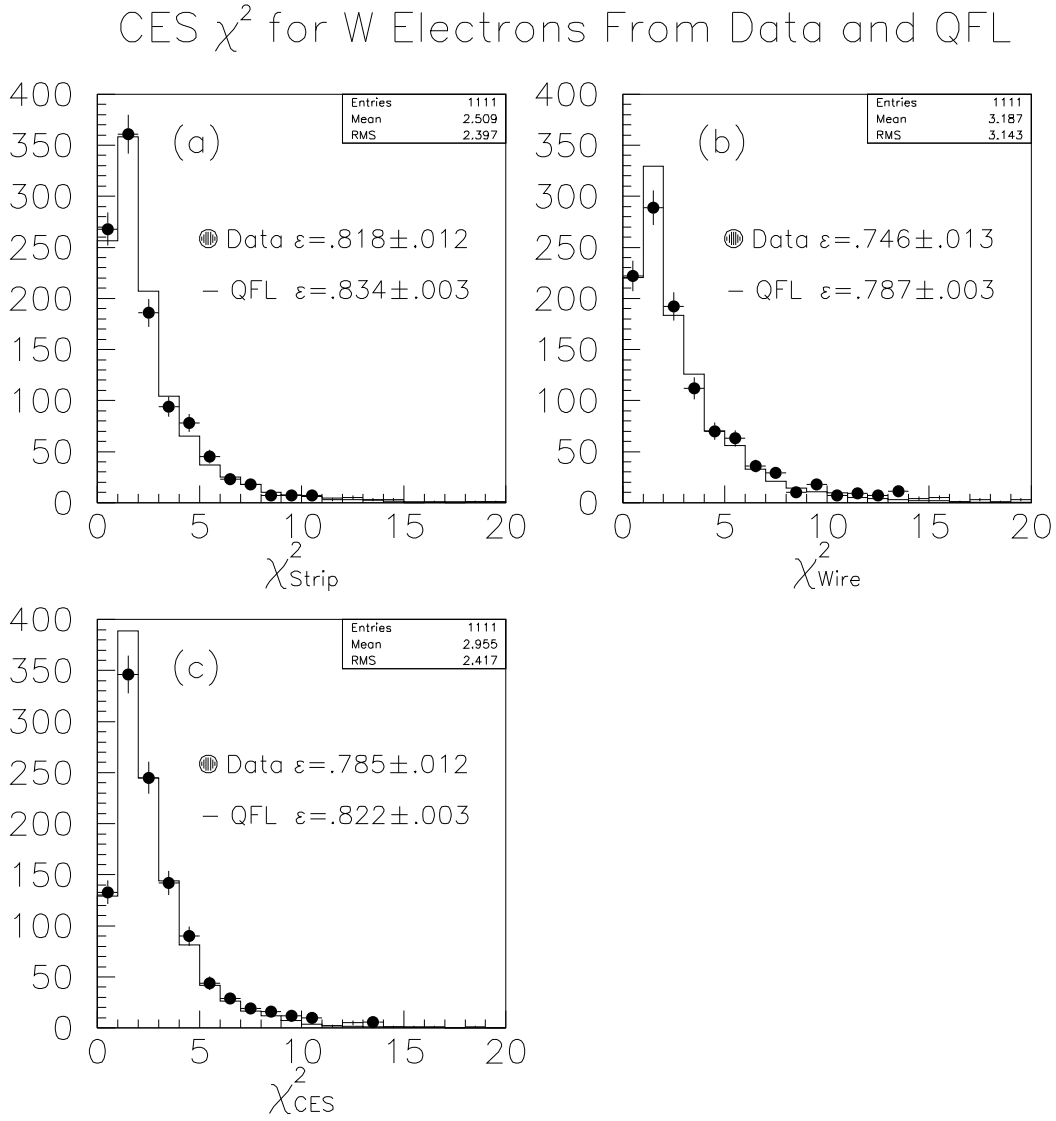

Figure 4.2: Comparison of the CES χ^2 distributions between the real W electrons and the simulated electrons, in (a)strip view, (b)wire view and (c)the average of both views.

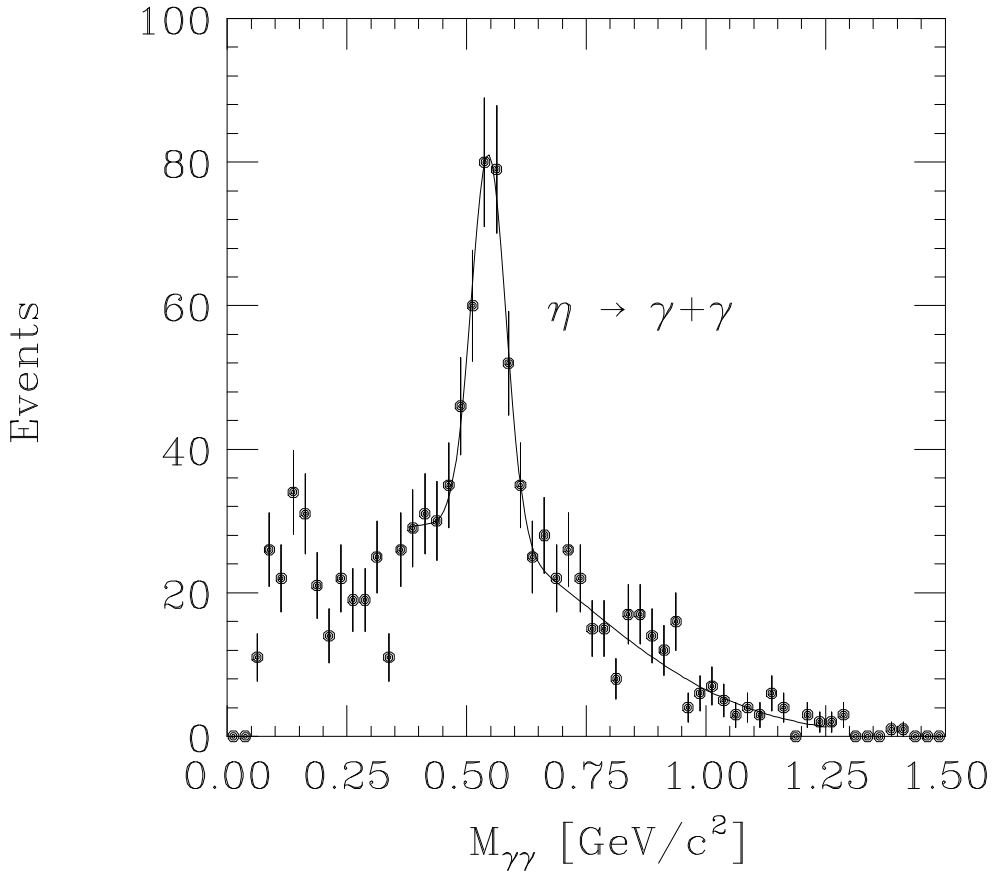

Figure 4.3: Invariant mass distribution of the two photons in η mass region. Points show the data, line shows the result of the fit.

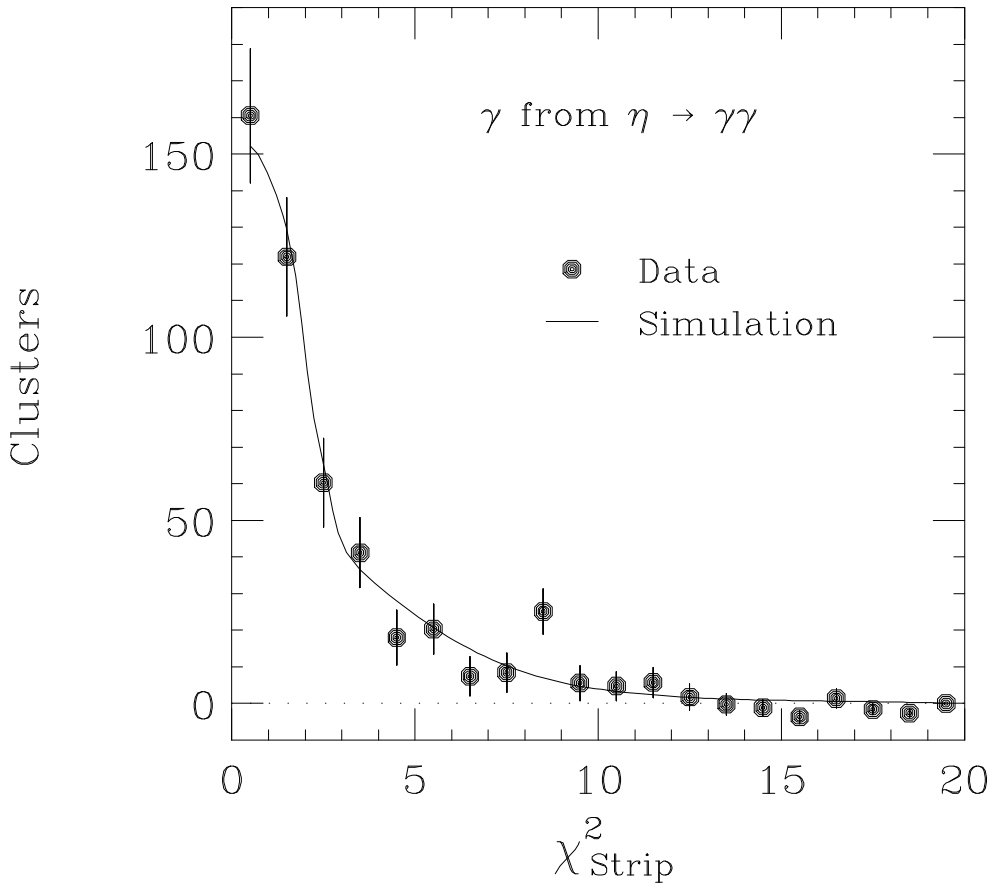

Figure 4.4: The CES χ^2 distributions of the photons from η meson decays in the strip view. Solid line shows the result from the simulation.

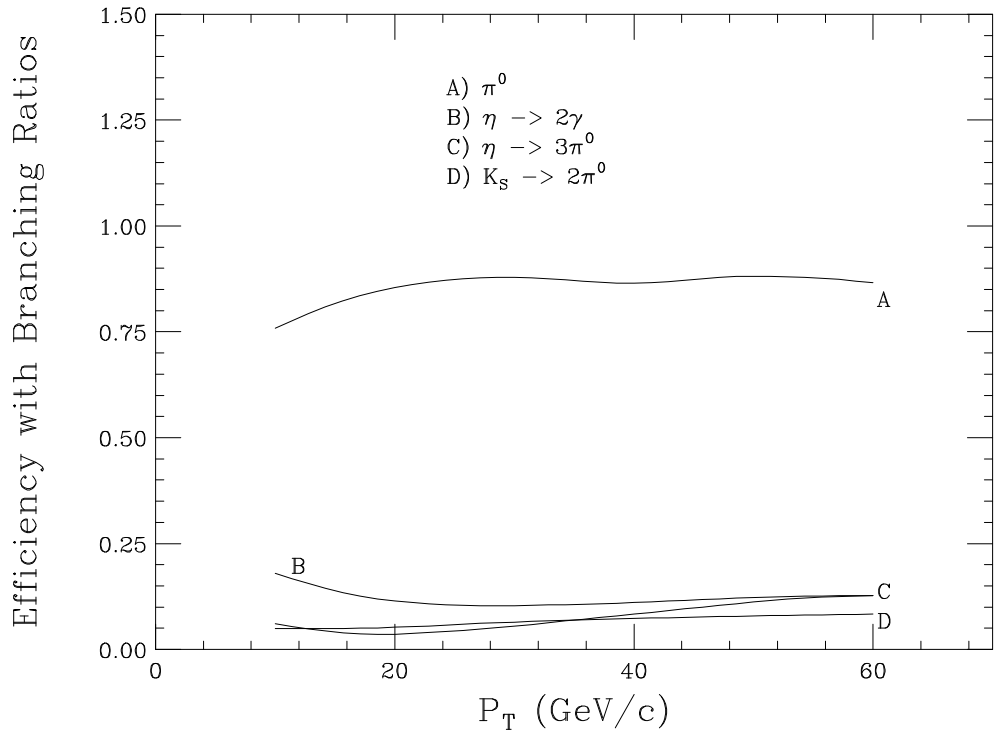

Figure 4.5: The detection efficiency times branching ratio of each background mesons.

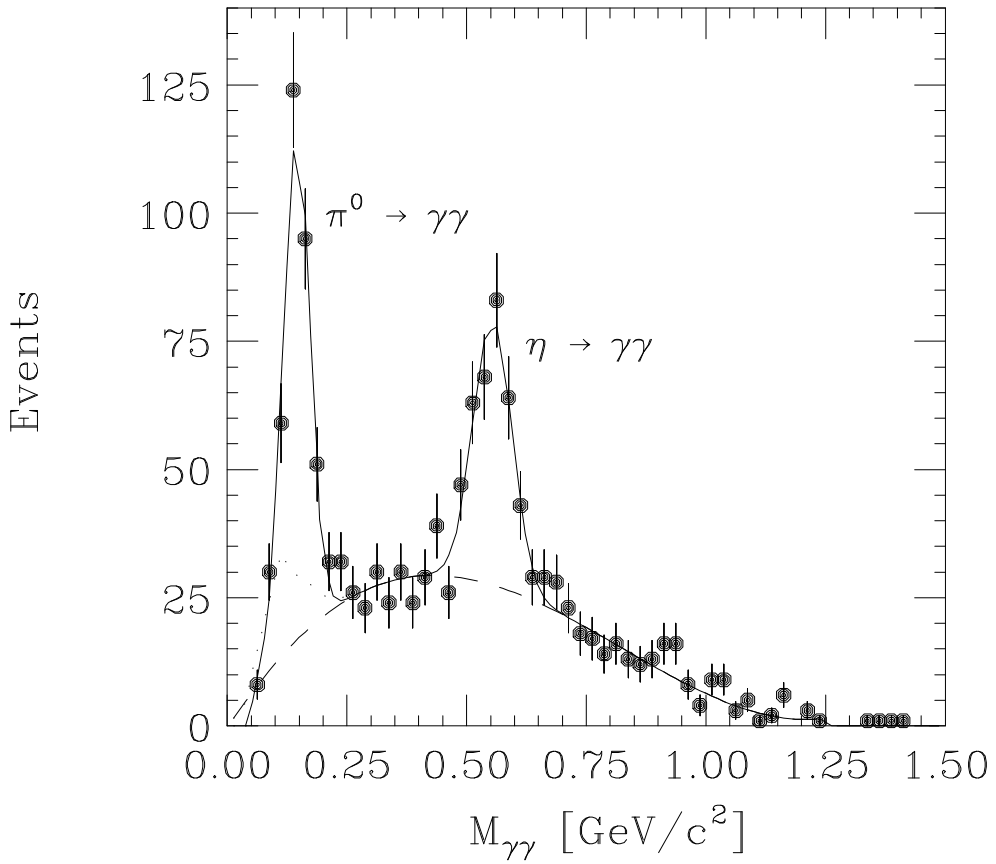

Figure 4.6: Invariant mass distribution of the two photons in π^0 and η mass region. Dashed line is the quadratic fitting for the combinatorial background, dotted line is the effect of the single photons and solid line is the fitted result of the signal plus backgrounds.

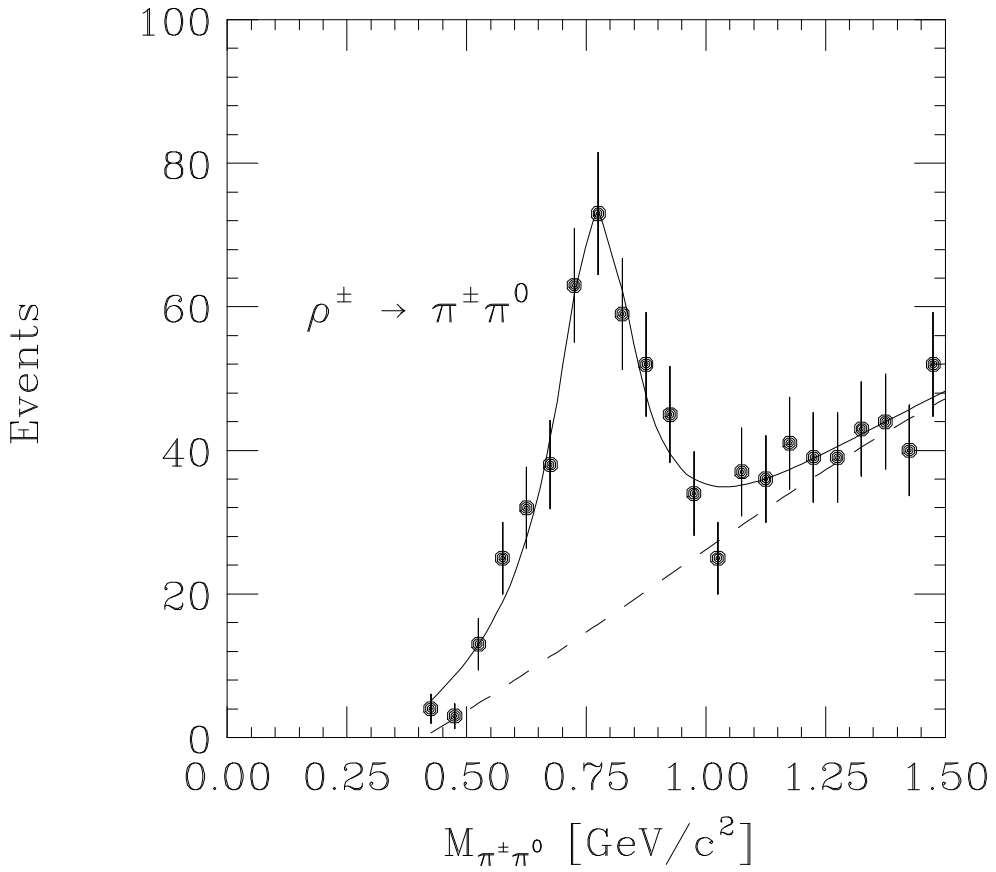

Figure 4.7: Invariant mass distribution of two photons plus a charged track in ρ mass region. the dashed line is the result of the estimation of the combinatorial background, solid line is the fitted result of the signal plus background shape.

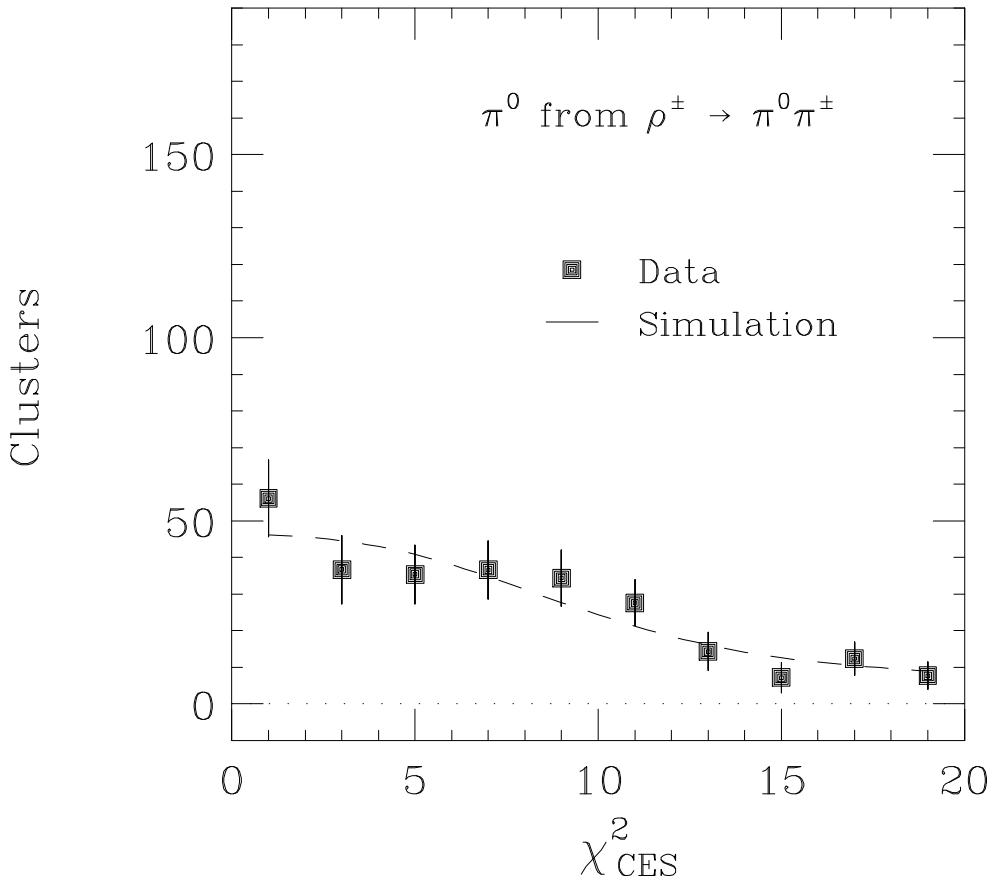

Figure 4.8: The CES χ^2 distribution for π^0's from ρ meson decay and that from the simulation.

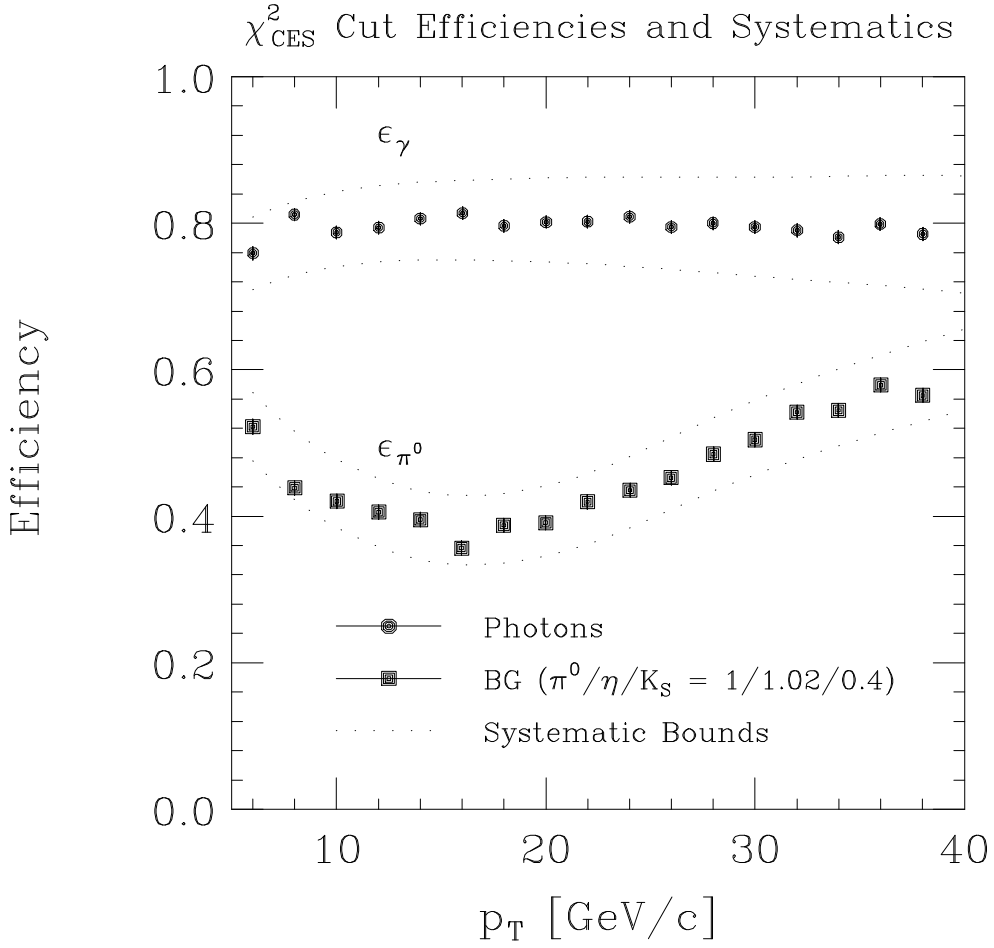

Figure 4.9: χ^2 cut efficiencies for photons and backgrounds. Systematic boundary is also shown.

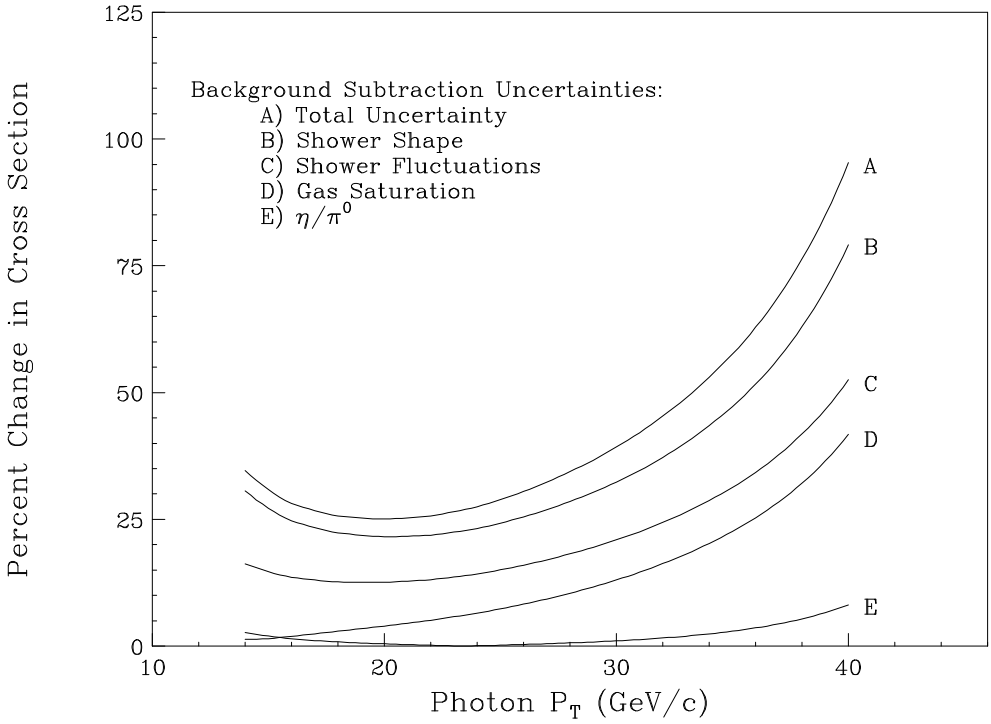

Figure 4.10: Effect of the systematic uncertainties in the χ^2 cut efficiencies on the cross section measurement. Curve A is the total uncertainty, curve B - E are the uncertainties from each source(see text).

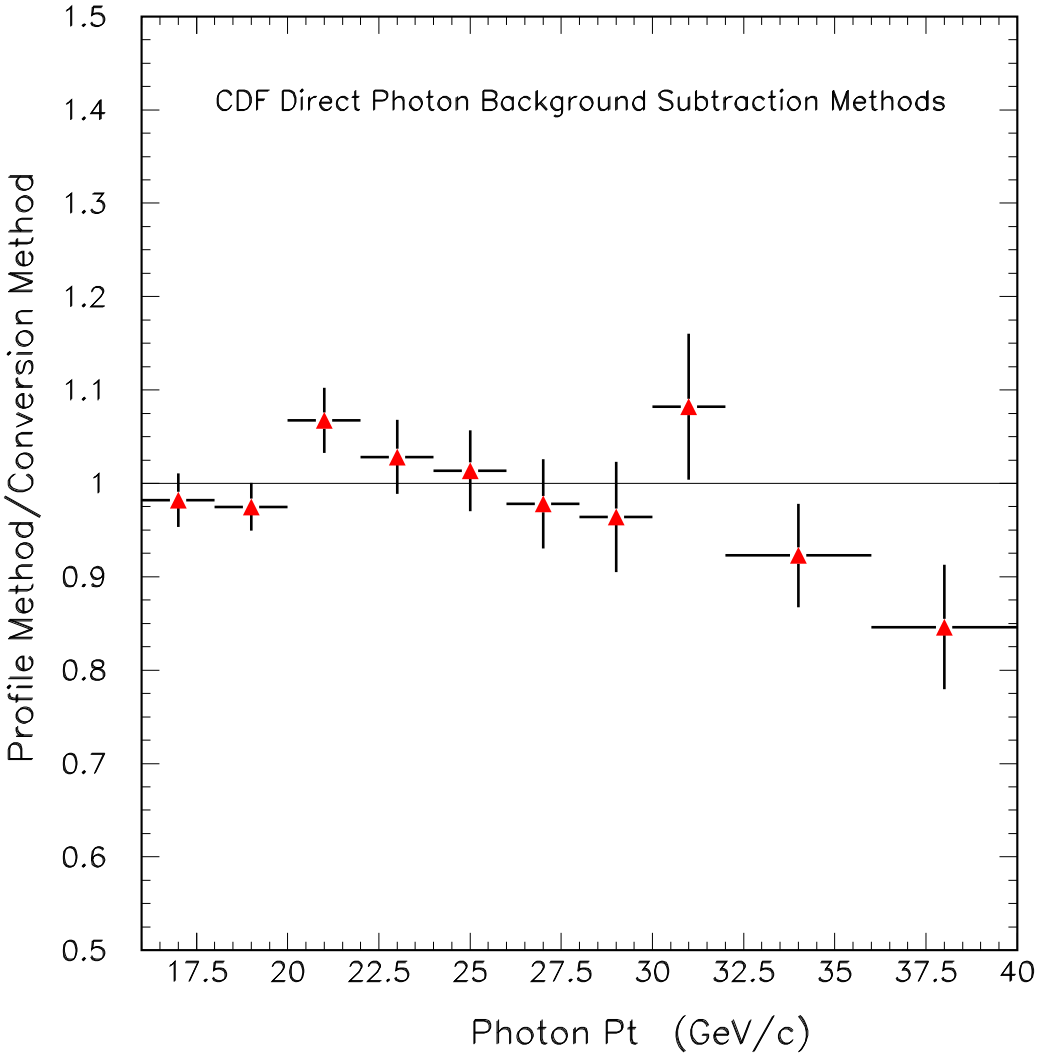

Figure 4.11: Ratio of the number of photons from the profile method and that from the conversion method The error bars are statistical only.

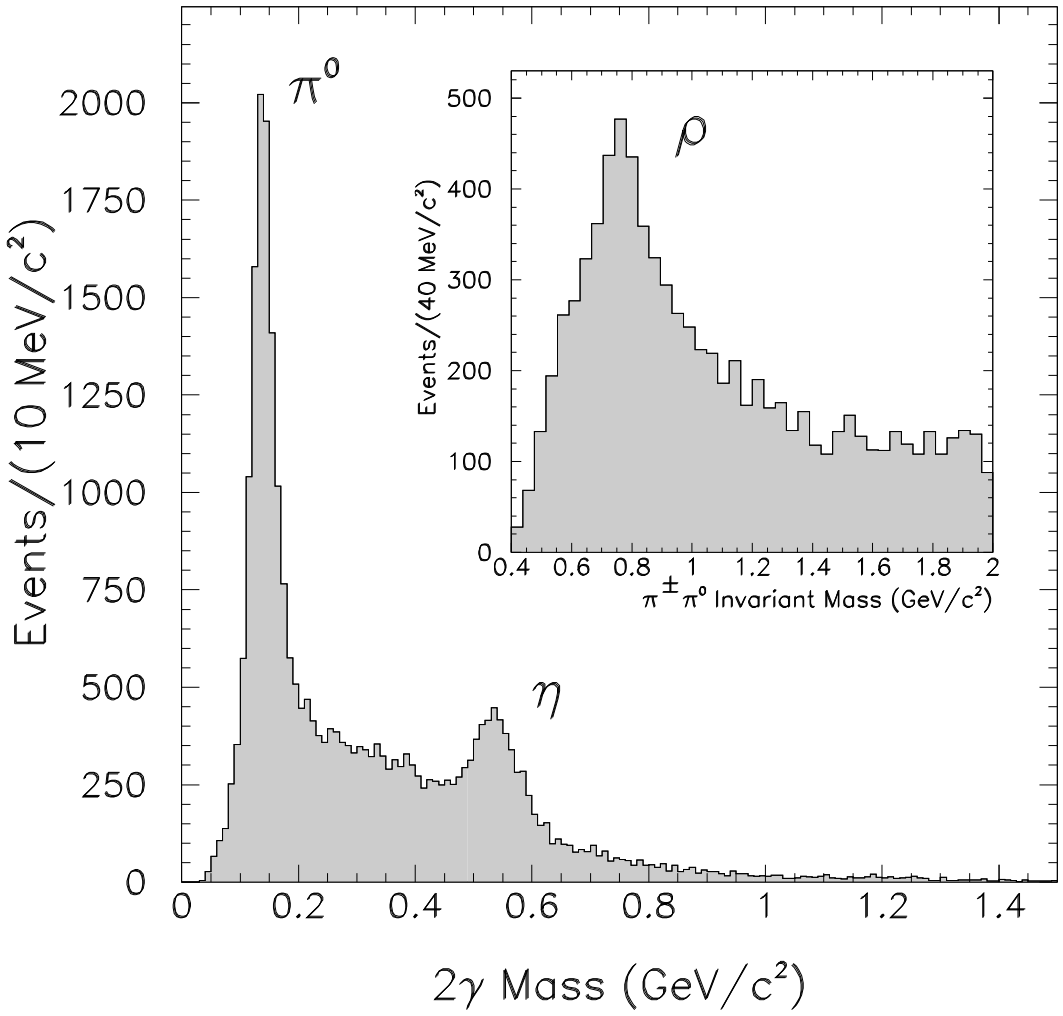

Figure 4.12: Invariant mass distribution of the two photons in π^0 and η mass region. It was used for the calibration of the CPR conversion method.

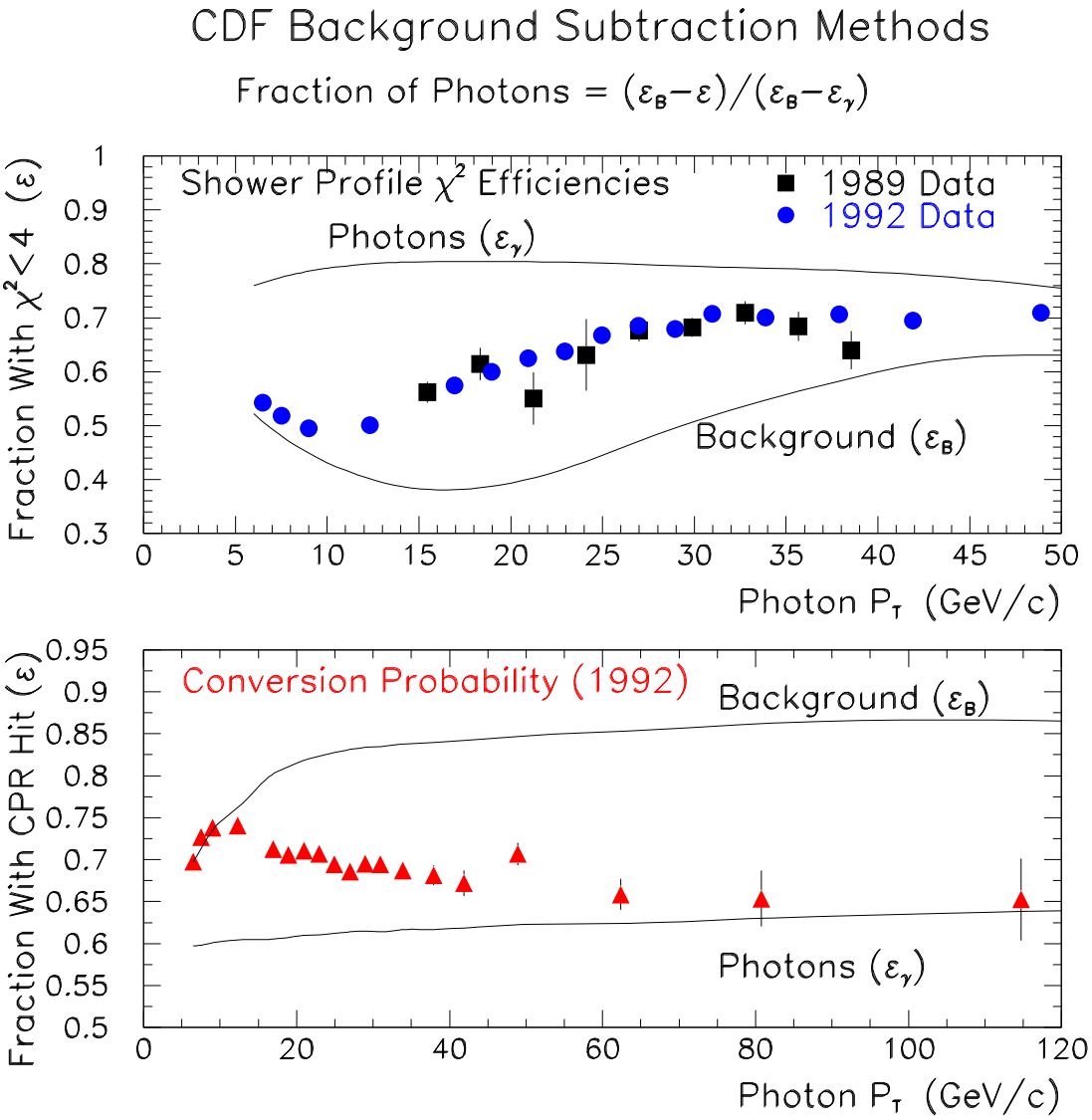

Figure 4.13: Signal and background efficiencies for the CES background subtraction method (upper) and the CPR method (bottom). The fractions of photons from the inclusive photon analysis are also shown for both methods.

Chapter 5

Measuring the Diphoton Cross Section

In this chapter we describe the results of the diphoton cross section as a function of photon p_T, invariant mass of the diphoton system, azimuthal angle difference between photons, the diphoton system p_T, and the p_T ratio (Z).

5.1 Result of the Background Subtraction and Final Diphoton Events

The background subtraction method described in the previous chapter is applied to the final diphoton candidates which are selected in chapter 3. The result is shown in table 5.1. The numbers of total diphoton candidates, estimated real diphoton events and the background events are shown in each photon p_T bin. The number of diphoton events $N_{\gamma\gamma}$ is then used to calculate the photon fraction in the diphoton candidates, and is used to calculate the diphoton cross section.

p_T(GeV/c)	$\langle p_T \rangle$ (GeV/c)	N_{TOT}	$N_{\gamma\gamma}$	$N_{\gamma b}$	N_{bb}
12-14	13.0	348	147.8±32.4	39.0±44.4	161.2±34.5
14-16	14.9	255	85.3±26.8	65.6±37.6	104.2±28.6
16-20	17.7	292	95.8±28.0	69.4±39.8	126.7±30.8
20-24	21.6	126	92.6±21.4	-14.9±27.7	48.4±21.5
24-30	26.6	61	26.1±17.4	9.0±24.4	25.9±18.4
30-48	35.5	50	50.8±34.6	-32.3±41.1	31.6±24.5

Table 5.1: The results of the background subtraction described in Chapter 3.

5.2 Photon Fraction in Diphoton Candidates

Following is a demonstration of how much we have the real diphoton signals after applying our selection criteria.

Applying the background subtraction method to the final diphoton candidates, we can evaluate the number of real diphoton events and background events. Then a photon fraction in our diphoton candidates can be calculated, which is defined by

$$\text{Photon Fraction} \equiv \frac{N_{\gamma\gamma}}{N_{TOT}}, \tag{5.1}$$

where $N_{\gamma\gamma}$ shows the number of real diphoton events and N_{TOT} is the number of total diphoton candidates. Figure 5.1 is the measured photon fraction in our diphoton candidates, as a function of p_T of the photons. It shows that the photon fraction becomes higher when p_T becomes larger. It indicates that the selection criteria used in this analysis makes the candidates pure at high p_T region.

We have also measure the photon fraction in the inclusive photon sample, which is shown in Fig. 5.2. The diphoton result shows the similar shape compared with that of the inclusive photon measurement.

ITEM	*VALUE*
Uncertainty of CES background subtraction	15 % ($12 \leq E_T \leq 30$ GeV)
Uncertainty of CPR background subtraction	10 % ($E_T \geq 30$ GeV)
Uncertainty of L2 Trigger Efficiency	2 %
Uncertainty of Isolation Cut	1 %
Uncertainty of no-tracks requirement	1 %
Uncertainty of Photon Energy Scale	4.5 %
Uncertainty of Luminosity	8 %

Table 5.2: Summary of systematic uncertainties.

5.3 The Diphoton Cross Section

In this section we first summarize the the systematic uncertainties from various sources, then show the procedure of evaluating the diphoton cross section with the estimated efficiencies described in chapter 3. The results are compared with the NLO QCD calculation: $\bar{\mathrm{p}}\mathrm{p} \rightarrow \gamma\gamma X$ [13].

5.3.1 Summary of the Systematic Uncertainties

Table 5.2 shows the summary of the systematic uncertainties in measured cross section.

The uncertainties on the background subtraction with the CES and the CPR come from the uncertainties of the efficiencies for the CES profile method and the CPR conversion method, which are described in chapter 4. They make 15 % cross section uncertainty on the CES method and 10 % on the CPR method. By taking the quadratic sum of these uncertainties, the systematic uncertainty of using both the CES and the CPR background subtraction methods are evaluated.

The total systematic uncertainty was 21%. It is dominated by the uncertainty from the background subtraction.

5.3.2 Evaluation of the Diphoton Cross Section

The diphoton cross section is calculated by correcting the events for the efficiencies of the each selection criterion and the level 2 trigger in each bin. The result is then divided by the width of each p_T bin (mass, diphoton system p_T, $\Delta\phi$ and $Z = p_T^{(2)}/p_T^{(1)}$), and the total integrated luminosity,

$$\frac{d\sigma_{\gamma\gamma}}{dp_T} = \frac{N_{\gamma\gamma}}{\epsilon_{\rm TOT} L \Delta p_T}, \tag{5.2}$$

where $\epsilon_{\rm TOT}$ is the total efficiency, L is the total integrated luminosity and Δp_T is the width of each p_T bin.

We use the efficiency in table 3.2 described in chapter 3. The total efficiency is

$$\epsilon_{\rm TOT} = {\epsilon_{\rm fid}}^{(1)} \cdot {\epsilon_{\rm fid}}^{(2)} \cdot {\epsilon_{\rm conv}}^{(1)} \cdot {\epsilon_{\rm conv}}^{(2)} \cdot {\epsilon_{\rm trk}}^{(1)} \cdot {\epsilon_{\rm trk}}^{(2)} \cdot {\epsilon_{\rm iso}}^{(1)} \cdot {\epsilon_{\rm iso}}^{(2)} \cdot \epsilon_{\rm zvert} \cdot {\epsilon_{\rm ext}}^{(1)} \cdot {\epsilon_{\rm ext}}^{(2)} \cdot \epsilon_{\rm L2} \,. \tag{5.3}$$

Figure 5.3 shows the diphoton cross section as a function of photon p_T, where each event is entered twice, once for each p_T of the 2 photons. The solid line shows the NLO QCD predictions with CTEQ2M [12] structure functions. The systematic uncertainties in the diphoton cross section are shown as error bars in this plot. The result is in qualitative agreement with the NLO QCD predictions. The numerical values for the diphoton cross section are listed in Table 5.3.

We also measured the diphoton cross sections as a function of the invariant mass of the diphotons, $\Delta\phi$ between photons, diphoton system p_T and the p_T ratio (Z) of the photons, which are shown in Fig. 5.4, 5.5, 5.6 and 5.7, respectively. Z is defined by

$$Z = \frac{p_T^{(2)}}{p_T^{(1)}}, \tag{5.4}$$

where $p_T^{(1)}$ and $p_T^{(2)}$ show the p_T's of leading and next-to-leading photon, respectively.

p_T(GeV/c)	$\langle p_T \rangle$	$d\sigma_{\gamma\gamma}/dp_T$(pb/GeV/c)	Stat. (%)	Sys. (%)
12-14	13.0	4.95	17	21
14-16	14.9	3.00	23	21
16-20	17.7	1.94	19	21
20-24	21.6	1.45	20	21
24-30	26.6	0.38	42	20
30-48	35.5	0.22	49	21

Table 5.3: The diphoton cross section as a function of photon p_T. Statistical and systematic errors are also listed.

M(GeV/c^2)	$\langle M \rangle$	$d\sigma_{\gamma\gamma}/dM$(pb/GeV/c^2)	Stat. (%)	Sys. (%)
10-20	15.2	0.166	39	21
20-25	23.4	0.399	48	20
25-30	27.7	0.739	30	21
30-35	32.3	0.650	33	21
35-45	38.8	0.232	44	21
45-60	50.3	0.166	39	20
60-120	75.7	0.0179	125	21

Table 5.4: The diphoton cross section as a function of the invariant mass of the diphotons. Statistical and systematic errors are also listed.

$\Delta\phi$(Rad)	$\langle \Delta\phi \rangle$	$d\sigma_{\gamma\gamma}/d\Delta\phi$(pb/Rad)	Stat. (%)	Sys. (%)
2.62-2.84	2.74	4.00	116	21
2.84-2.94	2.89	18.8	56	20
2.94-3.04	2.99	43.1	24	21
3.04-3.09	3.06	49.5	34	21
3.09-3.14	3.12	58.9	56	21

Table 5.5: The diphoton cross section as a function of the $\Delta\phi$ between the diphotons. Statistical and systematic errors are also listed.

p_T(GeV/c)	$\langle p_T \rangle$	$d\sigma_{\gamma\gamma}/dp_T$(pb/GeV/c)	Stat. (%)	Sys. (%)
0-1	0.66	1.33	46	21
1-3	2.11	1.46	34	21
3-5	3.98	1.27	40	20
5-8	6.58	1.02	52	21
8-13	10.1	0.53	36	21

Table 5.6: The diphoton cross section as a function of p_T of the diphoton system. Statistical and systematic errors are also listed.

Z	$\langle Z \rangle$	$d\sigma_{\gamma\gamma}/dZ$(pb)	Stat. (%)	Sys. (%)
0.45-0.70	0.617	17.535	4.658	21
0.70-0.85	0.784	28.253	9.289	21
0.85-0.95	0.898	28.888	16.423	21
0.95-1.00	0.970	46.509	18.120	21

Table 5.7: The diphoton cross section as a function of Z of the diphoton system. Statistical and systematic errors are also listed.

The explicit values are listed in table 5.4, 5.5, 5.6 and 5.7 for mass, $\Delta\phi$, system p_T and Z, respectively.

The results of the invariant mass and $\Delta\phi$ show the qualitative agreement with the NLO predictions, as is seen in the photon p_T result, while the cross sections as a function of diphoton system p_T and Z show the slight differences compared with the theory.

5.4 Discussion

5.4.1 Effect of the Initial Soft Gluon Radiation and Intrinsic k_T

As we discussed in chapter 1, comparison of the diphoton system p_T distribution from data with that from the NLO predictions reflects the effect of the initial soft gluon radiations and intrinsic transverse momentum of initial partons, because the NLO predictions include at most one gluon emission at the initial state, and it does not take the intrinsic k_T into account. While the parton shower Monte Carlo like PYTHIA simulates them. It is interesting to compare the data with these NLO and Monte Carlo distributions quantatively.

5.4.2 Kolmogorov-Smirnov Test for Diphoton System p_T Distribution

Here we demonstrate the comparisons of the diphoton system p_T distribution between the data, NLO predictions, and also between the data and the Monte Carlo with the "Kolmogorov-Smirnov (KS) Test" [43][44].

The KS test is often applied to see if two distributions are different; that is, to see if we can disprove the null hypothesis that they are drawn from the same population distribution function. This test gives the probability of the consistency between two given distributions. It is often used to compare the distribution of the data with the theory line or Monte Carlo distribution.

First the data was rebooked to the histogram with the bin size of 1 GeV/c. Both data, NLO and PYTHIA system p_T distributions were integrated from $0 \leq p_T \leq 12$ GeV/c. They were normalized at p_T=12GeV/c. Figure 5.8 shows these cumulative distributions of the data, NLO and PYTHIA. Then the KS test was applied to them. The most

different point between the data and the NLO was selected with these distributions (we call it D).

The Kolmogorov function is defined by

$$Q_{KS}(\lambda) = 2\sum_{i=1}^{\infty}(-1)^{i-1}e^{-2\,i^2\lambda^2} \tag{5.5}$$

where $\lambda = \sqrt{N}D$, N is the number of bins for the data. It corresponds to the probability of the consistency between these distributions. In this measurement, the probability of the consistency between the data and the NLO was estimated to be 0.13, while the consistency between data and PYTHIA Monte Carlo was 0.91. This test supports that the Monte Carlo, which includes both the multiple initial soft gluon radiations and the intrinsic k_T of the initial partons, describes the shape of the diphoton system p_T distribution better than the NLO.

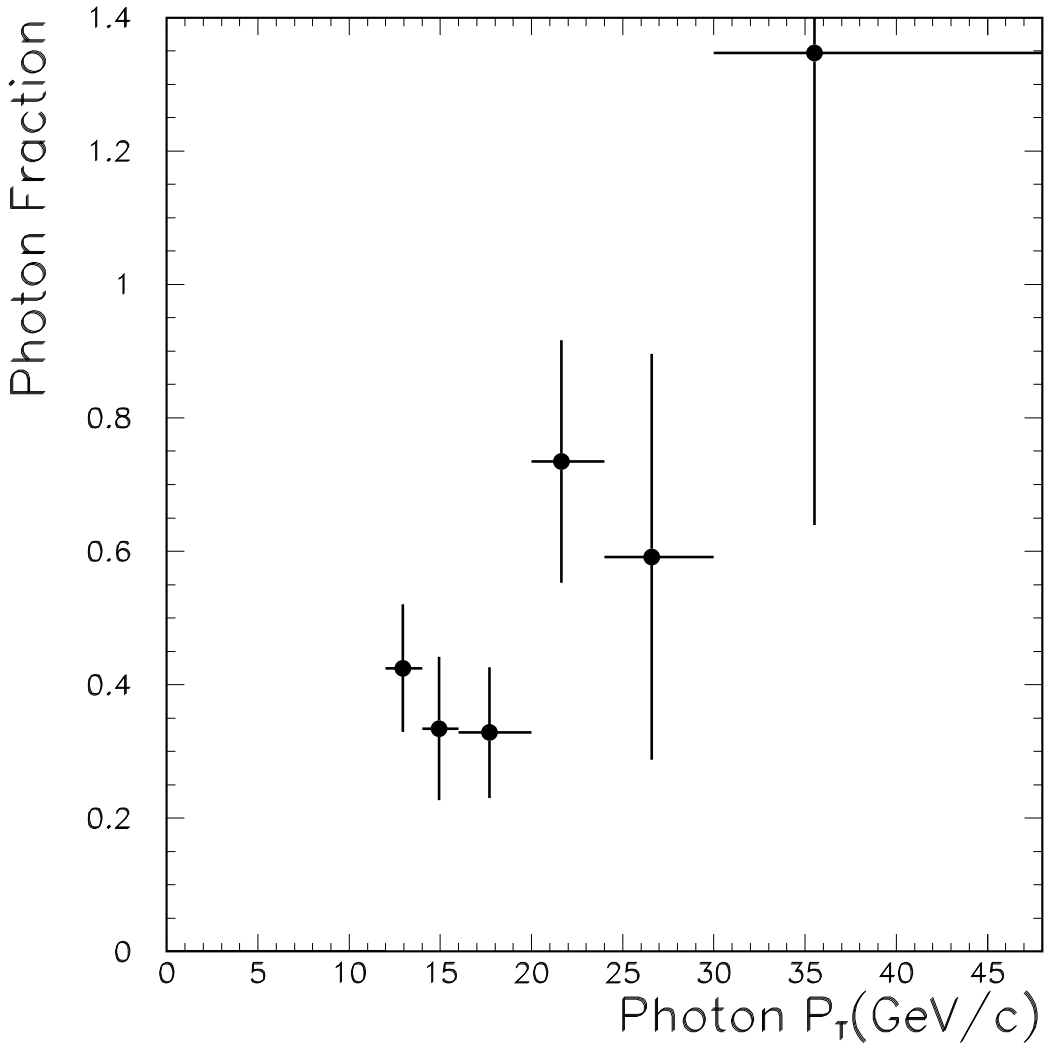

Figure 5.1: Photon fraction in the diphoton candidate as a function of photon p_T.

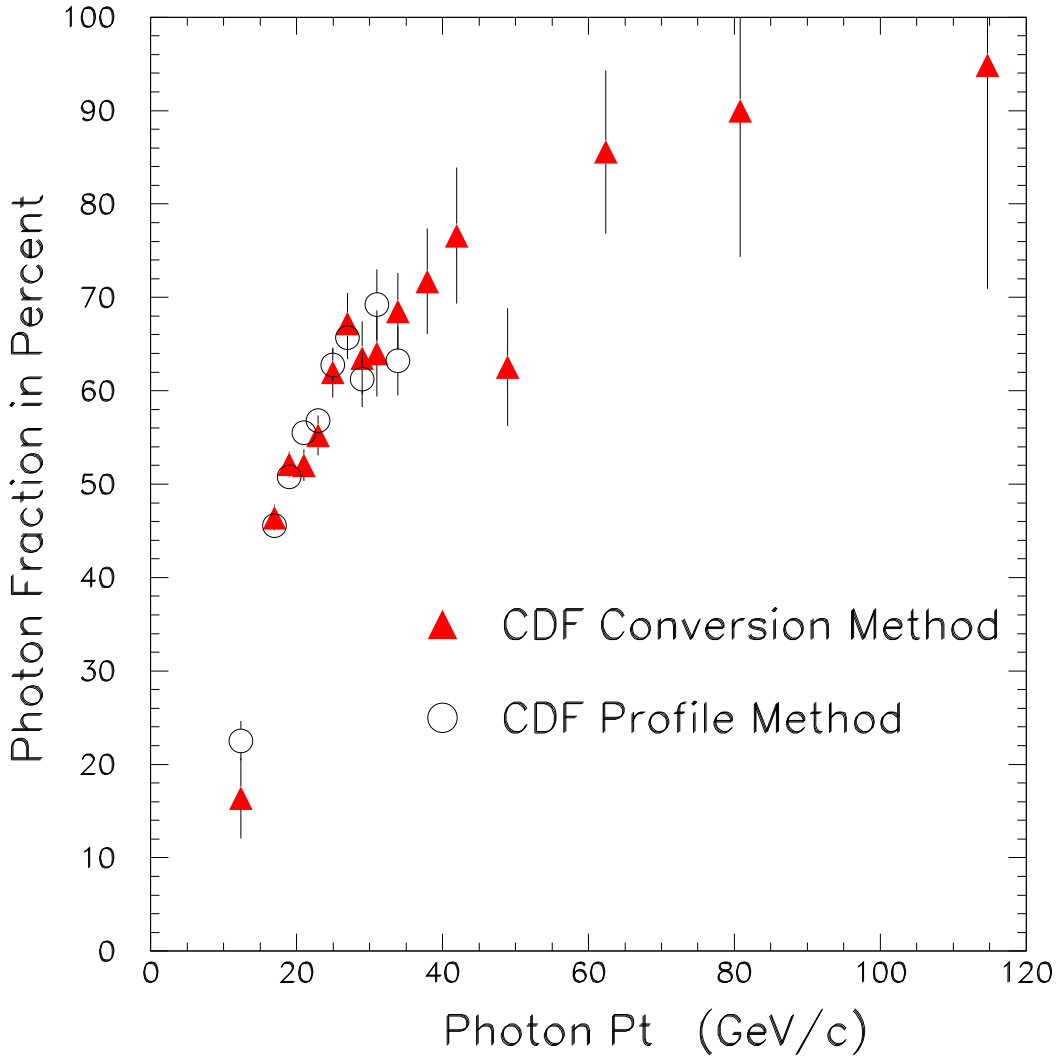

Figure 5.2: Photon fraction in the inclusive photon candidate as a function of the photon p_T. Open circles show the photon fraction measured only by the CES method, triangles show the photon fraction measured only by the CPR method.

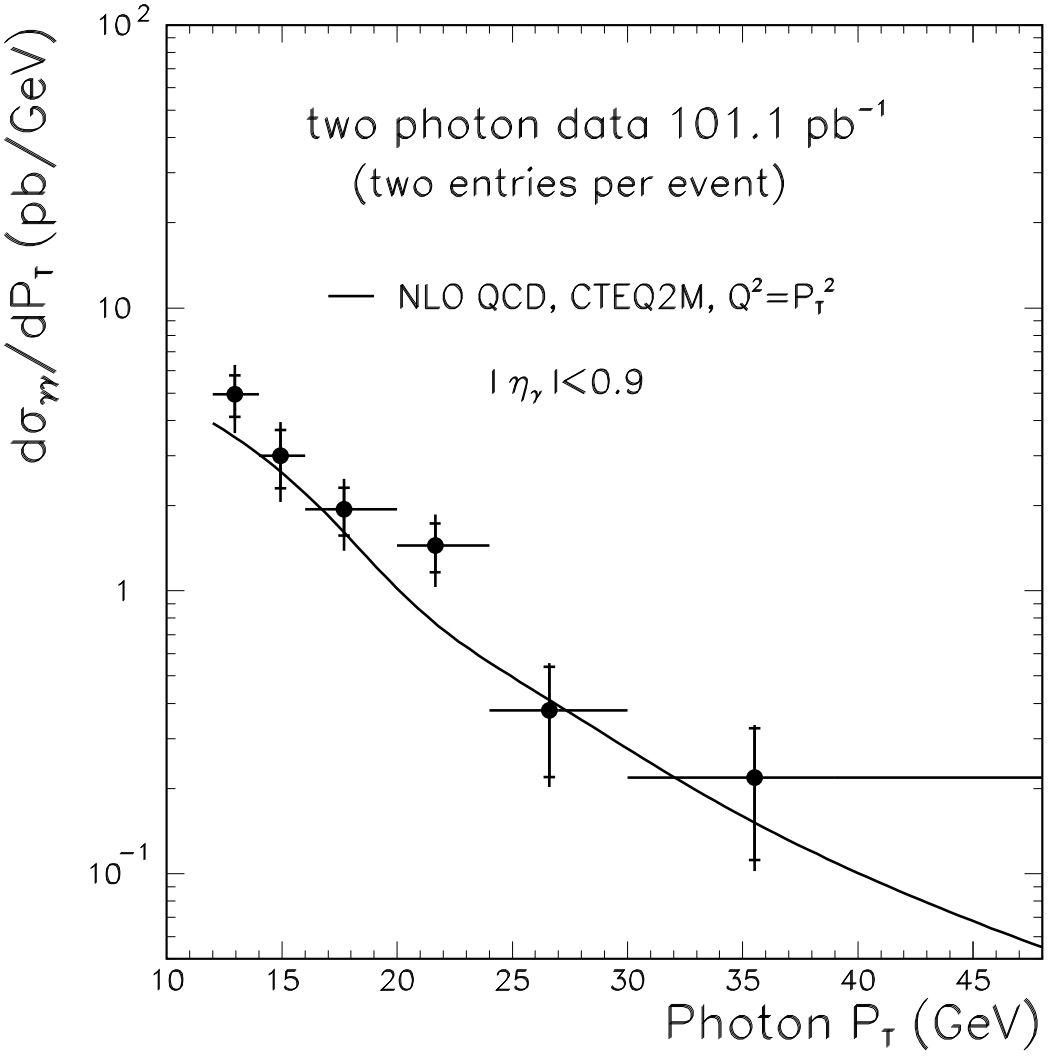

Figure 5.3: The cross section of the diphoton production as a function of photon p_T. Circles show the measured cross section. The statistical errors and the quadratic sum of the statistical and the systematic errors are superimposed. Solid line shows the NLO QCD prediction with the CTEQ2M parton distribution function.

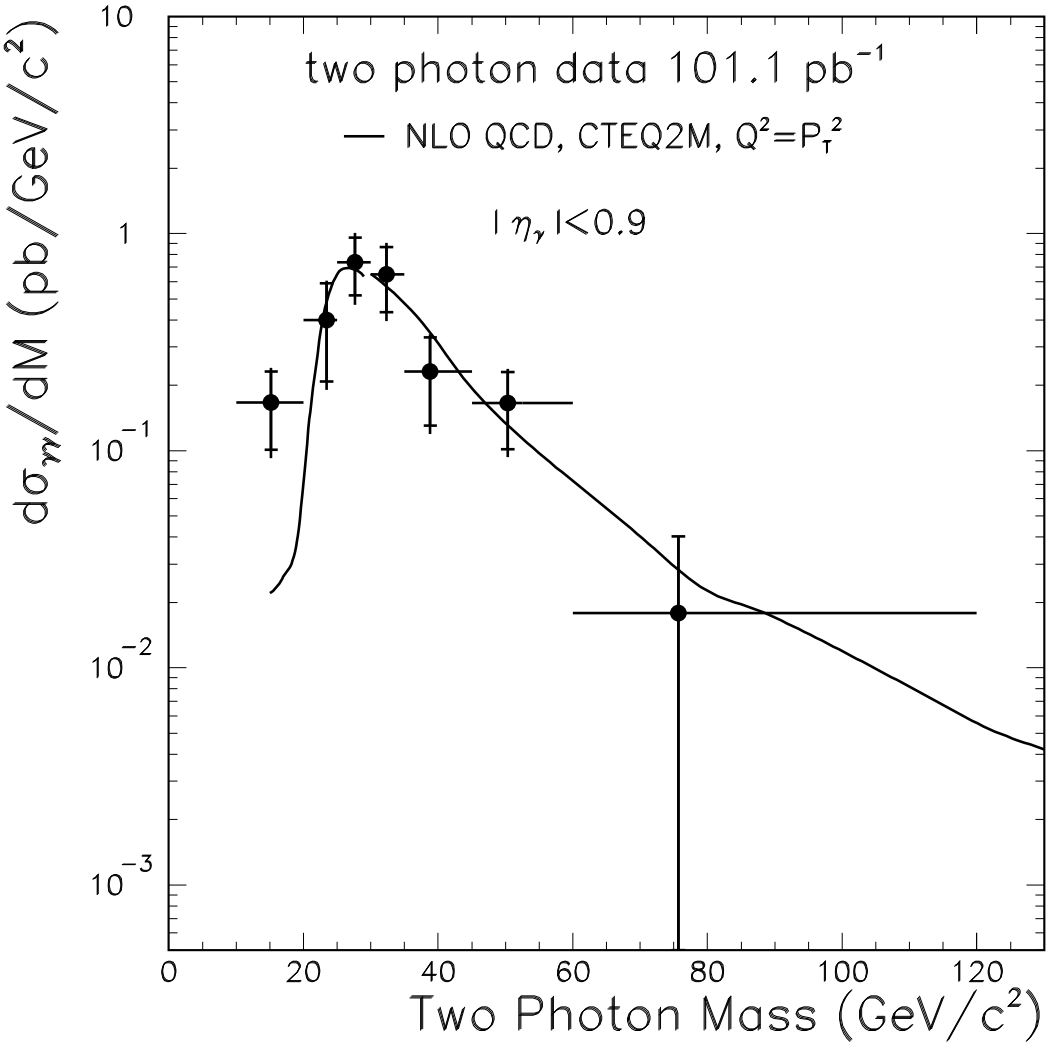

Figure 5.4: The cross section of the diphoton production as a function of the invariant mass of the diphotons. Solid line shows the NLO QCD prediction.

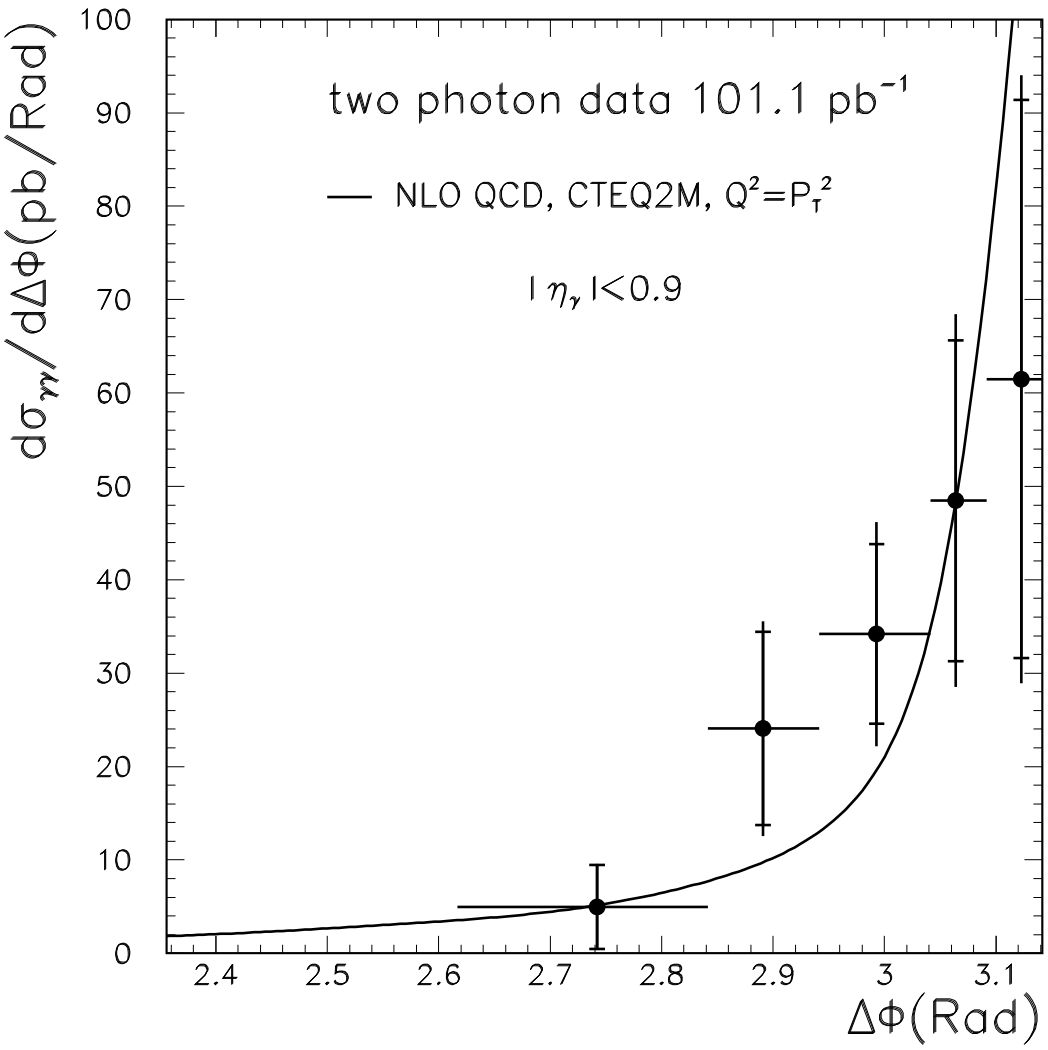

Figure 5.5: The cross section of the diphoton production as a function of $\Delta\phi$ between photons. Solid line shows the NLO QCD prediction.

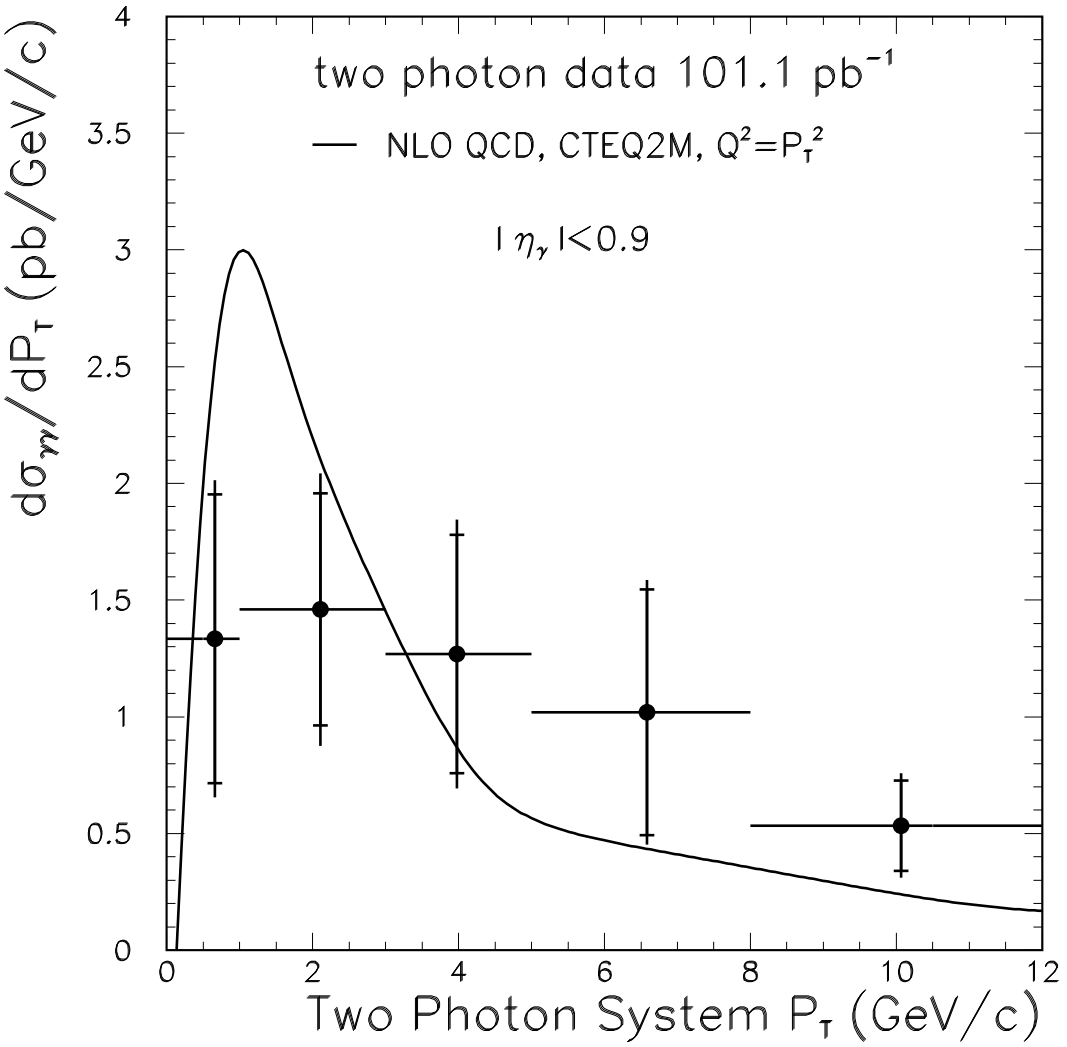

Figure 5.6: The cross section of the diphoton production as a function of the system p_T of the diphotons. Solid line shows the NLO QCD prediction.

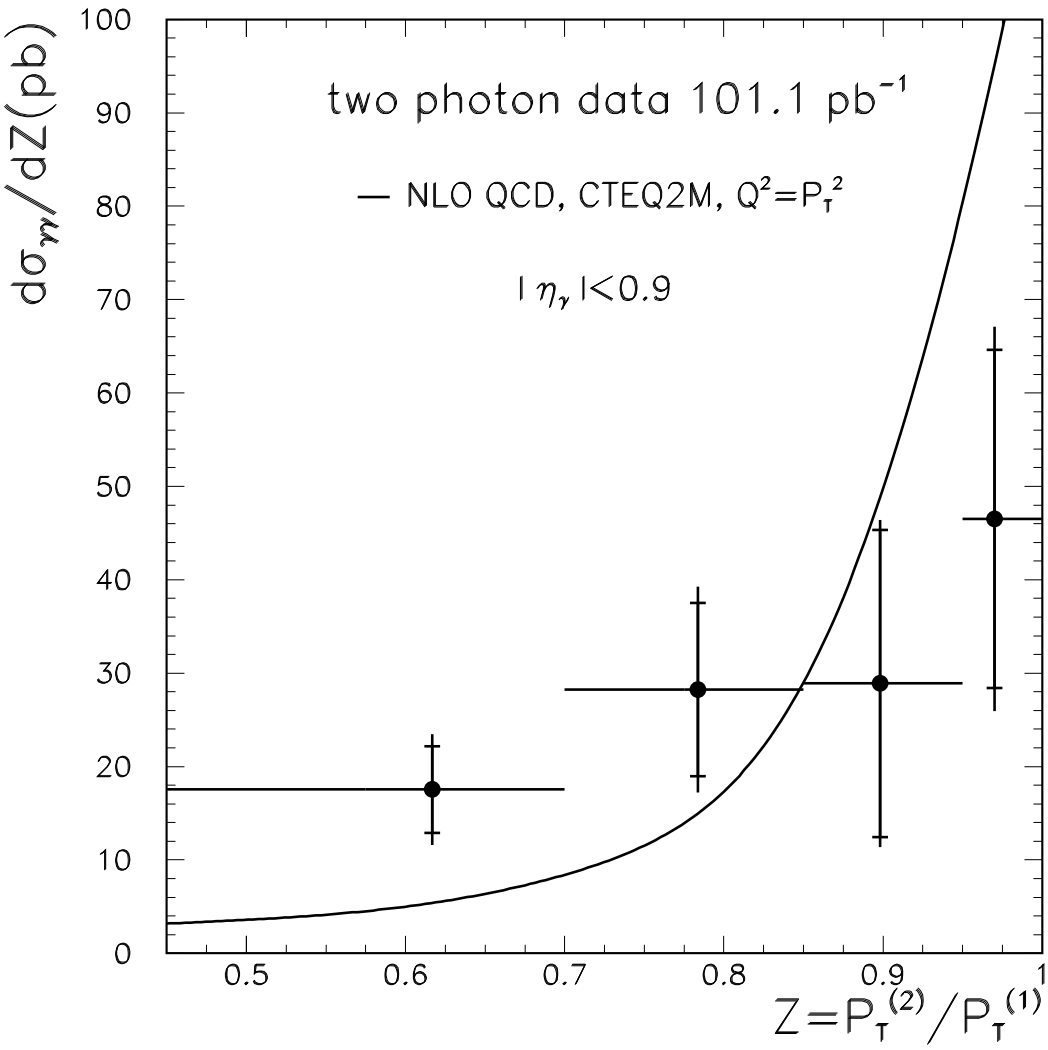

Figure 5.7: The cross section of the diphoton production as a function of the p_T ratio of the diphotons. Solid line shows the NLO QCD prediction.

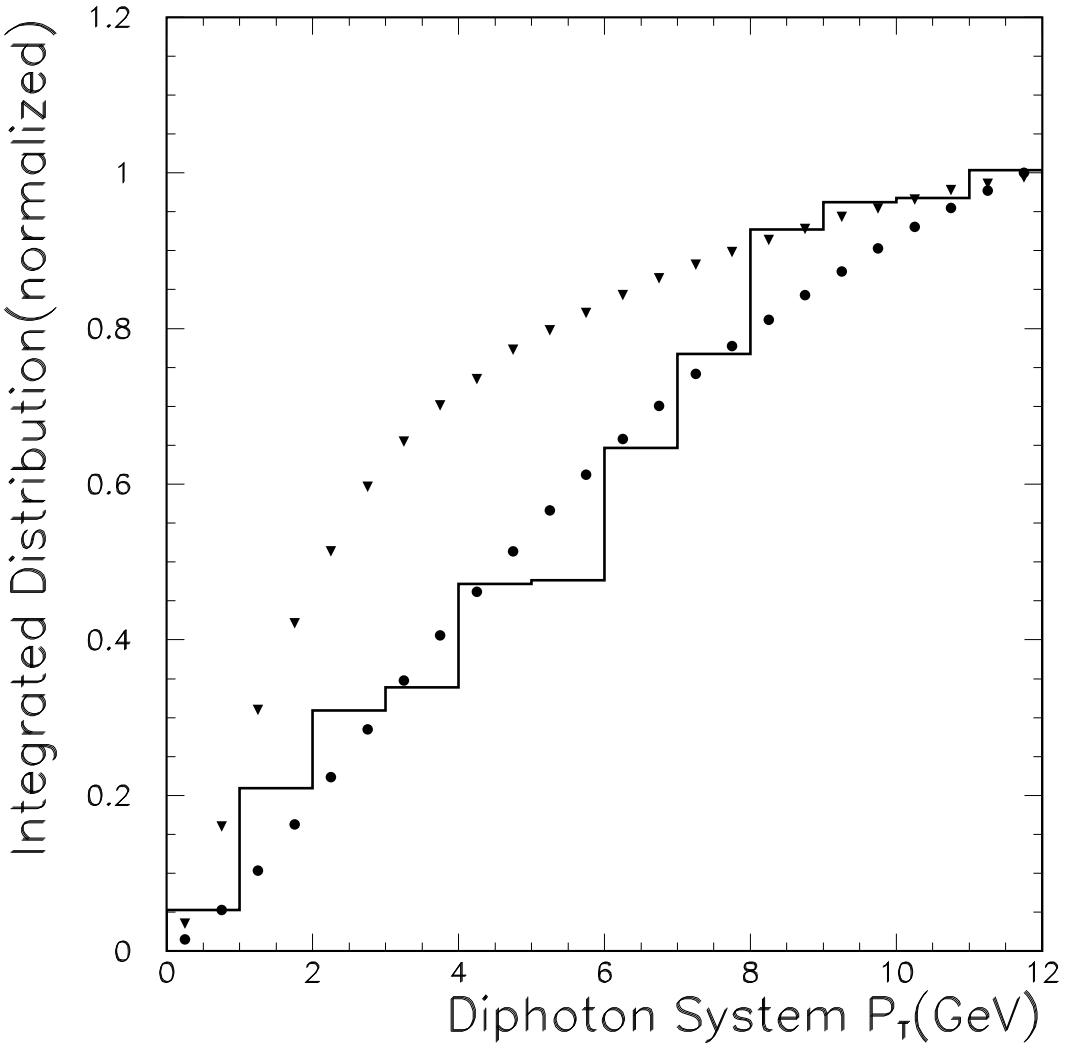

Figure 5.8: Integrated distributions of the cross section as a function of diphoton system p_T, normalized at p_T=12 GeV/c. Histogram shows the data, triangle shows the NLO predictions and circle shows the PYTHIA Monte Carlo.

Chapter 6

Conclusion

We have measured the prompt diphoton production cross section at a center of mass energy $\sqrt{s} = 1.8\,\mathrm{TeV}$. The differential cross section was evaluated as a function of p_T of photons, the invariant mass of the diphotons, $\Delta\phi$ between photons, $Z = p_T^{(2)}/p_T^{(1)}$ and the transverse momentum of the diphoton system, to compare it with the NLO QCD predictions with CTEQ2M parton distribution functions. The total systematic uncertainty in this analysis was estimated to be 21%.

The results, as a function of p_T, the invariant mass and $\Delta\phi$, were in qualitatively agreement with the theory, while the slight differences were seen in the results as a function of p_T of the diphoton system and of the p_T ratio between the data and the theory.

The difference of the diphoton system p_T between the data and the NLO, and also between the data and PYTHIA were quantified with the Kolmogorov-Smirnov test. The probability of the consistency between the data and the NLO predictions was estimated to be 0.13, while the consistency between the data and PYTHIA Monte Carlo, which includes the effects of the multiple initial soft gluon radiations and intrinsic k_T of the initial partons, was estimated to be 0.91. PYTHIA Monte Carlo explains the diphoton system p_T distribution better than the NLO.

Appendix A

The Standard Selection Criteria for Electrons

In this appendix we describe the standard selection criteria for electrons used in CDF analysis, especially for the variables from CES clustering; E/P, Had/EM and lateral shower sharing (L_{shr}).

A.1 The Selection Criteria for Electrons

A.1.1 3D Track Cut

As is seen in the photon selection, 3D track cut is essential for electron analysis to distinguish the EM cluster for photons from that from electrons. It is required to be

$$\text{Number of 3D tracks} \geq 1, \tag{A.1}$$

for high p_T electron analysis, and

$$\text{Number of 3D tracks} = 1, \tag{A.2}$$

for low p_T electron analysis. We used the latter cut in this analysis.

A.1.2 E/P

The variable we call E/P is defined by

$$E/P \equiv \frac{E_T}{p_T}, \tag{A.3}$$

where E_T is the transverse energy measured in CEM, p_T is the transverse momentum measured in CTC. Since the particles from $\bar{\text{p}}\text{p}$ collisions are considered to be massless, the ratio of E_T and p_T should be 1. Since the difference of the resolution of E_T and p_T the shape of E/P becomes broad, and it has a longer tail at high E/P because of the mismeasurement of the p_T from the photon radiation from the particle.

In CDF standard electron selection criteria, E/P is required to be

$$E\,/\,P \leq 1.8. \tag{A.4}$$

A.1.3 Had/EM

As the CEM is designed so that the electron deposits almost its energy to the CEM, the ratio of the transverse energy of the CHA and that of the CEM, called Had/EM, is a good parameter to discriminate the backgrounds for electrons. In the standard electron analysis, the following criterion,

$$Had/EM \leq 0.05\,, \tag{A.5}$$

is required to the electron dataset.

A.1.4 Lateral Shower Sharing: L_{shr}

The lateral shower sharing of the EM cluster energy among the tower is the variable for the difference of the energy spread in η direction between the real data and the testbeam data. It is defined by

$$L_{shr} \equiv 0.14 \sum_i \frac{E_i^{meas} - E_i^{pred}}{\sqrt{(\Delta E)^2 + \left(\Delta E_i^{pred}\right)^2}}, \tag{A.6}$$

where E_i^{meas} is the energy deposition in the CEM tower i, E_i^{pred} is the expected energy deposition in the CEM tower i, ΔE is the uncertainty in the energy measurement with the CEM ($\Delta E = 0.14/\sqrt{E}$) and ΔE_i^{pred} is the error associated with E_i^{pred}. The sum runs over the two towers in η direction adjacent to the seed tower. E_i^{pred} is determined by the CDF testbeam data, as a function of the seed tower energy and the direction of the CES shower center relative to the event vertex. ΔE_i^{pred} is given by the propagation of the error of the shower center measurement in the CES to the predicted energy E_i^{pred}.

In the electron selection, it is required to be a small value;

$$L_{shr} \leq 0.2. \tag{A.7}$$

Appendix B

Standard CES Profile

In this appendix we describe the standard CES profile of the electron evaluated from the CDF central calorimeter testbeam done at 1985.

B.1 Standard CES Profile

The profiles are evaluated for both the CES analysis and the simulations. We define $f(x)$ and $I(x)$, the instantaneous and the integrated fractional energies in 1 mm bins respectively:

$$f(x) = \int_{x-1}^{x} \rho(x')dx', \tag{B.1}$$

$$I(x) = \int_{-\infty}^{x} f(x')dx', \tag{B.2}$$

where the parent distribution $\rho(x)$ is normalized to unity:

$$\int_{-\infty}^{\infty} \rho(x')dx' = 1. \tag{B.3}$$

If $f(x)$ and $I(x)$ are obtained from the testbeam results, one can calculates $P(X)$, the fractional energy deposited in a channel a distance X from the shower center, and $dP(X)/dX$, the derivative of the fractional pulse height with respect to changes in

shower position:

$$P(X) = I(X) - I(X - \delta X) \tag{B.4}$$

$$dP(X)/dX = f(X) - f(X - \delta X) \tag{B.5}$$

$P(X)$ and $dP(X)/dX$ are used for the fitting the CES cluster of the real data.

B.2 Strip/Wire Profile Differences

The parent wire profile, $\rho(x)$, is independent of the X position of the shower center (X_0) and is symmetric about X_0, while the parent strip profile depends on the Z position of the shower center(Z_0) and not symmetric about Z_0. This asymmetry is caused by two reasons; one is simply the geometry of the CES and incident electrons, which is corrected by the following transformation:

$$Z' = Z \sin\theta, \tag{B.6}$$

where θ shows the polar angle of the incident electron with respect to the detector z axis.

Another reason is the total amount of the materials in front of the CES for the incident electrons is depend on the angle of the incident electrons, which is corrected by multiplying $cos\,\theta$ to the asymmetric parent function, $f_{s,anti}(z')$.

In general, the strip profile is decomposed into a symmetric profile $f_{s,sym}$ and an antisymmetric profile $f_{s,anti}$, which are defined by:

$$f_{s,sym}(z) = \frac{1}{2}\left\{f_s(z) + f_s(-z)\right\}, \tag{B.7}$$

$$f_{s,anti}(z) = \frac{1}{2}\left\{f_s(z) - f_s(-z)\right\}. \tag{B.8}$$

So the complete strip profile is then written by:

$$f_s(z') = f_{s,sym}(z') + f_{s,anti}(z')cos\,\theta, \tag{B.9}$$

Figure B.1 shows the standard electron profiles and the standard electron integral profile, both of which are from the electron testbeam results. Both plots are normalized to unity.

B.3 Parameterization of the CES Standard Profile

B.3.1 Parameterization of the Symmetric Profile

The transverse profile in a radial coordinate is parameterized as a double exponential form:

$$I(r) = \frac{0.5}{1+g}\left[\exp\left(-\frac{|r|}{b_1}\right) + g\exp\left(-\frac{|r|}{b_2}\right)\right] \tag{B.10}$$

Note that $I(r)$ is symmetric about $r = 0$ and $I(0) = 0.5$. I is then transformed from a radial coordinate to the x and z positions measured by the strip chambers:

$$I(X) = \frac{0.5}{1+g_x}\left[\exp\left(-\frac{|X|}{b_{1x}}\left(1+\frac{q_{1x}|X|}{b_{1x}}\right)\right) + g_x\exp\left(-\frac{|X|}{b_{2x}}\left(1+\frac{q_{2x}|X|}{b_{2x}}\right)\right)\right], \tag{B.11}$$

$$I(Z) = \frac{0.5}{1+g_z}\left[\exp\left(-\frac{|Z|}{b_{1z}}\left(1+\frac{q_{1z}|Z|}{b_{1z}}\right)\right) + g_z\exp\left(-\frac{|Z|}{b_{2z}}\left(1+\frac{q_{2z}|Z|}{b_{2z}}\right)\right)\right], \tag{B.12}$$

where X and Z are given in cm.

Table B.1 shows the parameters of the symmetric profile.

Parameter	g	b_1	b_2	q_1	q_2
X(Wire) Value	0.311	0.472	2.065	-0.031	-0.044
Z(Strip) Value	0.269	0.583	2.182	-0.031	-0.044

Table B.1: parameters

B.3.2 Parameterization of the Antisymmetric Profile

The integral, from $-\infty$ to Z, of the antisymmetric distribution can be parameterized as:

$$\delta I(Z) \;=\; (a + b\,|Z|)\,\exp\left(-\frac{|Z|}{b_3}\right)\,, \tag{B.13}$$

where Z is the shower coordinate relative to shower center. ***. a, b and b_3 are therefore $a = -0.026, b = -0.022, and b_3 = 1.60$. Using these values, Eq. B.13 multiplied by a factor

$$f \;=\; 1 \;+\; 0.35\exp\left(-|Z|/5.\right) \tag{B.14}$$

fits the 1985 testbeam data within 5 cm of the shower center.

B.3.3 Energy Scaling of the Variance

The variance σ_i^2, the squared RMS fluctuation of CES channel i in a profile normalized to unity depends on the number of secondary particles passing through the CES. Basically the number of secondaries is proportional to the primary electron's energy $(N \sim E)$, and assuming Poisson fluctuations in the fractional number of secondaries in each channel $(\sigma_i^2 = 1/N_i)$ gives a variance:

$$\sigma_i^2 \;\sim\; 1/E. \tag{B.15}$$

From 1985 testbeam, we estimated the energy dependence of the variance of the CES.

$$\sigma_i^2 \;=\; \sigma_{10,i}^2\,\left(\frac{10}{E}\right)^{0.747} \tag{B.16}$$

where

$$\sigma^2_{10,i} \;=\; (0.026)^2 \;+\; y(x_i)\,(0.096)^2 \tag{B.17}$$

is the variance of channel i in the normalized profile determined from 1985 10 GeV testbeam electrons. Equation B.16 and the power 0.747 in that equation were determined from the measured CES response vs. energy in 1985 testbeam data.

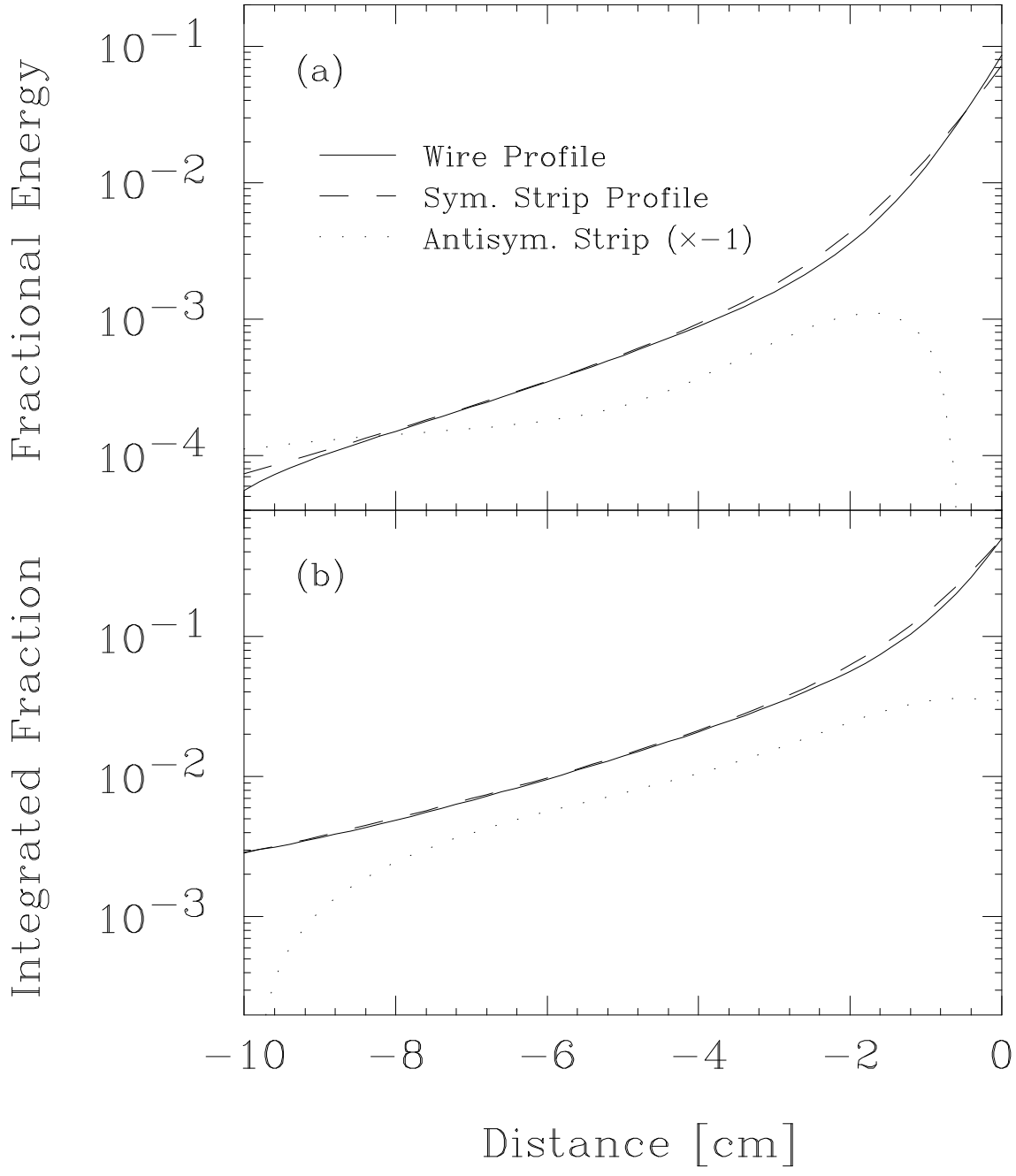

Figure B.1: cesprofile

Bibliography

[1] H. Fritzsch, M. Gell-Mann and H. Leutwyler, Phys. Lett. B 47 (1973) 365.

[2] D. J. Gross, and F. Wilczek, Phys. Rev. Lett. 30 (1973) 1343,

[3] H. D. Politzer, Phys. Rev. Lett. 30 (1973) 1346,

[4] F. Abe *et al.*, Phys. Rev. D 49 (1994) 1.

[5] F. Abe *et al.*, Phys. Rev. Lett. 77 (1996) 448.

[6] F. Abe *et al.*, Phys. Rev. Lett. 77 (1996) 438.

[7] J. F. Owens, Rev. Mod. Phys. 59 (1987) 465.

[8] R. P. Feynman, Phys. Rev. Lett. 23 (1969) 1415.

[9] J. D. Bjorken, E. A. Paschos, Phys. Rev. 185 (1969) 1975.

[10] D. W. Duke and J. F. Owens, Phys. Rev. D 30 (1984) 49.

[11] G. Altarelli and G. Parisi, Nucl. Phys. B 126 (1977) 298.

[12] J. Botts *et al.* (CTEQ collaboration), Phys. Lett. B 304 (1993) 145.

[13] B. Bailey *et al.*, Phys. Rev. D 46 (1992) 2018.

[14] J. F. Gunion, G. L. Kane and J. Wudka, Nucl. Phys. B 299 (1988) 231.

[15] F. Abe *et al.* (CDF collaboration), Phys. Rev. Lett. 73 (1994) 2662.

[16] J. Huston *et al.*, "A Global QCD Study of Direct Photon Production", MSU=HEP-41027, Michigan State University, January 1995.

[17] J. Huston, private communication.

[18] T. Ferbel, W. R. Molzon, Rev. Mod. Phys., 56, (1984) 181.

[19] J. Alitti *et al.* (UA2 collaboration), Phys. Lett. B 288 (1992) 386.

[20] C. Albajar *et al.* (UA1 collaboration), Phys. Lett. B 209 (1988) 385.

[21] F. Abe *et al.* (CDF collaboration), Phys. Rev. Lett. 70 (1993) 2232.

[22] D. Toback, "The Diphoton Missing E_T Distribution at CDF", Proceedings of the 1996 DPF Meeting.

[23] F. Abe *et al.* (CDF collaboration), Nucl. Instr. and Meth. A271 (1988) 387.

[24] H. Minemura *et al.*, Nucl. Instr. and Meth. A238 (1985) 18.

[25] F. Snider *et al.*, Nucl. Instr. and Meth. A268 (1988) 75.

[26] F. Bedeschi *et al.*, Nucl. Instr. and Meth. A268 (1988) 50.

[27] L. Balka *et al.*, Nucl. Instr. and Meth. A267 (1988) 272.

[28] R. Blair *et al.*, "Proposal for a Preradiator Chamber for the CDF Central Detector", CDF internal note 760.

[29] K. Yasuoka *et al.*, Nucl. Instr. and Meth. A267 (1988) 315.

[30] R. G. Wagner *et al.*, Nucl. Instr. and Meth. A267 (1988) 330.

[31] S. Bertolucci *et al.*, Nucl. Instr. and Meth. A267 (1988) 301.

[32] G. W. Foster *et al.*, Nucl. Instr. and Meth. A269 (1988) 93.

[33] G. Ascoli *et al.*, Nucl. Instr. and Meth. A269 (1988) 63.

[34] B. Denby *et al.*, Nucl. Instr. and Meth. A356 (1995) 485.

[35] L. Nodulman, K. Byrum, "CEM Tower Calibration and Map Trim", CDF internal note 2487.

[36] L. Nodulman, "Preliminary CEM Calibration for 1B to the Feb. Shutdown", CDF internal note 3048.

[37] A. Maghakian *et al.*, "Inclusive Photon Cross Section 1992", CDF internal note 1963.

[38] R. M. Harris, "Definition of CES χ^2", CDF internal note 1329.

[39] "Review of Particle Physics", Phys. Rev. D 54 (1996).

[40] R. M. Harris, R. Blair and S. Kuhlmann, "Calibration of CPR Conversion Probability from Fully Reconstructed η and π^0 Mesons", CDF internal note 2318.

[41] S. Kuhlmann and A. Maghakian, "Calibration of CPR Conversion Probability from $\rho^{\pm} \rightarrow \pi^{\pm}\pi^0$ Decay", CDF internal note 2478.

[42] F. Abe *et al.* (CDF collaboration), Phys. Rev. D 40 (1989) 3791.

[43] W. H. Press, Section 13.5 in *Numerical Recipes: The Art of Scientific Computing.*

[44] A. G. Frodesen, O. Skjeggestad, H. Tøfte, *Probability and Statistics in Particle Physics*, Universitetsforlaget.